TU Delft

Delft University of Technology

Document Version
Final published version

Citation (APA)
Hysa, I. (2026). *Large-scale volumetric velocimetry for aeronautics: Advancements in 3d ptv*. [Dissertation (TU Delft), Delft University of Technology]. https://doi.org/10.4233/uuid:87b61b28-28d8-4fc5-99b4-3ebb86d079c2

Important note
To cite this publication, please use the final published version (if applicable).
Please check the document version above.

Copyright
In case the licence states “Dutch Copyright Act (Article 25fa)”, this publication was made available Green Open Access via the TU Delft Institutional Repository pursuant to Dutch Copyright Act (Article 25fa, the Taverne amendment). This provision does not affect copyright ownership.
Unless copyright is transferred by contract or statute, it remains with the copyright holder.

Sharing and reuse
Other than for strictly personal use, it is not permitted to download, forward or distribute the text or part of it, without the consent of the author(s) and/or copyright holder(s), unless the work is under an open content license such as Creative Commons.

Takedown policy
Please contact us and provide details if you believe this document breaches copyrights.
We will remove access to the work immediately and investigate your claim.

This work is downloaded from Delft University of Technology.

Large-Scale Volumetric Velocimetry for Aeronautics

Advancements in 3D PTV

Ilda Hysa

LARGE-SCALE VOLUMETRIC VELOCIMETRY FOR AERONAUTICS

ADVANCEMENTS IN 3D PTV

Dissertation

for the purpose of obtaining the degree of doctor
at Delft University of Technology
by the authority of the Rector Magnificus, prof. dr. ir. H. Bijl,
chair of the Board for Doctorates
to be defended publicly on
9 March 2026 at 17:30

by

Ilda HYSA

This dissertation has been approved by the promotors.

Composition of the doctoral committee:

Prof. dr. ir. K. van Breugel,	chairperson
Prof. dr. F. Scarano,	Delft University of Technology, *promotor*
Dr. A. Sciacchitano,	Delft University of Technology, *promotor*
Independent members:	
Prof. dr. ir. L.L.M. Veldhuis	Delft University of Technology
Prof. dr. S. Ghaemi	University of Alberta, Canada
Prof. dr. rer. nat. A. Schröder	Brandenburg University of Technology, Germany
Dr. ing. T. Rockstroh	LaVision GmbH, Germany
Prof. M. Kotsonis	Delft University of Technology, reserve member
Other members	
Dr.ir. M. Tuinstra	Royal Netherlands Aerospace Center

Keywords: Quantitative flow visualization, Particle Image Velocimetry, Large-scale wind tunnel experiments, Low-speed aerodynamics

Cover by: Ilda & Enxhi Hysa

Copyright © 2026 by I. Hysa

ISBN 978-90-836415-9-1

An electronic copy of this dissertation is available at
https://repository.tudelft.nl/.

CONTENTS

Summary ix

Samenvatting xi

1. Introduction 1
1.1. Background . . . 1
1.2. Development of aerodynamic research methods . . . 2
1.2.1. Experimental Aerodynamics . . . 3
1.3. Particle Image Velocimetry . . . 8
1.3.1. PIV components . . . 9
1.4. Particle Tracking Velocimetry . . . 14
1.4.1. Volumetric Velocimetry . . . 15

2. Large-Scale Volumetric Velocimetry 21
2.1. Background . . . 21
2.1.1. State-of-the-art . . . 22
2.2. Open Questions in Volumetric PTV . . . 29
2.2.1. Optical Access around Complex Geometries . . . 29
2.2.2. PIV System Performance . . . 30
2.3. PIV Configurations . . . 32
2.4. Research Goals and Scope of work . . . 35

I. PTV TECHNOLOGY DEVELOPMENT 39

3. Multi-Directional Redundant Volumetric Velocimetry Systems 41
3.1. Introduction . . . 42
3.2. Three-dimensional imaging and volumetric illumination . . . 44
3.2.1. Constrained Illumination . . . 45
3.2.2. Imaging in the presence of obstructions . . . 47
3.3. Experiments around a ship model . . . 52
3.3.1. Experimental Apparatus . . . 52
3.4. Results . . . 57
3.4.1. Time-Averaged Flow Topology . . . 57

3.4.2. Unsteady behaviour on the flight-deck 60
3.5. Conclusion 64

4. Asymmetric time-sequences for multiple-exposure 3D PTV 67
4.1. Introduction 68
4.2. Trace detection 70
4.2.1. Numerical example 72
4.3. Numerical algorithm 73
4.4. Experimental database 75
4.5. Results 77
4.6. Algorithm accelerators 80
4.6.1. Linear-Fit pre-selector 81
4.6.2. Direction disambiguation 81
4.6.3. Computational Effort 82
4.7. Potential and bottlenecks of ME PTV 83
4.8. Conclusions 83

II. APPLICATIONS 85

5. 3D Quantitative Flow Visualization around a Thrust-Reverser 87
5.1. Introduction 88
5.2. Experimental apparatus and measurement conditions 90
5.2.1. Wind tunnel and aircraft model 90
5.2.2. Engines and TR 91
5.2.3. 3D PTV apparatus and procedures 94
5.3. Experimental Results and Analysis 100
5.3.1. Global flow topology 100
5.3.2. Comparison with temperature based re-ingestion detection 105
5.3.3. Parametric analysis with NPR and momentum ratio 106
5.4. Conclusion 108

6. 3D PTV around a Ship at Varying Wind Directions 111
6.1. Introduction 112
6.2. Experimental apparatus and measurement conditions 113
6.2.1. Ship model 113
6.2.2. 3D PTV apparatus and procedures 114
6.3. Experimental Results and Analysis 119
6.3.1. Comparison with the SFS 119
6.3.2. Global flow-field over the ship at varying wind directions . . 122
6.3.3. Flow dynamics 124

6.4. Conclusion 127

7. Conclusions and Perspectives **129**
7.1. Measurement technology development 129
7.1.1. Multi-directional Volumetric Velocimetry Systems 129
7.1.2. Multiple Exposure for Volumetric Velocimetry 131
7.2. Impact of large-scale volumetric velocimetry in aerodynamic development 132
7.3. Further potential impact 133

Acknowledgements **147**

Curriculum Vitæ **149**

List of Publications **151**

SUMMARY

Volumetric Particle Image Velocimetry (PIV) is a state of the art technique for quantitative flow diagnostics. Its ability to measure the velocity field around the typically complex objects, as needed in the field of aeronautics, makes it a valuable tool for designers and engineers. Wind tunnel experiments making use of PIV as a diagnostic tool are used to gain physical insight into the flow field organization, generate data for validation of computational methods, and perform optimization in various domains, most notably in the field of aerospace and wind engineering.

Despite continuous advancements in the measurement technique, performing a PIV experiment in industrial wind tunnel environments remains challenging, making its use rather limited to niche applications within aeronautics or the automotive industry. In this thesis the recent advancements in helium-filled soap bubbles (HFSB) technology and 3D particle tracking algorithms are synthesized, to demonstrate the impact of PIV in industrial environments and extend its utility to a wider range of aeronautical applications.

Two limitations currently preventing the broad adoption of PIV are addressed: i) the limited spatial coverage of full-field volumetric velocimetry due to shadows and blocked optical access; ii) the limited measurement accuracy and the accessible velocity ranges by conventional two-pulse PIV systems.

Both these problems are introduced and treated in Part I of this thesis.

Multi-directional illumination and imaging systems with redundancy are introduced for the study of volumetric flows around complex geometries. A volumetric loss parameter is defined, that can be used as a guideline in the phase of experimental setup design of these systems. Additionally the logics of the combinations of the multiple cameras that work in a single system are examined and the results of the different combinations are presented.

The technical limitations in hardware technology of the cameras' frame rates have inspired the revisiting of original PIV methods of multi-exposure imaging. This is investigated as a way to increase the dynamic velocity ranges of more common and practical two-pulse systems used in industrial testing. Methodology and initial results are presented for the workings of a novel concept.

Part II introduces specific application experiments in two fields. The first is part of integrated propulsion, the study of the flow around a thrust-reverser at-

tached to a complete aircraft; and the second, the flow around the top side of the superstructure of a ship with helicopter and drone landing capabilities in the deck, investigated across a spectrum of incoming wind directions.

The study around the thrust reverser has demonstrated the feasibility and added value of PIV even in challenging complex industrial wind tunnel experiments, by providing insight into the mechanisms of jet reversal and re-ingestion, as well as a rich database that is in good agreement with, and complementary to, more traditional wind tunnel re-ingestion measurement methods.

The study of the redundant multi-illumination and camera systems has proven to increase the spatial coverage of measurements with these setups, providing more complete data for numerical low-fidelity turbulence models validation, as well as practically proving to increase the robustness of PIV systems against reflections. This has been demonstrated in the final chapter of the thesis.

SAMENVATTING

Volumetrische Particle Image Velocimetry (PIV) is een geavanceerde techniek voor kwantitatieve stroomdiagnostiek. Het vermogen om het snelheidsveld te meten rond de typisch complexe testgeometrieën die op het gebied van luchtvaart worden aangetroffen, maakt het een waardevol hulpmiddel voor ontwerpers en ingenieurs om optimalisatie en geïnformeerde iteraties uit te voeren in verschillende domeinen, met name in het gebied van lucht- en ruimtevaart en windtechniek. Ondanks de voortdurende vooruitgang in meettechniek blijft het uitvoeren van een PIV experiment in industriële windtunnelomgevingen een uitdaging, waardoor het gebruik ervan vrij beperkt is tot nichetoepassingen binnen de luchtvaart of de auto industrie. In dit proefschrift worden de recente ontwikkelingen in de heliumgevulde zeepbellen (HFSB) technologie en 3D deeltjesopsporingsalgoritmen gesynthetiseerd om de impact van PIV in industriële omgevingen aan te tonen en het nut ervan uit te breiden tot een breder scala aan luchtvaarttoepassingen. Twee beperkingen die dit momenteel verhinderen, worden aangepakt: de beperkte ruimtelijke omvattendheid van volwaardige volumetrische snelheidsmeting vanwege schaduwen en geblokkeerde optische toegang; en de beperkte nauwkeurigheid en snelheidsbereiken die kunnen worden gemeten met twee-puls PIV systemen. Beide problemen worden geïntroduceerd en behandeld in deel I van dit proefschrift. Voor de studie van de volumetrische stromen rond complexe geometrieën worden multi-directionele verlichtings- en beeldvormingssystemen met redundantie ingevoerd. Er is een volumetrische verliesparameter gedefinieerd die als leidraad kan worden gebruikt in de fase van het ontwerp van de experimentele installatie van deze systemen. Bovendien wordt de logica van de combinaties van de meerdere camera's die in een systeem werken onderzocht en worden de resultaten van de verschillende combinaties gepresenteerd. De technische beperkingen in de hardware technologie van de beeldfrequentie van de camera's en de pulserende verlichtingsfrequentie en energie hebben de herziening van de oorspronkelijke PIV methoden voor beeldvorming met meerdere belichtingen geïnspireerd. Dit wordt onderzocht als een manier om de nauwkeurigheid en de snelheid van meer gebruikelijke en praktische systemen met lage snelheid die in industriële tests worden gebruikt, te vergroten. Methodologie en eerste resultaten worden gepresenteerd van de werking van een nieuw concept. Deel II introduceert specifieke toepassingsex-

perimenten op twee gebieden. De eerste in een onderdeel van de geïntegreerde voortstuwing, de studie van de stroom rond een straalomkering (thrust-reverser) die aan een compleet vliegtuig is bevestigd; en de tweede, de stroom rond de bovenkant van de bovenbouw van een schip met landingsmogelijkheden voor helikopters en drones op het dek, onderzocht over een spectrum van modellen van gierhoek. De studie rond de straalomkering heeft de haalbaarheid en de toegevoegde waarde van PIV aangetoond, zelfs in uitdagende, complexe en grootschalige windtunnelexperimenten, door inzicht te geven in de mechanismen van jet reversie en re-ingestie, evenals een rijke database die goed overeenstemt met en complementair is aan meer traditionele windtunnelmetingen. De studie van de redundante meervoudige verlichtings- en camerasystemen heeft aangetoond dat zij de ruimtelijke omvang van de meting met deze systemen verbeteren, waardoor meer volledige gegevens worden verkregen voor de validatie van numerieke turbulentiemodellen met lage betrouwbaarheid, en dat zij in de praktijk de robuustheid van PIV systemen tegen reflecties aantonen. Dit is aangetoond in het laatste hoofdstuk van het proefschrift.

1

INTRODUCTION

1.1. BACKGROUND

Over the course of time people have used aerodynamic principles, often intuitively and long before the scientific principles behind them were understood. Such uses can be seen in the design of arrows and sails, tools essential for survival and exploration, that were probably slowly developed through the understanding that comes with trial and error.

A shift in how we approach the natural world occurred with the scientific revolution (16th to 17th century), when empirical observation and systematic analysis became central to scientific work. This way of thinking, where data is carefully collected and examined to explain and predict phenomena, continues to be central to formal research today. As scientific inquiry has become more complex, the need for expertise in increasingly narrow fields has grown.

Nowadays, the narrowness of individual expertise is attempted to be compensated with increased collaboration across multiple disciplines. Take for example the case of optical measurement techniques in aerodynamics. To clarify that one is an expert in such techniques they need to funnel down from aerospace to aeronautical engineering, to aerodynamics, to experimental aerodynamics. On the other hand, advances within optical measurement techniques combine innovations in the fields of optics and photonics, camera technology, computer hardware and processing algorithms inspired by a number of distant fields.

Within the field of aeronautics, over the past century aerodynamic testing has played a critical role in transforming conceptual aircraft designs into viable machines capable of flight, as well as in supporting fundamental research. The contrast of the images from Figure 1.1, attempts to capture the progress done in aerodynamic testing in the past 150 years. In the left is a sketch of one

1

the simplest devices for moving models around that was available in the 19th century, the whirling arm, used among others by Lilienthal (1889). Spun by a falling weight acting on a pulley and spindle arrangement, the whirling arm provided most of the systematic aerodynamic data gathered up until the end of the 1800's, which typically consisted of flat plate measurements. Jumping to the present day, on the right of Figure 1.1 is a photograph from the testing of an open rotors, hybrid-electric systems aircraft at one of the largest wind tunnels in Europe, the Large Low-Speed Facility of the German-Dutch Wind Tunnels. The testing of such novel architectures (in this case developed as part of the European research program Clean Sky) represents a step in the direction of the achievement of the ambitious modern goals of sustainable aviation.

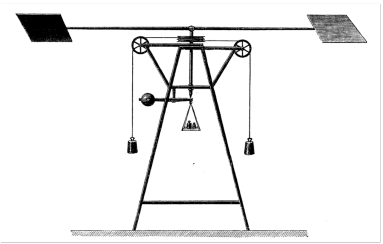

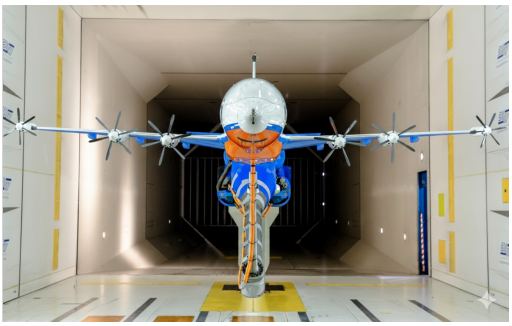

Figure 1.1.: Progress in Wind Tunnel Technology from the whirling arm Lilienthal (1889) to modern wind tunnels (2023, Public domain).

As we look to the future, the need for sophisticated aerodynamic tools and methods will only grow. Whether improving the efficiency of current designs, or characterizing disruptive new concepts, whether in aviation or wind engineering, the ability to understand and shape airflow with precision will continue to be highly relevant.

1.2. DEVELOPMENT OF AERODYNAMIC RESEARCH METHODS

One of the foundational tools in aerodynamic development is analytical modelling. It is beneficial due to its simplicity and the ease with which it can provide insights, however its utility is very limited when dealing with complex flows, where assumptions made in the models may no longer hold true.

Nevertheless, theory informs the governing equations of the computational methods, and fundamental results like the Bernoulli theorem, isentropic flow theory and shock wave theory are of use as guiding principles even to examine

complex flow data.

The limitations of analytical modelling to account for intricate flow phenomena around complex geometries, turn the attention to numerical modelling.

Over the past several decades, computational fluid dynamics (CFD) has been increasingly used in the aerospace industry for the design of new and derivative aircraft. Regarding the issue of capturing complex flow phenomena with CFD, today even with modern high-performance computing resources, converged high-fidelity simulations results, for instance around passenger aircraft, cannot be provided and will most probably not be reachable within the next couple of decades (Schröder and Schanz (2023)).

The most consistently used models in industry, Reynolds-averaged Navier-Stokes (RANS), work well for attached flows, but are inadequate for other situations dominated by large boundary layer separation (Mani and Dorgan (2023)). Improving the accuracy and expanding the scope of the applicability of the current RANS methods would have a significant impact on industry. Validating the low-fidelity turbulence models requires wind tunnel testing data.

To this day, experimental methods still remain a crucial part of aerodynamic development. The data gathered from experimental testing is highly valuable, providing real-world validation for both analytical and CFD models. In order to achieve this, spatially (and for unsteadiness investigations temporally) well-resolved data at high Reynolds numbers, preferably in large volumes around various complex geometries are needed. Having this kind of experimental data available offers unique opportunities to combine the strengths of experimental and numerical approaches.

Additionally, testing experience, especially of the less well-established measurement techniques, is invaluable in terms of identifying areas that need improvement and for informing future technological advancements. Pushing the limits of the experimental techniques clarifies the areas with specific needs for innovation.

1.2.1. EXPERIMENTAL AERODYNAMICS

Experimental aerodynamics is performed at different lengths and velocity ranges. These scales are important because aerodynamic phenomena can vary significantly depending on the size of the object and the speed of the airflow, influencing the relevance and accuracy of the results.

For the purposes of the disambiguation of the terminology that is used in the rest of this thesis the term 'large-scale', is clarified in this section, as depending on the field of study, large-scale can mean different things. For

instance, the range of scales where optical measurement techniques like PIV are applied is quite broad, from micron resolution of the fluid velocity near walls by Stone et al. (2002), to the planetary cloud-tracking PIV correlation based methods to extract velocity fields from the atmosphere of Jupiter, Saturn and Earth (Liu and Salazar (2022)). Most commonly, PIV is applied to a planar region of space ranging from 10x10 cm^2, to the area of an A3 sheet (30x40 cm^2).

Figure 1.2 presents three examples from very diverse experimental and measurement conditions. The photograph in the top left illustrates the visualization of delta-wing vortices by filaments of dye in a water tunnel. Here the model is very simplified and downscaled, resulting in a low Reynolds number. The image on the right illustrates results achieved with state-of-the-art quantitative flow visualization in a wind tunnel (3D PTV, see Chapters 2 and 6). Finally, the photograph on the bottom left shows a full-scale, accidental flow visualization from a ship leaking oil at sea.

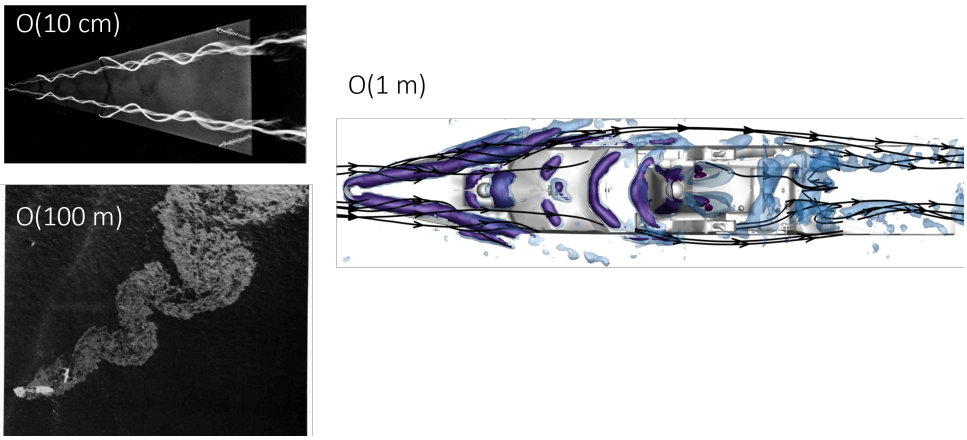

Figure 1.2.: Lab, Wind Tunnel and Full Scales. Top left: ONERA photograph of the vortices in an inclined triangular wing, test object approx. 10 cm (Van Dyke (1982)); Right: Quantitative visualization of two different values of the Q-criterion and streamlines on a ship model of 1.5 m length (Chapter 6); Bottom left: NASA photograph of the accidental flow visualization from a ship leaking crude oil at sea, model in the order of approx. 100 m (Van Dyke (1982))

Since the focus of this thesis is in PIV measurements in wind tunnels, the term large-scale in the rest of this thesis refers to volumetric measurements performed in the order of 1 m^3.

To ensure flow similarity between model-scaled and full-scaled objects, it is required that the experiments meet the criteria of:

- Geometric similarity - the sub-scaled model has the same geometrical shape as the actual application, and a single scaling parameter can relate the two geometries.
- Kinematic similarity - geometric similarity of the streamline patterns of the flowfield around the geometry, and proportionality of the distributions of velocity, pressure, temperature, etc. when plotted against common non-dimensional coordinates (Anderson (2011)).
- Dynamic similarity - the force coefficients are the same, a consequence of meeting the first two criteria.

In this context, the two parameters that are by far the dominant similarity parameters for most aerodynamic applications in wind tunnel testing are the Reynolds number (Equation 1.1) and the Mach number (Equation 1.2).

$$Re = \frac{\rho V L}{\mu} \tag{1.1}$$

where ρ is the density of the freestream flow, V is the freestream flow velocity, L is the characteristic length of the model, and μ is the freestream dynamic viscosity of the fluid. The Reynolds number is physically a measure of the ratio of inertial to viscous forces in the flow.

$$M = \frac{V}{a} \tag{1.2}$$

where $a = \sqrt{\gamma RT}$ is the freestream speed of sound. The Mach number is the ratio of the freestream flow velocity to the speed of sound.

In a limited sense, but applicable to many problems, such as those considered in this thesis, it can be said that the flow over geometrically similar bodies at the same Mach and Reynolds numbers are dynamically similar, and hence the lift, drag and moment coefficients will be identical for the bodies. The focus of this thesis is on the subsonic, incompressible flow regime, up to V = 80 m/s (M = 0.23). Therefore, typically only the matching of the Reynolds number is a key point.

$$Re_{model} = Re_{full-scale} \tag{1.3}$$

This is taken to ensure the validity of the wind tunnel testing. To a large-extent, the main influencing parameters are boundary layer properties

just prior to separation, so in cases where the separation point is fixed (for example due to sharp edges on the test geometry) the characteristics of the flow are even independent on Reynolds number. This independence is elaborated further in this thesis.

WIND TUNNEL MEASUREMENTS

In industrial wind tunnels the most common measurement techniques are direct force measurements by balance and surface pressure measurements through tiny orifices. Figure 1.3 depicts typical examples of the instrumentation of the sensors. Although the two techniques provide reliable data and are considered the state-of-the-art for wind tunnel measurements in industrial facilities, they provide no information about the flow field around the models (e.g. flow separation, vortices, unsteadiness etc.). If the interest is in the entire flow field, as is often the case with newer, not well established applications, then techniques that provide full field data are required as the analysis of flow features in aerodynamics often involves the study of vortices released from or interacting with the test model.

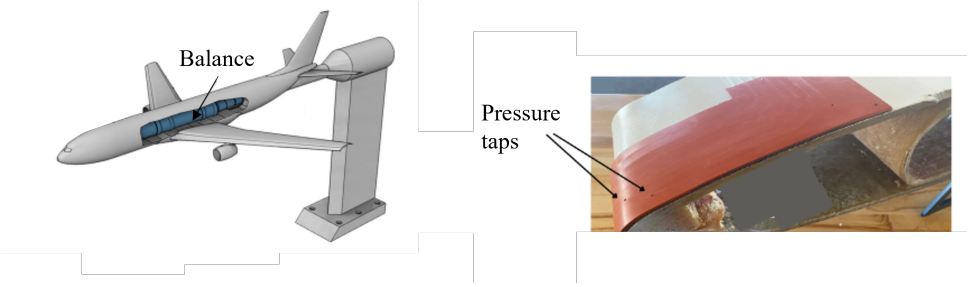

Figure 1.3.: Left: Schematic of wind tunnel force balance measurements; Right: Photograph of typical pressure taps on the test body. Figures adapted from Burns and Parker (2020),Vandervoort et al. (2023).

The simplest step toward obtaining such information is qualitative flow visualization, where certain areas of the flow are made visible by marking a streamtube in the flow with smoke or dye. Depending on where the tracers are released they will be entrained in boundary layers, wakes behind models etc. The spatial and temporal evolution of these structures can be studied in this way, however it does not allow for accurate predictions for design and operation. Additionally the detailed analysis at specific planes of interest is hindered by the fact that only the smoke bulk can be inferred. Finally, comparison between experiments or data obtained with numerical

simulations is not possible in this way, and requires quantitative data to lead to conclusive investigations.

MEASURING THE AIR FLOW VELOCITY

Determining the velocity of air is not straightforward as it is transparent, therefore the air motion cannot be traced unless another element, such as flow seeding, is introduced in it. That is why many measurement techniques that have been developed determine the flow velocity indirectly by measuring other quantities such as pressure – with pressure probes, rotational speed – with anemometers, or heat transfer – hot wires. In these cases the velocity of the flow is finally derived through well-understood and well-established relations of physics (Raffel et al. (2018)).

The advantage of the indirect measurement techniques is that they are easy to use and relatively cheap. The disadvantage is that they disturb the flow or fluid properties leading to measurement errors, and that they deliver results only at a single location. In order to obtain information about the velocity field, the probe needs to be traversed through the flow field, which is a process that requires time, limiting the methods to the traversing resolution and time-averaged information.

In order to overcome such difficulties optical measurement techniques have been developed, which allow placing the measurement sensors outside the flow to capture images of the whole flow field of interest. In comparison to the point-wise measurements, these techniques are quite complex and the costs needed for the equipment are high. Those optical measurement techniques which have found wider use, need tracer particles that follow the flow motion faithfully without disturbing the fluid properties. By measuring their position in time, the velocity of the flow can be measured indirectly.

The most important optical measurement techniques to obtain the flow velocity are Laser Doppler Velocimetry (LDV) (Wang (1988)) and Particle Image Velocimetry (PIV) (Raffel et al., 2018).

LDV relates the speed of the moving tracers to the frequency shift of the light scattered from the tracer particles, and is a point-wise measurement. PIV provides the displacement of tracer particles between two instants of time focusing on ensembles of tracer particles, or focusing on single tracer particles in the version Particle Tracking Velocimetry, and it a planar or volumetric technique.

In the past three decades PIV has become a standard tool in laboratory scale experimental fluid mechanics, primarily due to this ability to measure instantaneous velocity fields simultaneously at many points. This is the technique that is the focus of this thesis, specifically its development and

application in large-scale. The next section gives an overview of its working principles.

1.3. PARTICLE IMAGE VELOCIMETRY

Particle Image Velocimetry as a measurement technique in fluid mechanics was first mentioned in Adrian, 1984, to refer to an optical, quantitative and non-intrusive field measurement technique. Since then the frequency and versatility of its use can be gauged by looking into the literature published on this subject. Books that cover the more fundamental aspects of the technique along with the advancements up to the time of their publishing include Raffel et al. (1998), Adrian and Westerweel (2011), Raffel et al. (2018), as well as covering applications by Schröder and Willert (2008).

Additionally multiple reviews have been published such as the early work by Adrian (1991), and then again at the twenty year mark of the technique development by Adrian (2005). Topical reviews have been published on tomographic PIV by Scarano (2012), PIV in complex flows by Westerweel et al. (2013), volumetric PIV by Discetti and Coletti (2018), time-resolved PIV by Beresh (2021) and more recently 3D Lagrangian particle tracking by Schröder and Schanz (2023).

The specific type of PIV studied and further advanced in this thesis is Large-Scale Volumetric PIV, which is the subject of Chapter 2. A brief introduction of the technique is given here, but it does not attempt to be fundamental or exhaustive. For a more complete understanding of the technique the reader is referred to any of the previously listed references and their bibliographies.

Before delving into the components of the measurement technique a disambiguation of terminology is helpful. Over the years PIV has evolved as an umbrella term to also cover Particle Tracking Velocimetry (PTV) and Lagrangian Particle Tracking (LPT). This is because all these techniques are based on particle images, and the branching in terminology separates correlation based image analysis from individual particle tracking methods. In this thesis the general umbrella term is preferred due to its generality and widespread use.

The layout of a PIV setup is shown in Figure 1.4. The flow is seeded with tracer particles in order to visualize its motion. These particles are illuminated and their position in space is recorded at known times. Through the known time separation and image processing algorithms the velocity of the tracer particles is extracted, and under the assumption that they follow the fluid faithfully, this is assumed to be the velocity field of the fluid under study.

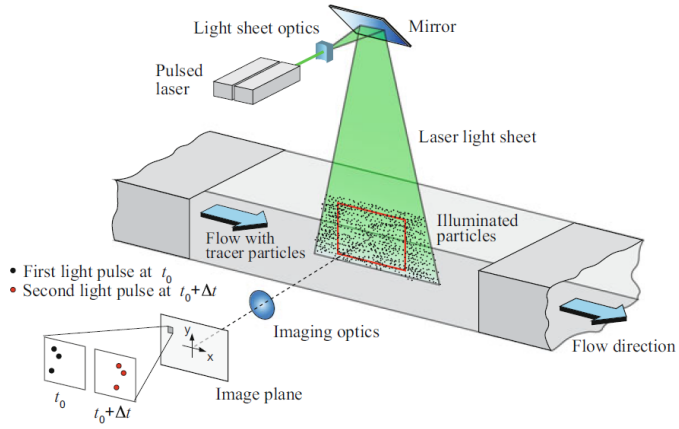

Figure 1.4.: Components of 2D, 2C PIV. Schematic reproduced from Raffel et al. (2018)

The combination of double-pulsed laser forming a light sheet, a single camera imaging light scattered from particles at 90 degrees to the light sheet, and spatial correlation analysis of the images to determine their displacement in the imaging plane, depicted in Figure 1.4 is a standard that has remained relatively constant over the past decades, due to its effectiveness and simplicity. Nevertheless there is some range in the choice of each component that is available to the experimentalist.

1.3.1. PIV COMPONENTS

TRACER PARTICLES

The appropriate selection of tracer particles is fundamental to any PIV measurement. Assessing the fluid velocity through quantification of particle displacement in images implies that the disparity between the particles and the fluid motion is negligible. In other terms, the particle velocity must adapt rapidly to any change in the fluid velocity, which is quantified by the particle response time τ_p (Raffel et al. (2018)).

$$\tau_p = \frac{d_p^2(\rho_p - \rho_f)}{18\mu} \tag{1.4}$$

where ρ_p and ρ_f represent the tracer particle and fluid density respectively. The above equation is derived from Stokes drag which assumes the particle-fluid interaction is dominated by viscous forces and therefore, it is only valid for small values of the particle's Reynolds number. The fluid kinematic

viscosity is a given property of the fluid of interest, meaning that the only parameter that can be varied are the tracer particles' diameter and density. Consequently, the response time in Eq. 1.4 is minimized by selecting small particles or by choosing neutrally buoyant tracers with particle density approaching that of the fluid. Commonly, the response time is considered acceptable if the Stokes number is below 0.1 Samimy and Lele (1991).

$$S_k = \frac{\tau_p}{\tau_f} \tag{1.5}$$

where τ_f is the relevant flow time scale.

The tracer size will affect the light scattering properties of the particles (the smaller the tracer, the less light will be scattered). The amount of light scattered increases proportional to the scattering cross-section which scales with the square particle diameter (Caridi (2018)).

ILLUMINATION

The tracer particles have to be illuminated for them to be imaged sufficiently clearly. Typically in PIV pulsed light is used to achieve this. In this regard, the most important parameters to be considered for the illumination source are schematically shown in Figure 1.5 and are namely the: pulse width δt, pulse energy E_p, the pulse sequence which includes the time separation between the pulses Δt, the frequency f, and their overall number, N. In this figure three different cases are depicted: double-pulse systems - the most common due to their simplicity, characterized by high pulse energy depending on the power source (for lasers this is typically up to 300 mJ per pulse), and frequencies up to 15 Hz; multi-pulse systems - in the most straightforward way that can be obtained by a combination of multiple double-pulse systems, also operating at the same frequency; high-repetition, high-speed systems - characterized by lower pulse energy (for lasers this is typically up to 10 mJ per pulse) and higher frequency (up to 10kHz).

The pulse energy is critical to get good signal to noise ratio, especially in large scale where the source has to be expanded in a large sheet or a volume, further elaborated in Chapter 2.

The time separation and its customization between the pulses determines the resolution and accuracy of the measurement, and should be adjusted depending on the range of velocities in the flow to be measured. Typically this is desired to be controllable in the order of microseconds, and it determines the rate of sampling along the particle trajectory Raffel et al. (2018).

Additionally depending on the sensitivity of the imagers, the wavelength of the light is relevant (most cameras are sensitive to green light 526-532 nm

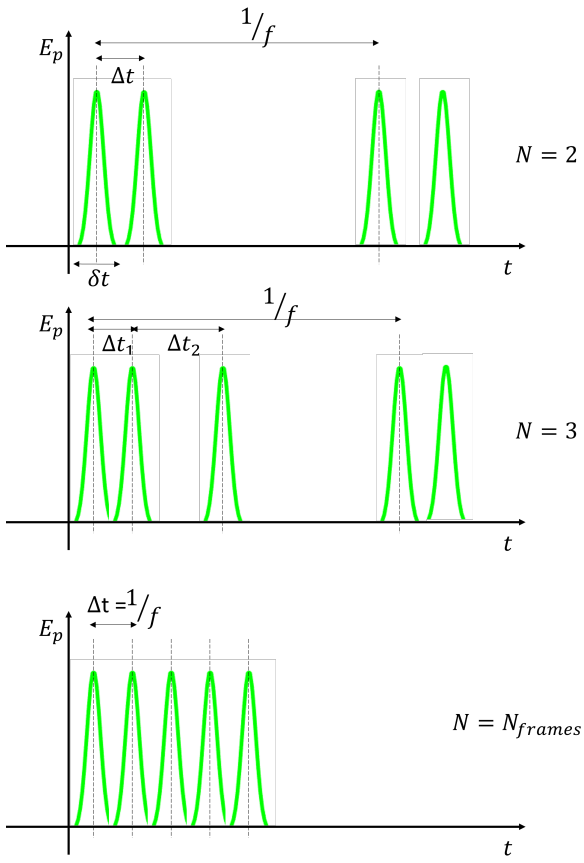

Figure 1.5.: Schematic features of the: Top - Low frequency 2-pulse illumination; Middle - Low frequency multiple, in this case 3-pulse illumination; Bottom; High frequency illumination.

wavelength). Other considerations consider the light collimation and the ease of shaping it into sheets of volumes.

Common practice is to provide the illumination of particles by high-power lasers, such as Nd:YAG (neodymium: yttrium aluminium garnet) and Nd:YLF (neodymium: yttrium lithium fluoride), to produce light of wavelengths within the visible part of the spectrum (532 nm and 526 nm, respectively). These lasers provide high energy monochromatic light, allowing illumination of large volumes or planes (laser sheets) through properly manipulating the light with optical lenses and mirrors. Most conventional PIV investigations utilize light sheet illumination, achieved through sending the laser light beam through a combination of cylindrical and/or spherical lenses to produce specific sheet

width and thickness.

More recently light-emitting diodes (LED) have found applications in PIV, primarily for volumetric imaging. They are composed of banks of dozens of hundreds of individual LEDs to create intense flood lights. They are available as white light or specific wavelength ranges such as green to match typical camera sensitivity. They can either be continuous or pulsed, but they tend to provide lower pulse energy for shorter pulses. The pulse lengths recorded in literature are in the order of 100 microseconds (Kühn et al. (2012)) which is orders of magnitude higher than low-speed lasers that provide pulse widths in the order of 10 -100 nanoseconds, although constant progress is being made in this technology.

IMAGING

The most common electronic sensors used for digital PIV cameras are charge coupled devices (CCD), complementary metal oxide semiconductor (CMOS) devices, and scientific CMOS (sCMOS) devices Raffel et al. (2018).

Having illuminated the particles, the light scattered or reflected from them towards the camera, travels through a lens and impinges onto the image sensor. The displacement recorded on the image plane must then be translated back to the object plane before the velocity is calculated. From the thin lens approximation, the lens focal length relates the distance between the image and lens planes (z_i) to the distance between the object and lens planes z_o as follows:

$$\frac{1}{f} = \frac{1}{z_i} + \frac{1}{z_o} \tag{1.6}$$

The particle position on the object plane at time t is obtained as follows:

$$\overrightarrow{x_p}(t) = -\frac{\overrightarrow{X}(t)}{M} \tag{1.7}$$

where $\overrightarrow{X} = (x_i, y_i)$ is the position of the particle image, i.e. the projection of the particle position $\overrightarrow{x}_p = (x_p, y_p, z_p)$ onto the image plane, and M is the image magnification:

$$M = \frac{z_i}{z_o} \tag{1.8}$$

This transformation can lead to perspective errors in 2D imaging since the true displacement of the particle cannot be recovered.

The planning of a PIV experiment requires the proper choice of the camera lens focal length f and the aperture diameter D_a. The latter is defined in practice by setting the objective $f_\#$:

$$f_\# = \frac{f}{D_a} \tag{1.9}$$

The choice of f and $f_\#$ defines the particle image diameter and the depth of field δ_z for a given image magnification M and light wavelength λ.

To obtain the image diameter of small particles light diffraction has to be considered. The light scattered by a small particle forms a diffraction pattern on the camera sensor given by Adrian and Yao (1985):

$$d_{diff} = 2.44 f_\# (M+1)\lambda \tag{1.10}$$

Neglecting lens aberrations and considering particles imaged in focus, the particle image diameter becomes:

$$D = \sqrt{(M d_p)^2 + d_{diff}^2} \tag{1.11}$$

For good imaging of the particles, they should encompass at least two pixels to avoid peak-locking - a biasing of the measured displacement towards integer values of the displacement in pixel units Westerweel (2000).

Furthermore, if all particles are to be in-focus, the depth of field must be greater than or equal to the illuminated volume. The depth of field gives the distance along the camera axis between the two extreme out-of-focus positions, based on d_{diff}, that still yields an acceptable particle diameter. The depth of field is given as:

$$\delta z = 4.88 \lambda f_\#^2 (M^{-1}+1)^2 \tag{1.12}$$

IMAGE PROCESSING

Image analysis techniques can be characterized in two different classes: correlation based and tracking of individual particles.

Originally PIV referred to the method of displacement evaluation by means of cross-correlation Keane and Adrian (1992). This means that the frames are divided into smaller interrogation regions, and the displacement of the particle images in each interrogation region is defined by cross-correlation. The correlation peak is located with sub-pixel accuracy by fitting a Gaussian or similar function to the tallest correlation peak, and this measurement gives an estimate of the mean displacement of the particles residing in the volume

that corresponds to the intersection of the interrogation domain with the laser light sheet Willert and Gharib (1991).

In today's practice cross-correlation is normally executed in an iterative manner, with a successive reduction and deformation of the interrogation window size following Scarano (2001).

1.4. PARTICLE TRACKING VELOCIMETRY

The spatial resolution is raised beyond that of the correlation-based analysis if individual particles are tracked, yielding one velocity vector per tracer rather than one per interrogation volume Kähler et al. (2012). However particle image density requirements for particle tracing tend to be more strict, as false particle pairings yields false velocity measurements Maas et al. (1993).

The working principle of PTV can be briefly summarized as:

- Detection of particle images from each recording. This is done by eliminating background intensity and analyzing the images in search of local maxima.
- Forming a vector of particle positions at each of the time instants with sub-pixel accuracy.
- Pairing particle images corresponding to the same physical tracer. (Here the most common criterion for a simple analysis is that the image pair with the closest distance corresponds to the correct image pair).

Predictor-corrector schemes where a priori knowledge of the velocity field is imposed to match particle images have been applied in numerous versions and they can be used to make the technique more robust. More detail on the specific tracking schemes used in this thesis are provided in the following section for the case of volumetric tracking.

MEAN FLOW ANALYSIS BY ENSEMBLE AVERAGING

Following the particle pairing and displacment determination in PTV, the unstructured particle data is converted onto a structured grid.

For densely seeded, unsteady flows the interest is often in the analysis of the instantaneous flow data.

In this thesis, the focus lies on the evaluation of the time-averaged flow fields. For the time-averaged analysis of particle track data, the velocity information belonging to an ensemble of particles is averaged in both space and time. Hence, the process is frequently referred to as a spatio-temporal

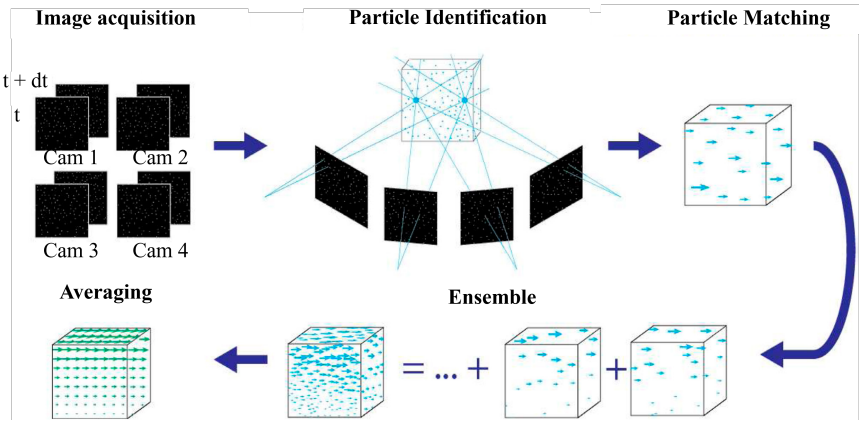

Figure 1.6.: Sketch of the ensemble PTV process. Figure adapted from Agüera et al. (2016).

ensemble averaging. The common strategy that is pursued in this thesis works on the following basis:

- The measurement domain is discretised into equally shaped and spaced sub-volumes. Each of these sub-volumes, referred to as cells or bins, represents one velocity measurement at its center.
- The particles are assigned to the cells based on their spatial position. This step leads to an ensemble of particle velocity readings for each cell.
- The velocity readings are averaged per cell, yielding the mean velocity field on the Cartesian grid defined by the cells. Averaging schemes range from an arithmetic mean to fitting of distribution functions.
- Once the mean of the velocity for a cell is computed, additionally statistical analysis in terms of velocity fluctuations can be performed, for example the standard deviation of the velocity fluctuations.

A detailed description of this type of ensemble averaging procedure, specifically for 3D PTV data is presented by Agüera et al. (2016).

1.4.1. VOLUMETRIC VELOCIMETRY

SCANNING 2D PIV

Adding a second camera to a PIV system like the one depicted in Figure 1.4 enables to make a stereoscopic setup, where all three velocity components

can be measured in a plane. Utilising such 2D systems to slice volumes in depth, scanning PIV provides 3D measurements by multiple planar samples (Gray et al. (1991), Brücker (1997)). Apart from the increased experimental complexity needed to provide the scanning however, this technique (as all scanning techniques) is limited to flows where the time scales of the flow are higher than the time needed to scan the volume, i.e low speed flows.

Another option to obtain quasi-volumetric data is multi-plane stereo PIV, where several adjacent planes are illuminated and imaged with multiple stereo-PIV systems. To achieve optical separation between the light in separate planes, different wavelengths or light polarization can be used. Whereas this solves the problem of the measurable flow speed, it introduces significant experimental complexity and cost, as multiple PIV systems have to be calibrated and operated simultaneously.

TOMOGRAPHIC PIV

The transition from scanning approaches to volumetric measurements was achieved with the development of tomographic PIV by Elsinga et al. (2006). Using three or more cameras the particle distribution in a volume is reconstructed from its two-dimensional images in a tomographic reconstruction problem, such as the motion analysis is carried out in a three-dimensional space. The cameras are placed subtending a solid angle to observe the illuminated region from several viewing directions.

The relation between the position of the particles in three-dimensional space and their projection onto the image planes is obtained with a calibration procedure similar to what is used for stereoscopic PIV or 3D PTV Tsai (1987), Soloff et al. (1997).

The tomographic reconstruction is based on the geometrical relation between 3D physical space and the image space, referred to as a calibration or mapping function. A third order polynomial and the pinhole model are the most commonly adopted choices to represent the mapping function.

Any misalignment in the geometric calibration leads to rather large errors that require a correction Scarano (2012). A procedure for misalignment detection and correction for 3D measurements is known as '3D self-calibration', which is based on particle detection in the individual recordings and their triangulation in 3D space (Wieneke (2005), Wieneke (2008)). The data is clustered in sub-volumes yielding the statistical estimate of the local disparity vector used to correct the mapping functions for all cameras.

Following the corrected mapping, the set of simultaneously recorded images is the input to the particles' 3D object reconstruction algorithm. Within tomographic PIV, this is commonly done by an iterative algebraic

reconstruction method (MART among others). Subsequently, the analysis of the particles motion within a pair of objects is performed by three-dimensional cross-correlation. This entire process is schematically depicted in Figure 1.7.

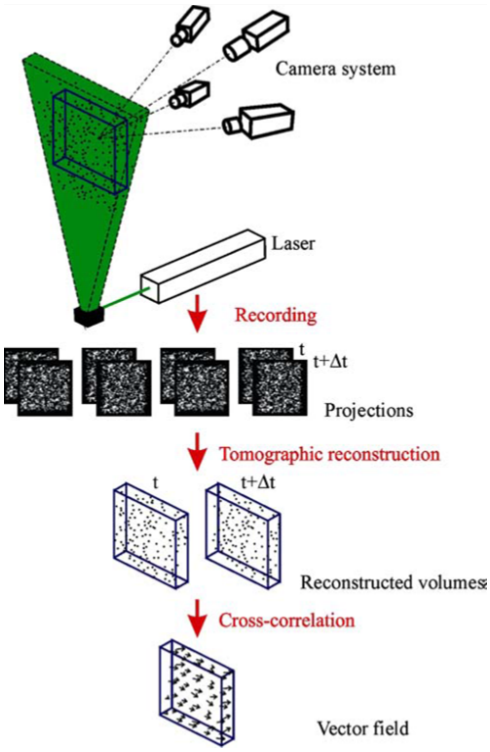

Figure 1.7.: Components and procedure of tomographic PIV. Image from Elsinga et al. (2006).

Table 1.1 summarizes the chronological progression of some of the most important developments of volumetric velocimetry, in the context of making the technique more robust and versatile. Following its introduction, the work of Scarano and Poelma (2009) showed its suitability for the study of complex flows. The feasibility of its extension to large-scale was then shown in a convection cell measurement by Kühn et al. (2012). A further important development for a wider application was the extension of tomo-PIV for measuring higher speed flows in its multi-pulse version (Lynch and Scarano (2014)).

Eventually hybrid approaches such as tomographic PTV, where after the tomographic particle reconstruction instead of cross-correlation, tracking methods are applied to the particle clouds, were explored by Novara and

1

Scarano (2013), among others (Schröder et al. (2011), Doh et al. (2012), Fuchs et al. (2016)) in an attempt to combine the advantages of both techniques. In the last years much research has shifted towards particle tracking approaches.

3D PTV

Fully 3D measurements in the version of 3D PTV was introduced in the early nineties (Maas et al. (1993)), and relied on a triangulation procedure using epipolar lines to deduce the volumetric particle distribution on each evaluated time-step. However, these measurements were limited to very low seeding density, otherwise they resulted in too many false reconstructions - ghost particles.

Development Step	Research group	3D Technique	Application	Domain Size [mm^3]	Freestream speed
Introduction of Tomo-PIV	Elsinga et al. (2006)	Tomo-PIV	Cylinder wake	40x40x10	5 m/s
Early application to complex flow structures	Scarano and Poelma (2009)	Time-Resolved Tomo-PIV	Cylinder wake vorticity	80x90x20	2 cm/s
Application to Large-Scale	Kühn et al. (2012)	Large-Scale Tomo-PIV	Convection cell	840x500x240	-
Hybrid Tomo + PTV	Doh et al. (2012)	Tomo-PTV	Ring vortex	35x35x7	Synthetic data
Multi-Pulse Tomo-PIV for high speed	Lynch and Scarano (2014)	Tomo-PIV	Axissymetric BFS model	65x35x10	20 m/s
3D LPT for high particle densities	Schanz et al. (2016)	IPR + STB	Low speed jet	30x30x50	1 m/s (Jet exit velocity)
Scanning 3D LPT around complex geometries	Schneiders et al. (2018)	Scanning STB	Introduction - Flow around a sphere	200x150x200	2.5 m/s
Multi-pulse, multi-exposure 3D LPT	Novara et al. (2019)	STB	Turbulent Boundary Layer	80x120x10	15 m/s

Table 1.1.: Volumetric velocimetry progression.

A first step in attaining higher particle image densities for particle tracking methods was the introduction of the Iterative Particle Reconstruction Wieneke (2012), which extended the working range of single time step particle position

reconstruction, compared to standard triangulation. IPR makes use of residual images, created by backprojecting the triangulated particle cloud. In this step the use of a calibrated Optical Transfer Function (OTF) Schanz et al. (2012) describing the image properties of the particles was an important development to avoid artificial residuals and further improve the algorithm's performance.

Following these developments, the Shake-The-Box (STB) algorithm was introduced for 3D particle tracking at high particle densities Schanz et al. (2016). STB introduces temporal information into the IPR processing of each time step, by predicting a particle cloud for each consecutive time step of its time-resolved version. The combination of these developments enabled a reduction in the computational cost compared to tomographic based reconstruction and 3D cross-correlation, causing the last years trend of this technique becoming more popular.

The extensions to STB have been similar in nature to the extensions to tomo-PIV. One development that offers increase in the measurement volume was the introduction of the scanning volumetric approach based on co-axial imaging velocimetry system mounted on a robot arm (Schneiders et al. (2018)). Further the application to higher speed flows came in the form of multi-pulse STB measurements, for example the measurement by Manovski et al. (2021) at M = 0.506 and 0.845. The table is concluded with the introduction of multi-pulse, multi-exposure systems by Novara et al. (2019), a technique that provides potential for measurements at high particle density and high speed at reasonable experimental complexity.

Despite ongoing work, especially in topics such as uncertainty quantification (Discetti and Coletti (2018)), volumetric velocimetry is an established technique at the laboratory level. It is clear from this outline that it is mostly deployed to do turbulence research in low-speed flows, where time-resolved measurements can be afforded.

In order to perform volumetric velocimetry investigations in relevant environments for advanced aerodynamic development around complex geometries, a number of advances need to be made. The overarching goal of this thesis is the extension of the volumetric velocimetry to such measurements, where large volumes and a range of speeds are measurable with increased robustness, comprehensiveness and accuracy. Before breaking down this goal into more tangible objectives, a review of large-scale volumetric velocimetry in industrial environments is given in the following chapter.

2

LARGE-SCALE VOLUMETRIC VELOCIMETRY

2.1. BACKGROUND

The application of advanced flow measurement techniques like PIV in industrial environments is important for several reasons, primarily that it enhances realism and relevance, measuring flows that are more directly applicable to real-world design optimization, and capturing complex flow phenomena that are not present in simplified models.

However, while a powerful diagnostic tool, as argued in Chapter 1, the application of PIV in industrial wind tunnels presents several mismatches with the demands of industrial testing. These are considered here in terms of - measurement complexity and robustness, measurement accuracy, measurement time, data processing time, and data reduction.

Standard pressure and force balance measurements are very reliable and provide high accuracy readings, which depending on the type of sensor used these are down to 0.1% of the full-scale value (Barlow et al. (1999)). Additionally, once calibrated and set up, the measurements are very quick, in the order of a few seconds, allowing for quick configuration changes. Finally, signal processing is typically done online, which means that there is a high reliability of the measurement, as there is more opportunity for correction in case of mistakes. Further data reduction and post-processing is typically highly standardized and uses performance parameters that are widely accepted such as pressure coefficients, lift and drag coefficients, etc.

For PIV, the measurement complexity is relatively high in comparison, with lower robustness due to the increased chance of technical failure of any of the involved components. One considerable technical challenge is related to the need for introducing seeding into the flow. Achieving uniform and sufficient seed-

ing across the typically large test sections of industrial facilities is a significant challenge. Progress has been made, especially with regard to the generation and control of helium-filled soap bubbles (HFSB) (Scarano et al. (2015), Caridi et al. (2016), Faleiros et al. (2019)), as is covered in more detail in the following section. However, the case remains that seeding with HFSB requires significant effort, and introduces the possibility of the pollution of the model that might be instrumented with sensitive probes, as well as of the tunnel circuit.

The measurement time for PIV/PTV is comparable, slightly higher, in the order of 1 minute per datapoint (i.e. a full 2D or 3D flow field composed of hundreds of thousands of vectors, corresponding to one condition in the measurement matrix) for low-frequency (10 Hz) systems. This is also related to the measurement completeness, which is affected by the optical blockages and reflections present if measuring around test objects. The standard solution to achieve measurement completeness, as is expanded further in the next section, features scanning. However, if scanning methods are employed, the time scales up with the number of scanning regions of interest, making the study of many different configurations difficult.

Data processing for PIV features relatively complex algorithms. Typically, limited online processing is possible and if so, it requires expertise. Part of the reason has to do with the sheer volume of data generated by PIV - depending on the type and number of cameras used this can reach up to a few Gb/s. Quick validation of the data is typically conducted by using sub-optimal processing parameters that allow fast processing, possibly in a small region of the full measurement domain, and using a sub-set of the full set of the acquired data.

Finally, for the data reduction, longer data interpretation time is required as compared to more straightforward analysis methods from traditional sensors. Additionally, there are no widely accepted performance parameters well known among the aeronautical community at large. Relatively specialized aerodynamic knowledge is needed to interpret vorticity and Q-criterion, turbulent kinetic energy, Reynolds stresses, or the interpretation of modal decomposition sometimes used to gain insight into the flow dynamics.

In this thesis the topics of the measurement robustness, measurement time, spatial completeness, and velocity determination accuracy are addressed.

First an overview of the state-of-the-art of PIV in industrial facilities is given.

2.1.1. STATE-OF-THE-ART

When the research summarized in this thesis started, the state of the art in industrial large-scale velocimetry measurements is represented by the measurement of Faleiros (2021), a photograph from which is shown in Figure 2.1. Quasi-volumetric measurements were achieved by a scanning approach in the wake of

a tilt rotor in the 9.5 x 9.5 m^2 test section of the LLF, DNW. The progress this measurement represents is in terms of its scale and impact. It also allowed to identify possible directions of improvement. For example, the scanning approach was found to increase the overall measurement time and complexity, favoring a potentially fully volumetric, single acquisition approach. Despite the scale, the measurement was performed in the wake of a rotor, where optical access is clear. If data around the model was needed, the blocked optical access of the cameras around the complex geometry would not allow for it. Finally, the double-pulse measurement made it possible to acquire data at the relatively high speed of 60 m/s, however this type of measurement only allows for limited velocity determination accuracy and a limited range of velocities that can be measured (Adrian (1997), Raffel et al. (2018)).

Each one of these factors is revisited in more depth in the remainder of this chapter, however, for a broader idea about the state of the art, Table 2.1, summarizes some large-scale measurements at industrial facilities, or on-site, from the last years.

Figure 2.1.: Photograph from PIV tilt rotor measurement at the LLF, DNW, Faleiros (2021).

Research group	Technique	Wind Tunnel	Application	Domain Size	Freestream speed
Carmer et al. (2008)	2D PIV+Traverse	Free flight lab, ONERA	Wake vortex system study	$2m^2$	-
Bosbach et al. (2009)	2D PIV + HFSB	Aircraft cabin mock-up	Convection	12.6 m^2	-
Wadcock et al. (2013)	Stereo-PIV	NFAC, NASA	Wake of full-scale rotor	4 x 1.16 m^2	33 m/s
De Gregorio et al. (2012)	Stereo-PIV+Traverse	LLF, DNW	Helicopter rotor	1 x 0.35 m^2	M = 0.25
Sciacchitano et al. (2018)	3D Robotic	LST, DNW	Turboprop aircraft	0.58 m^3	8-50 m/s
Kempaiah et al. (2023)	Stereo-PIV	LST, DNW	Turbofan inlet	0.25 x 0.25 m^2	M = 0.2
Erdogdu et al. (2024)	Stereo-PIV+Traverse	Volkswagen	Automotive/Car Wake	1.7 x 1.5 m^2	38 m/s
Kuratani (2024)	Stereo-PIV	Honda	Automotive	0.3 x 0.3 m^2	27 m/s
Birvalski et al. (2024)	Stereo-PIV	On Site	Ship Propeller Inflow	0.65 x 1.4 m^2	5 m/s (Ship speed)

Table 2.1.: Large-Scale PIV Experiments in Industrial Facilities.

The applications chosen to be summarized here feature complex geometries that are representative of the actual full-scale models.

The measurement of Carmer et al. (2008) is quite a unique application at ONERA, where the wake vortex system of an aircraft was studied in a catapult facility. In a fairly complex measurement, they used a multi-camera setup traversed to study different sections of the wake. The measurement by Bosbach et al. (2009) presents one of the first approaches to large-scale PIV using HFSB as tracer particles. In this experiment it was possible to measure turbulent convective airflows on the scale of 12.6 m^2, overcoming limitations of traditional PIV setups. The experiment was conducted in a full-scale cabin mock-up to validate CFD codes. Another large-scale measurement was performed at NASA by Wadcock et al. (2013), where the wake of a full-scale rotor in forward flight was measured. Several large-scale PIV measurements have been performed at DNW, including the helicopter rotor measurements of De Gregorio et al. (2012) with a cameras and laser traversing system, the measurement around a turboprop by Sciacchitano et al. (2018) with robotic volumetric velocimetry, and the more recent turbofan measurements by Kempaiah et al. (2023) to study the flow in a turbofan inlet. Water measurements behind a ship propeller at full-scale using natural sediments as particles are reported by Birvalski et al. (2024). Additionally large scale measurements from the automotive sector were performed by Erdogdu et

al. (2024) and Kuratani (2024).

This table is not exhaustive, but it does attempt to be representative of large-scale PIV in industrial facilities. A few observations can be made based on the commonalities between these measurements - these are typically 2D or stereo measurements; quasi-3D data is obtained by plane scanning or full 3D data by volumetric scanning with co-axial systems mounted on a robotic arm. The measurements typically employ the more robust 2-pulse system, which is suitable for measurements at the higher velocities, up to 60 m/s.

Moving towards the goal stated in the previous chapter, that is towards full-field volumetric measurements in these complex applications, requires the consideration of a number of factors. In the following, tracer particles, optical access around complex geometries and PIV system performance are considered in more detail.

HFSB

For volumetric particle velocimetry efficient scattering tracers are essential, as the illumination intensity rapidly decays if the light is expanded over a large cross section. Additionally, to image particles in focus, the local depth of field of the cameras must be greater than or equal to the illuminated volume depth.

The focal depth is proportional to $f_\#^2$ (Equation 1.12), with $f_\#$ being the f-stop, indicating the ratio of focal length f to lens aperture diameter D. It follows that for a given focal length, the amount of light passing through the lens scales with $f_\#^{-2}$, further lowering the light intensity captured by the camera sensor. Lastly, when the particle image is diffraction limited, the particle image diameter is directly proportional to $f_\#$ (Equation 1.10, 1.11). A larger particle image diameter yields a reduced peak particle intensity.

The combination of the these factors, namely the light expansion into a volume, the necessary focal depth and the increase in diffraction, presents a real challenge to large-scale 3D PIV measurements (Jux (2022)). From the outline relations presented in the Imaging section of Chapter 1, it follows that peak particle intensity is inversely proportional to the fourth power of the measurement volume depth for a chosen optical magnification (Raffel et al. (2018)). Therefore scattering-efficient tracers with relatively large diameter but density equivalent to the fluid density are the preferred choice for large-volume measurements.

When HFSB are illuminated, the light rays reflected on the bubble soap film towards the recording medium form two glare points, resultant from reflections occurring externally and internally of the bubble. Depending on the magnification factor, if the bubbles diameter is resolved in several pixels the two bubble glare points are plainly visible. For large-scale PIV, because of the small magnification, the glare points merge, forming a single particle image, as can be seen in the far

left of Figure 2.2. Recent research by Grille Guerra et al. (2024) demonstrates that the light scattered by these tracers significantly increases with particle diameter increase, opening up possibilities for even larger measurement domains.

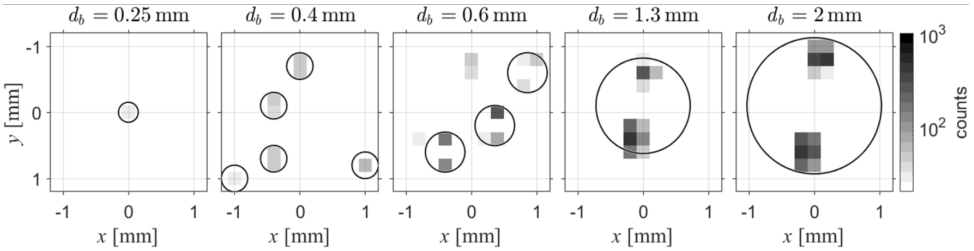

Figure 2.2.: Low-magnification recordings (M = 0.1) of the light scattered by HFSB tracers. The black circles are the estimated positions of the bubbles. Plot from Grille Guerra et al. (2024)

The HFSB particle image area after merging, considering only diffraction, may be approximated to the area of an ellipse, extended along the axis passing through both glare points. For narrow apertures at meter-scale field of view, the particle image diameter may be approximated to d_{diff}.

For applications in air flows, HFSBs have first been employed at large-scale in the measurement by Bosbach et al. (2009). Caridi (2018) demonstrated that the HFSB tracers scatter approx 10,000 times more light compared to conventional μ-sized PIV tracers. The response time of a nominal 0.3 mm diameter HFSB tracer is reported within 10-30 μs by Scarano et al. (2015). Likewise, Faleiros et al. (2019) reports larger HFSB of 0.5 mm diameter with a similar response time.

HFSB are typically generated by coaxial, orifice-type nozzles following the initial design of Bosbach et al. (2009). An illustration of the generator architecture along with a photograph of a HFSB rake with 400 of these generators, are shown in 2.3.

A fluid supply unit controls the flow rates of air, helium and soap solutions provided to the generator. Faleiros et al. (2019) studied the impact of the relative flow rates on the bubble characteristics, in terms of size, production rate and buoyancy. Depending on the operating conditions and nozzle design 10,000 - 70,000 tracers/sec are produced by one nozzle. Such high production rates are necessary for seeding the relevant measurement volumes. Rakes housing multiple nozzles are designed to enhance the tracer particle concentration. Faleiros (2021) presented a 400 nozzle, 3x3 m^2 cross section HFSB seeding system for the tilt-rotor measurement.

Some representative large scale experiments featuring HFSB are summarized in Table 2.2. Depending on the experimental facility where the measurements

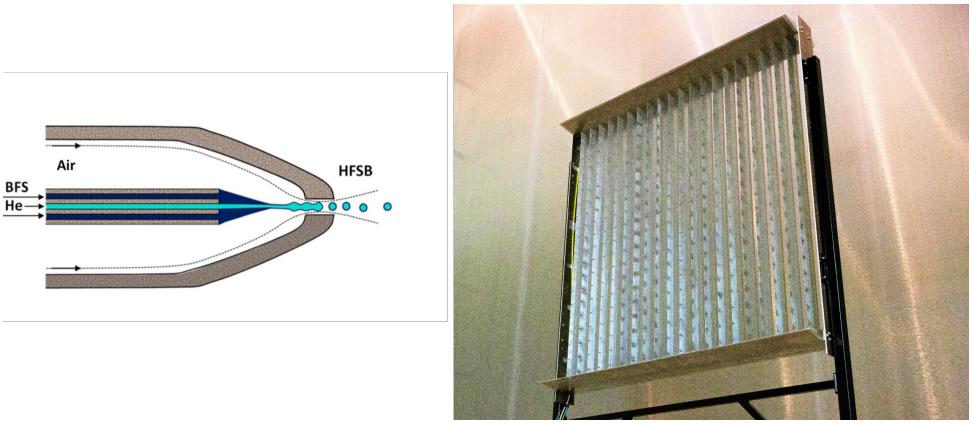

Figure 2.3.: Left: Schematic illustration of an HFSB generator used by Faleiros et al. (2018), Right: NLR seeding rake of 400 bubble generators, 20 wings and cross sectional area of 9 m^2

have been conducted, they have been split in three categories: Room enclosure measurements, i.e. where no freestream flow was present; On-site measurements, with a representative measurement from the Ring of Fire approach by Spoelstra (2022), Spoelstra et al. (2019); and Wind tunnel experiments.

From the first category, measurements are focused on the study of flow physics, such as the convection flow study by Huhn et al. (2017), the spreading of aerosol particles from a breathing mannequin by Schröder et al. (2022), and the free-flight quadcopter drone by Wolf et al. (2024). All of these measurements are similar in that very high quality, and highly resolved data is obtained in both space and time.

The on-site and wind tunnel measurements are more challenging as far as experimental setup and measurement time are concerned. Additionally, they are typically conducted around complex geometries. For the volumetric (Jux et al. (2018)), or quasi-volumetric (Faleiros (2021)) cases scanning, traversing or multiple successive 3D systems (Schanz et al. (2019)) are employed, with the exception of Hysa et al. (2023), an experiment performed in the context of this thesis, and further elaborated in Chapter 5.

Research group	Technique	Experimental Facility	Case Study	Domain Size	Freestream speed
Huhn et al. (2017)	3D LPT	Convection chamber	Convection	0.6 m^3	-
Schröder et al. (2022)	3D LPT	Room enclosure	Breathing mannequin	$12m^3$	-
Wolf et al. (2024)	3D LPT	Room enclosure	Hovering quadcopter	$1.5m^3$	-
Spoelstra et al. (2019)	Stereo-PIV	*On Site*	Cycling drag determination	2 x 2 m^2	-
Jux et al. (2018)	3D Robotic	TU Delft OJF	Full-scale cyclist	2 m^3	14 m/s
Schanz et al. (2019)	Three successive 3D LPT systems	AWM Munich	Turbulent Boundary Layer	0.58 m^3	7 m/s
Faleiros (2021)	Stereo-PIV+Traverse	LLF, DNW	Tilt rotor aircraft	1.1 x 1.1 m^2	60 m/s
Hysa et al. (2023)	3D PTV	LST, DNW	Thrust-Reverser Flow	0.6 m^3	10 m/s

Table 2.2.: Large-Scale PTV/LPT Experiments with HFSB

2-PULSE STB

As far as range of application of PIV systems is concerned, the most widespread version of PIV used in more complex industrial applications is double-pulse, double-frame PIV. This is primarily due to its relative simplicity and the range of velocities it allows to measure.

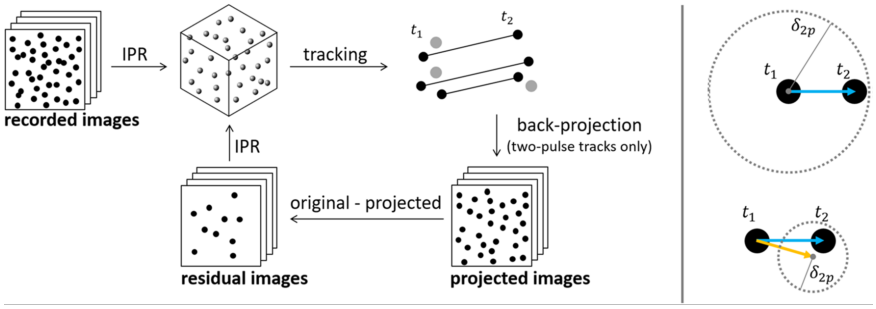

Figure 2.4.: Left: iterative processing strategy for 2P STB; two pulse tracks are indicated in black, untracked particles in gray. Right: particle tracking scheme without (top) and with (bottom) the aid of a displacement predictor (orange arrow). Figure from Novara et al. (2023).

The adaptation of STB to two-pulse recordings was introduced by Novara et al. (2023), where to compensate for the lack of a large number of recordings, the

method makes use of an iterative strategy where the sequential application of Iterative Particle Reconstruction (Wieneke (2012)) and predictive particle tracking by Particle Space Correlation are used to progressively reduce the complexity of the object to be reconstructed and increase the number of successfully retrieved particle tracks. A schematic representation of this coupled approach is shown in Figure 2.4.

Despite the larger volumes afforded by employing HFSB, and the advances in 3D particle reconstruction and tracking algorithms, there are multiple challenges that remain in order to perform complex measurements at high technology readiness levels in industrial wind tunnels. In the following sections, the aspects of PIV that are relevant to this goal are presented.

2.2. OPEN QUESTIONS IN VOLUMETRIC PTV

2.2.1. OPTICAL ACCESS AROUND COMPLEX GEOMETRIES

A frequently encountered bottleneck in volumetric measurements is the limited spatial coverage around complex model geometries, arising from restrictions in optical access.

A measurement volume in 3D particle imaging is achieved by ensuring that the entire region of interest is illuminated and imaged clearly without obstructions or distortions.

When attempting to achieve spatially comprehensive data around geometrically complex models a number of challenges arises, which are summarized below:

- **Shadows** Illumination of any opaque object results in shadows in some parts around the object. Their exact configuration depends on the geometry and the direction of the illumination source, but if these shadows are present within the domain of interest, the motion of the tracers in these regions cannot be tracked.

- **Blocked line of sight** Similarly to the illumination, complex shapes such as those found in engines, aircraft geometries or wind engineering, have parts of the geometry that will obstruct the cameras' lines of sight, preventing clear imaging of the flow field. Physical obstructions such as objects with curvature, can block the view of certain areas making it impossible to capture the particles' motion in those areas.

- **Increased experimental setup complexity** The typical experimental guidelines for PIV are tailored towards the study of phenomena around simpler geometries, so careful considerations and availability to (potentially) extra

equipment are needed when designing experimental setups where comprehensive measurements are desired.

- **Image quality and reflections** Image processing becomes more challenging with complex geometries as different parts of the object will almost certainly cause reflections in some of the cameras.

- **Image processing complexity** Most of the particle reconstruction and tracking algorithms have been designed for clear line of sight of the cameras, therefore necessitating additional considerations regarding the processing algorithms logics.

- **Incomplete flow dynamics** The ability to capture the full flow dynamics is hindered for spatially incomplete data, making it challenging to understand the entire behaviour of the fluid around the geometry, which is particularly interesting given the possibility of employing techniques such as modal decomposition.

Due to the combination of some or all of the above, only portions of the flow field are visible or able to be processed, leading to typically incomplete data. The separate losses from shadows, cameras lines of sight or inability of the processing algorithm to analyse parts the acquired data, are losses that are compounded. Furthermore, these losses are not systematically quantified in the available literature, making it difficult to perform detailed investigations. If spatially comprehensive measurements are to be achieved, there is a need for a theoretical framework for understanding and quantifying these losses.

2.2.2. PIV SYSTEM PERFORMANCE

The spatial resolution and velocity measurement error for a given time delay dt between two recordings are defined relative to the linear dimension of the field of view l_x and the maximum allowable particle displacement Δx_{max}. These are represented as the dynamic spatial range DSR and the dynamic velocity range DVR from Adrian (1997):

$$DSR = \frac{l_x}{\Delta x_{max}} = \frac{L_x/M_0}{\Delta x_{max}} \tag{2.1}$$

and

$$DVR = \frac{u_{max}}{\sigma_u} \tag{2.2}$$

where M_0 is the image magnification, $L_x = l_x M_0$ is the linear dimension of the image sensor, u_{max} is the maximum measurable velocity within the domain, and σ_u is the minimum resolvable velocity for a given image particle diameter.

From the combination of these expressions, a parameter which is commonly accepted to define the performance of a PIV system is defined as the product of DVR and DSR (Westerweel et al. (2013)).

It follows from this that the performance of a PIV system is increased by increasing the sensor size and/or by decreasing the minimum resolvable velocity. The latter comes down to decreasing the particle centroid location uncertainty, as the particle diameter is limited to diffraction limited imaging (as elaborated on the HFSB Imaging section).

The physical size of the digital camera arrays has been increasing slowly. For example sCMOS cameras operating at double-frame have 5.5 MPx resolution, with a pixel pitch of 6.5 micrometers, and 16-bit depth for a large dynamic range, at very low noise imaging levels.

Decreasing the minimum resolvable velocity is an issue particularly for 2-pulse recordings, where accuracy is limited to two instances of the particle imaging along its trajectory, as expressed schematically in Figure 2.5. The sampling of the particle in multiple instances, as is the case in multi-pulse systems, opens the possibility for higher order interpolations, which provides a better estimate of the particle's trajectory, thus improving performance.

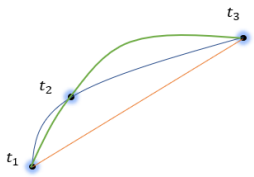

Figure 2.5.: Trajectory of a particle (green) and particle images at three instants. The shaded regions centered on the path line qualitatively represent the probability of measured image locations at each instant, with the locations of the measured image centers found by image analysis indicated by the small black dots. The blue line is the interpolated 3-pulse curve, and the orange line is the conventional linear two-pulse interpolation.

Additionally, multi-pulse or multi-frame techniques improve the probability for correct pairing by tracking particles over more than two successive frames.

Whereas the sensor size is a question of further camera technological development, or simply availability of equipment, there is room for improving the 2-

pulse PIV system performance by the increased sampling of the particle along its trajectory through multiple pulse recordings.

2.3. PIV CONFIGURATIONS

For PIV investigations the design of an experimental setup must be based on the priority of the measurement given the case specific constraints due to technical limitations in available laser power, pulse repetition rates, camera frame rates, etc, followed by the constraints that are imposed by the storage limitations and image evaluation methods.

Often there are also constraints in the components that are already available in the laboratory or that can be easily obtained for the experiments.

Depending on the choice of priority an appropriate system for recording can be configured based on the desired spatial and temporal resolution, desired accuracy of the velocity measurement, experimental components cost, ease of integration or complexity, scale of the domain that needs to be covered and overall measurement time.

So far the basics of illumination, imaging and processing have been covered. Depending on the type of imagers and the illumination strategy employed, different types of measurements are possible.

SCANNING AND FULL-FIELD PIV

As remarked in the beginning of this chapter, scanning approaches are relatively common in industrial environment measurements, either to construct quasi-volumetric data from planar measurement, or to increase the overall measured domain.

One approach to increasing the volume size was developed by Schneiders et al. (2018) in the form of the coaxial volumetric velocimeter. The measurement device consists of a fixed and precalibrated system of four cameras and a volumetric laser illumination installed in a common housing. The light reflected by the tracers is recorded by the four cameras and particle trajectories are reconstructed using STB. The device is pointed at a region of interest and operated for a certain time, yielding LPT results in a volume of up to 30 liters. Larger volumes are scanned by moving the system on a robotic arm, scanning around the object of interest. One industrial application of the method is the measurement of the flow around a turboprop by Sciacchitano et al. (2018), full combined volume shown in Figure 2.6.

The downsides of the method are the low position accuracy in the depth direction (due to the limited tomographic angle of the camera views) and the restriction to averaged data due to the scanning approach. Additionally because

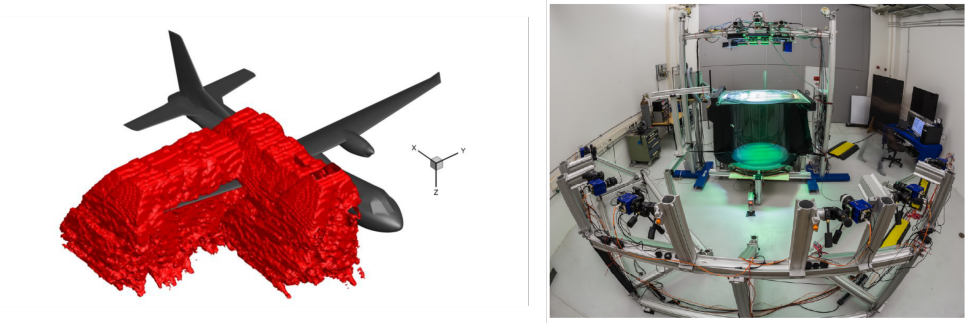

Figure 2.6.: Left: 3D Robotic Scanning around a turboprop model Sciacchitano et al. (2018); Right: 3D LPT measurement in convection cell Huhn et al. (2017).

of the time required to scan the whole volume, which scales up with the volume size, the overall wind tunnel time is increased, increasing operational costs and imposing stricter requirements in terms of maintaining steady flow conditions over extended times. In his PhD thesis Jux (2022), reports that at around 2 m^3, this technique reaches its volume limit.

Instead, the term 'full-field' approach is used here to indicate a type of measurement where the entire measurement volume is captured in a single acquisition, as is the case on the right of Figure 2.6. In this specific case this approach is less challenging due to the lack of test objects and therefore clear optical access. This approach is preferred in this thesis due to several advantages that it offers, namely: complete measurements in minimal time; possibility for unsteady global analysis of the instantaneous recordings of time-averaged data by methods such as modal decomposition; and the possibility of scaling up the volume to the maximum allowed by the available laser energy and practical camera placement. The main disadvantage, especially when measuring around complex geometries, is that optical blockages can become limiting in terms of the measurement domain comprehensiveness, making this a point worthy of special attention. This is an issue addressed in this thesis.

TIME-RESOLVED AND STATISTICAL PIV

Time-resolved PIV is widespread in fluid dynamics research typically in laboratory environments. The dynamic content provides temporal as well as spatial information. The temporal information can be exploited to enhance the DVR of the measurement, as is done in multi-frame PIV (Hain and Kähler (2007)), or in the pyramid correlation (Sciacchitano et al. (2012)).

From these time-resolved series further analysis are possible such as accelerometry, space-time correlations, frequency spectra of turbulence, and the potential for derivation of pressure and force fields. In combination with volumetric methods and data assimilation, a full four-dimensional description of the flow is achievable.

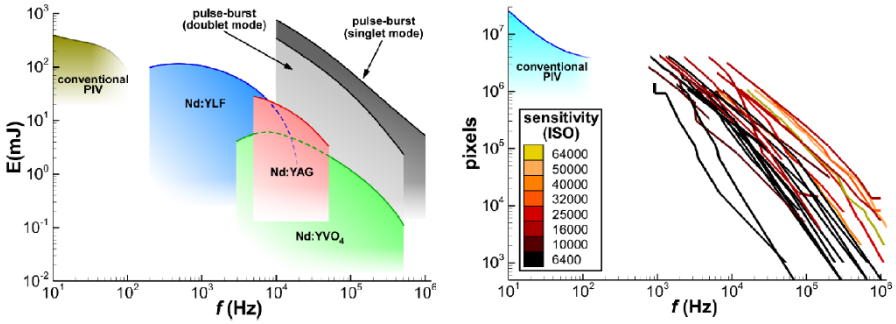

Figure 2.7.: Range of capability of current TR-PIV equipment; Left: energy vs frequency of high-repetition lasers; Right: number of pixels vs framing rate of high-speed cameras. Beresh (2021)

The technological trends in camera and laser technology are depicted in Figure 2.7, from the review of Beresh (2021). Excepting cost, which increases considerably moving from left to right in the plot, for increased laser repetition rate, the pulse energy drops considerably. For the imaging, modern cameras allows the user to reduce the window size of the image sensor to boost framing rate, however at some point the small number of pixels available may become prohibitive to obtain sufficiently descriptive recordings. Accuracy considerations are another concern, as noise is typically higher in high-speed cameras (Raffel et al. (2018)).

In contrast, for statistical, double-pulse double-frame PIV, labeled 'conventional' PIV in this plot, high pulse energies in the order of hundreds of mJ are typically available, as well as large camera sensors in the order of MPx, albeit at low repetition rates, in the order of 10 Hz.

The high pulse energies allow for the illumination of large-volumes, which is of interest in large-scale applications, and the larger camera sensors (especially when combined with small pixel pitch) allow for a high DSR.

Time-averaged data is typically used for comparison with the results of numerical simulations or other measurement techniques. Additionally, apart from the mean flow fields, accurate flow statistics can also be retrieved, which is of interest particularly in inhomogeneous turbulent flows around complicated geome-

tries (Westerweel et al. (2013)). Because of this, the character of the experiments differs from measurements of instantaneous fields in that accuracy is of greater importance.

The main disadvantage of low-speed PIV systems is the limited velocity determination accuracy and DVR.

SINGLE-EXPOSURE AND MULTIPLE-EXPOSURE PIV

PIV images can be recorded in a variety of modes, changing the number of frames and light exposures per frame. Following Raffel et al. (2018), two main categories can be defined: methods that capture the images of the illuminated particles at multiple times onto a single frame and methods which provide a single image of the illuminated particle distribution for each time of the illumination.

Any combination of camera frames and exposures is possible. Single-frame, multi-exposure was historically used with photographic PIV (Adrian (1986), among others), but was eventually replaced with single exposure measurements with digital cameras due to the processing simplicity.

Double-frame, single exposure is used widely for a variety of measurements as already elaborated in the previous sections. Approaches to improve the DVR of this technique in its single-exposure version include the Multi-Δt version introduced by Saredi et al. (2020). In this category also belong double-frame multi-pulse systems that use strategies to separate multiple pulses into different sets of cameras, albeit at much increased experimental complexity, used by Novara et al. (2016).

Double-frame, double-exposure was investigated by Novara et al. (2019), as an approach to reduce the complexity of multi-pulse systems by using a single set of cameras.

Multi-frame, single-exposure describes most of time-resolved recordings, and in theory it is also possible to acquire in multi-frame, multi-exposure in order to potentially further increase the sampling rate.

The specific interest in parts of this thesis is with multi-pulse, multi-exposure approaches, which would allow to further enhance the precision in estimating the flow velocity, by relying on the temporal smoothness of the particle trajectory and the regularity of the image signal. Additionally multi-pulse or multi-frame PTV techniques improve the probability for correct pairing by tracking particles over more than two successive instances.

2.4. RESEARCH GOALS AND SCOPE OF WORK

The role and further potential of large-scale volumetric PIV for modern aerodynamic development has been discussed in Chapters 1 and 2. Despite the already

advanced technique capabilities, its application in industrial aerodynamic testing remains limited. The overarching goal of this research project is to further advance large-scale volumetric velocimetry systems with HFSB towards a higher point of robustness and technological maturity, where they can be reliably applied to flows around complex objects within strict measurement time limitations.

While drawing advantages from recent progress in tracer particle technology (HFSB), which allows for measurements in the cubic meter volumes, the approach followed is to extend the spatial comprehensiveness of the full-field volumetric measurements by addressing the problem of blocked optical access, and increasing the dynamic velocity range measurable by two-pulse tracks of two-pulse PIV systems.

In this context, the objectives of the thesis are defined as:

- PTV Technology Developments
  - Extend the spatial comprehensiveness of volumetric velocimetry measurements by targeting the problem of the reduction of the measurement domain around complex geometries due to blocked optical access of the illumination and imaging (Chapter 3).
  - Extend the dynamic velocity range of double-pulse PIV systems by the investigation of multi-pulse, multi-exposure methods (Chapter 4).
- Applications
  - Increase the robustness of large-scale volumetric PIV by means of demonstration experiments in relevant environments (Chapter 5).
  - Demonstrate the impact of spatially comprehensive large-scale volumetric velocimetry measurements that allow for global unsteady dynamics analysis (Chapter 6).
  - Demonstrate the potential of PIV as a complementary approach to traditional wind tunnel testing techniques in order to provide additional flow information (Chapter 5).

This thesis combines the key contributions from the developed methodologies and applications that enhance the capabilities of the technique, presented in the first part, along with applications in a relevant environment with higher technology readiness level, presented in the second part.

In the first part, Chapter 3, extends the application of PTV to applications with model rotation and blocked optical access, most pronounced in the field of wind

engineering. By employing a multi-camera redundant 3D PIV system, the study addresses the challenges posed by restricted optical access around complex geometries.

The second study, Chapter 4 introduces the approach of using multi exposure, as a way to reduce the probability of spurious particle matching, and get improved DVR compared to double-pulse tracks.

In the second part, two advanced applications in the Low-Speed Tunnel of DNW are presented.

The first one, Chapter 5 focuses on the application of volumetric velocimetry to study the flow around thrust reversers mounted on a complete aircraft model.

Lastly, Chapter 6 presents an application of extended PIV systems around a ship at varying incoming wind directions.

Chapter 7 "Conclusions and Outlook" summarizes the main findings of the research and gives the author's outlook for possible future developments.

I

PTV TECHNOLOGY DEVELOPMENT

3

MULTI-DIRECTIONAL REDUNDANT VOLUMETRIC VELOCIMETRY SYSTEMS

1

[1] Parts of this chapter have been published in: Hysa, I., Tuinstra, M., Sciacchitano, A., Scarano, F., van der Meulen, M. J., Rockstroh, T., & Roosenboom, E. W. (2024). A multi-directional redundant 3D-LPT system for ship–flight–deck wind interactions. *Experiments in Fluids*, *65*(8), 126

3.1. INTRODUCTION

A frequently encountered bottleneck of 3D measurements is the limited spatial coverage around complex model geometries, arising from restrictions in the optical access.

A measurement volume in 3D particle imaging is achieved by ensuring that the entire region of interest is illuminated and imaged clearly without obstructions or distortions. This issue is not problematic in laboratory settings where simple geometries are studied, or where the object is kept out of view (e.g. wakes, jets and boundary layers), however optical obstructions become limiting in some large-scale applications. For instance, in the recent 3D measurement around a jet aircraft model Hysa et al. (2023), the domain of interest, around the thrust-reversers, contains several regions of blocked optical access because of the complex configuration, whereby either illumination is missing or the imaging is obstructed. The problem is further exacerbated in the field of wind engineering, where the aerodynamic interaction around groups of objects needs to be evaluated over a range of wind directions (often around 360 degrees).

A variety of techniques have been devised to overcome optical blockage in PIV. Challenging applications such as velocity measurements inside the geometrically complex model of a human carotid were carried out by Buchmann et al. (2011). Measurements in internal combustion engines Fajardo and Sick (2009) and turbomachinery also pose specific problems related to optical access. In multi-phase flows Poelma (2020) succeeded in the measurement of the flow across an opaque medium. Successful extensions to the standard optical techniques include the refractive index matching Uzol et al. (2002) in liquid flows, the use of fluorescent tracers to reduce laser reflections Häfeli et al. (2014), and optical coherence tomography Poelma (2020). Despite their innovative character, these solutions mostly apply to liquid flows, whereas for air flows alternatives remain limited.

In turbomachinery applications single-view 3D PIV and PTV techniques have been based on plenoptic imaging Fahringer et al. (2015). This technique operates with minimal optical access, at the expense of optical aperture and in turn, the precision of particle depth positioning. This highlights the importance of multi-directional imaging as twofold: domain imaging coverage and accurate particle positioning by large-aperture systems. Attempts to improve the latter with a mirror system (multiple-eye PIV) have been proposed by Maekawa and Sakakibara (2018), but its extrapolation to large-scale measurements has not been yet devised.

Other approaches which could effectively extend the measured volume are based on spatial scanning where the measurement volume is covered by non-simultaneous sessions. The work by Hoyer et al. (2005) presents a 3D scanning

PTV approach, albeit at small scale. For large-scale application, scanning stereo-PIV has been demonstrated around helicopter models by De Gregorio et al. (2012), Raffel et al. (2017), and more recently by Faleiros (2021) using HFSB. In all these cases however, obstructed views are omitted, which often limits the measurement domain to a fraction of the domain of interest.

The introduction of robotic volumetric PIV, based on the concept of coaxial 3D velocimetry Schneiders et al. (2018) was demonstrated with the measurements around the complex geometry of a full-scale cyclist model Jux et al. (2018). Furthermore, its application at the German-Dutch Wind Tunnels (DNW) returned the time-average velocity field around a scaled turbo-prop aircraft model Sciacchitano et al. (2018). The robotic manipulation effectively circumvents the optically obstructing elements and allows a rapid positioning of the axial velocimeter. Among the shortcomings of this technique are the lower accuracy along the viewing direction (similar to that of plenoptic systems), the potential aerodynamic interference of the robotic system and the flow field, and the increased measurement time due to scanning. Furthermore, unsteady fluctuations are typically not captured by this approach.

Extending the above optical access techniques to the context of wind engineering, to additionally include the investigation of the unsteady aerodynamic effects, has not been afforded so far. In particular, the study of the unsteady flow behavior above the ship-flight-deck presents a challenge, where the fluctuating wind conditions can adversely affect the launch and recovery of aircraft and UAV from the flight-deck, particularly rotorcraft Zan (2005).

The specific aerodynamic investigation of the flow around a ship has been covered with a number of studies aiming at characterizing the complex and turbulent environment caused by the wind-ship interaction. Previous experimental research on ship aerodynamics and the nature of the air-wake has made use of typically pointwise measurement techniques: multi-hole pressure probes Miklosovic et al. (2011); hot-wire anemometry and laser Doppler velocimetry. Qualitative inspection of the flow was done with smoke flow visualization Kulkarni et al. (2005). Planar PIV, was employed to yield more details about the spatial organization of the flow Rosenfeld et al. (2015), Seth et al. (2021) and recently a dual-plane PIV experiment Zhu et al. (2024) has yielded an increased level of detail in the organization of large-scale turbulent structures. A first study employing tomographic PTV Vidales (2016) was restricted to the rear deck, where the proper orthogonal decomposition method was used to understand the global structure of the unsteady velocity fluctuations.

More comprehensive investigations of this problem are conducted with CFD techniques, which require extensive validation in view of the number of parameters involved (ship geometry, wind direction, atmospheric boundary layer, co-

herence of flow fluctuations). Therefore, solutions are sought that enable comprehensive measurements for comparison and verification. The present work examines the use of a redundant illumination and imaging system to extend the spatial coverage of 3D LPT measurements to include the study of the unsteady aerodynamic effects. For this purpose, two-directional illumination and seven-directional imaging have been deployed for the case study of the wind aerodynamics around a representative ship model.

The article first introduces the problem of optical blockage, as the basis of the measurement volume reduction. In the first section, the relevant parameters governing the problem of illumination and imaging with a redundant system are introduced. Furthermore, the possible system configurations are presented and discussed in terms of the expected measurement performance. The following section describes the experimental apparatus, its configuration and the measurement procedure. The fourth section presents and discusses the results in terms of global flow field topology, with a specific discussion about the behavior at the flight-deck where most literature is focused.

3.2. THREE-DIMENSIONAL IMAGING AND VOLUMETRIC ILLUMINATION

This section introduces the definitions and operations necessary to study the problem of optical blockage for LPT measurements. The geometry used for this assessment is the same as that of the model that was tested in the wind tunnel and it is shown in Figure 3.1. Although the concepts are illustrated using the specific example of the ship geometry at several angles, the analysis reported below, in particular the equations that describe the volume losses remain of general validity and it can be applied to a variety of experiments where a redundant illumination and imaging system is used around a complex geometry.

The following variables are defined: S_i denotes the shadow volume resulting from the i^{th} illumination source, and $V_{tot,S}$ denotes the total shadow region, resulting from a combination of different illuminations. For the imaging, C_i denotes the occlusion region (volume) where the optical access of camera i is blocked, with $V_{tot,C}$ being the total occluded region. The tomographic aperture between sets of cameras i and j is measured by $\beta_{i,j}$. Measurements are performed around the domain of interest (DOI). If a fraction of the domain is not measured, that is considered an imaging loss and is represented by the variable V_{loss}.

In order to quantify the losses in a systematic way, simple elements of set theory are used. These are represented schematically in Figure 3.2. The largest set is the DOI, plotted here as the outlining rectangle. Inside the DOI, sub-sets are

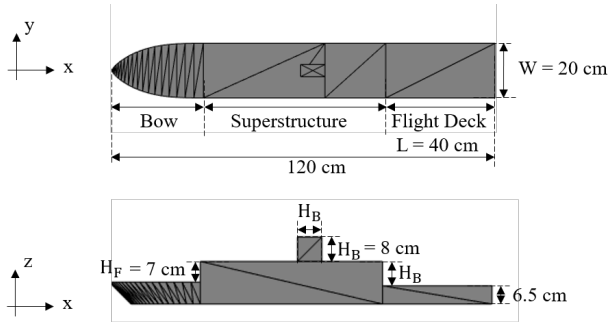

Figure 3.1.: Schematic geometry (at scale) of the ship model along with main dimensions and parts nomenclature.

denoted as circles, named here A and B. These sub-sets that represent the losses regions, can be combined using the operations of intersection - $\cap$ - or union - $\cup$ -, depending on the logics of the case.

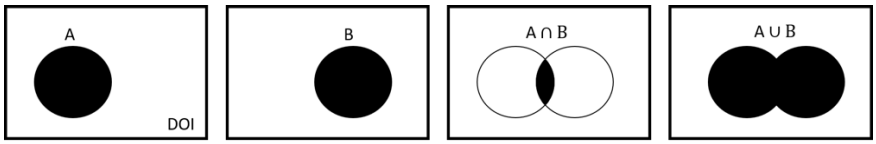

Figure 3.2.: Schematic of the elements of set theory used in the volume losses quantification.

In general, minimizing the intersection between two sets translates to minimizing the number of common elements between them. For the union the opposite is true, minimizing the union is achieved by maximizing the number of common elements between the sets.

3.2.1. CONSTRAINED ILLUMINATION

The problem of optical blockage due to shadow forming is simple in principle, by treating shadows with ray tracing of geometrical optics, under the assumption of parallel illumination. However, the problem complexity arises when a multitude of illumination directions are considered in three-dimensional space, where the illuminated object also undergoes rotation. Redundant illumination is an effective approach to reduce the measurement volume erosion: a region in shadow from a given direction can be illuminated from a second or a third one. On Figure 3.3-top, the shadows around the model are shown for the case of a single illumination, along with the DOI (green rectangle) in the first condition.

The rotation of the model is denoted by the yaw angle γ, and the elevation of the illumination source with respect to the center of the DOI is denoted by the elevation angle α. Shadows are formed at different locations for every orientation of the object. A measurement point is considered valid when data is obtained at all angular positions. The consequence of the latter for the single illumination direction is that almost no point in the domain is imaged at all the rotation steps. The second row illustrates the improved situation by adding a second, orthogonal, illumination direction. The overall losses drop from 75% (additive) with one illumination direction, to 41% with a second illumination.

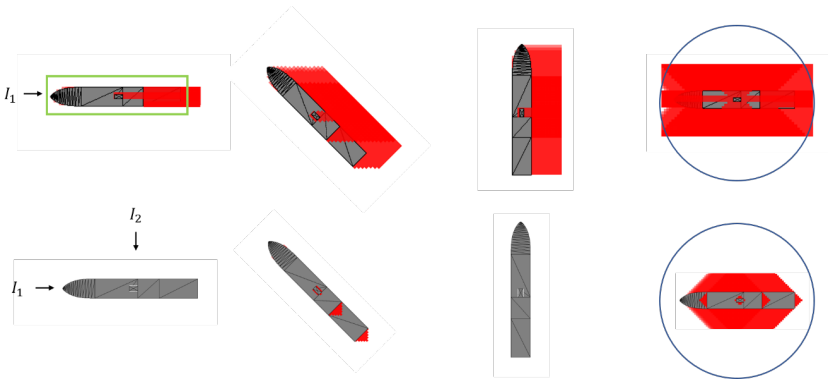

Figure 3.3.: Top view of the shadows (in red) resulting from single (top) and double (bottom) illumination directions. The model is rotated counterclockwise in steps of 45 degrees (from left to right) as to represent different wind conditions. Last image on the right illustrates the cumulative effect over 360 degree rotation at illumination elevation of 0 degrees.

Considering a system illuminated from M directions, the expression of the volumetric losses due to shadows reads as:

$$V_{\text{tot,S}} = S_1 \cap S_2 \cap \cdots \cap S_M \tag{3.1}$$

based on the fact that a region in shadow from a given direction can be illuminated from an M^{th} direction, the total shadowed region is gradually eliminated with the addition of illumination directions. Figure 3.3 illustrates the limiting case of the illuminators being at 0° elevation angle. When the elevation angle is increased, the shadowed volume decreases, as this particular model has a convex geometry. The results from the ray tracing analysis around this model at three different elevation angles are summarized in Table 3.1. Adding a second illumination direction and increasing the elevation angle from 0 to 60° results in a rapid

decrease of the overall volume losses from 75% to 27% of the DOI.

(α)	Yaw angle (γ)	$V_{\text{tot,S}}$ #1	#2
0°	0°	9%	0.2%
	45°	16%	2%
	90°	14%	0.2%
	(0:45:360)°	**75%**	**41%**
30°	0°	2%	0.2%
	45°	11%	1%
	90°	10%	0.2%
	(0:45:360)°	**48%**	**35%**
60°	0°	1%	0.2%
	45°	6%	0.5%
	90°	6%	0.2%
	(0:45:360)°	**33%**	**27%**

Table 3.1.: Summary of volume losses for a full rotation of the model, with varying number of illumination directions and elevation angle

3.2.2. IMAGING IN THE PRESENCE OF OBSTRUCTIONS

In the present section the concept of optical access to a complex object from several directions is discussed with the purpose of explaining different approaches and options to imaging. As discussed in the literature, systems for 3D particle tracking typically comprise 3 to 4 cameras, which subtend a solid angle such to accurately triangulate the position of the illuminated particle tracers in physical space. In the present discussion, the algorithm Shake the Box (STB), used for LPT is considered as a baseline for the analysis of the images set Schanz et al. (2016). Although a number of methods and variants of particle tracking exist and have been proposed in the literature (most notably, Maas et al. (1993), among others), STB is a prominent technique, which has been rapidly adopted in the experimental fluid mechanics community Schröder and Schanz (2023). The use of 3 to 4 cameras is typically reported as sufficient to accurately describe particle distributions resulting in an image seeding density in the order of 10^{-2} to 10^{-1} particles per pixel (ppp). The losses that would result from a standard three camera volumetric system are illustrated in Figure 3.4, for three rotation angles that correspond to those considered for the illumination in the previous section, as well as the total. For the sake of clarity only a plane at the ship mid-height is plotted, under the simplification of parallel imaging.

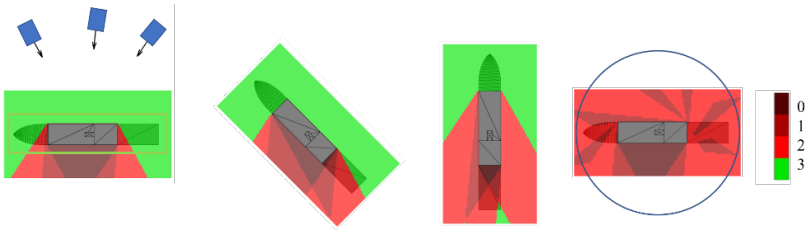

Figure 3.4.: 3D Imaging around the ship model at rotation of 0,45, 90 degrees and full rotation additive (left to right) plotted on a plane at the mid-deck height. The different colors represent the number of cameras with clear optical access at any given region.

Flow measurements can only be performed within regions in view by all the cameras; hence the total losses due to optical blockage are in fact equal to the combination, i.e. union of all the individual camera losses (as opposed to the intersection in the case of illumination) expressed in Eq. 3.2.

$$V_{\text{tot,C}} = C_1 \cup C_2 \cup C_3 \tag{3.2}$$

Since the losses are combined, a minimal geometrical loss scenario is achieved when the individual losses intersect maximally, i.e. when the cameras are placed as close to each other as possible, coaxial imaging ($\beta_{i,j} \rightarrow 0$). However this is detrimental for the reconstruction accuracy Scarano (2012).

In all tomographic imaging systems where the total number of cameras is equal to the number of cameras needed for reconstruction, there is a conflict between minimizing losses and maximizing reconstruction accuracy, as $\beta_{i,j}$ increases $\rightarrow$ V_{loss} increases.

The total measurement volume that is not accessible to measurements is a result of either a shadow from the illumination, or the cameras' blocked line of sight and can be defined as:

$$V_{\text{loss}} = DOI \cap (V_{\text{tot,S}} \cup V_{\text{tot,C}}) \tag{3.3}$$

An overview of the total losses for a system comprising three cameras and a single illuminator is given in Table 3.2. It should be remarked that these values are problem dependent and as such, they only give an impression of the typical losses, rather than to provide exact figures. The actual value of the volume loss is strongly dependent on parameters such as object shape and connectivity, cameras and laser positioning. Additionally, the same situation that was presented previously for the elevation angle of the illumination, is valid here for the cameras. It is clear that in the present case the losses for the full rotation of the

model completely hamper the measurements, while at each position they may still be considered as acceptable. This motivates the analysis of redundant imaging systems, where more imaging directions are necessary in order to extend the measured volume, which is presented in the following section.

Model yaw angle	$V_{tot,C}$	$V_{tot,S}$	V_{loss}
0	21%	9%	23%
45	24%	16%	32%
90	41%	14%	51%
(0:45:360)	100%	75%	100%

Table 3.2.: Losses for a three camera, one illumination 3D LPT system

REDUNDANT IMAGING

In the present context, a 3D particle imaging system is denoted as redundant when the number of cameras (viz. views) largely exceeds the above minimum of three.

A redundant system can be operated in two different modes, depending on the logics imposed for the detection of a particle. In the monolithic mode a particle tracer is detected if its image is found on each image of the set. Conversely, a partitioned system splits the camera set into independent subsets. Each subset operates separately to detect particle images. A consequence of the monolithic approach is that when a tracer is not in view from one of the cameras (e.g. if the view is blocked by the presence of a solid object) the particle is not detected. The same rule applies to a partitioned system, but to each subset separately.

A monolithic system therefore, can potentially reconstruct particle fields at high concentration with minimal occurrence of ghost particles Elsinga et al. (2011). However, for such system, particle detection may be hampered by the weakest link, i.e. the particle detection may fail based on a single view being obstructed by the object.

Conversely, the partitioned system is more prone to the occurrence of ghost particles. The main advantage of such system is that a particle not in view by one of the cameras in a given subset may be in view from all the other cameras of another subset. In this respect, the system is more resilient to optical obstructions.

The above concepts are depicted schematically in Figure 3.5, where the situation is exemplified with three particles in the surrounding of the model. Particle A is in view of 5 cameras, particle B in view of 4, and particle C in view of 3. What regions of the domain, and which particles will be detected, depends on how the system is operated, more specifically on how many cameras are requested for the

reconstruction.

The result of a monolithic system where all cameras are required is that none of the points will be detected. The reconstructed regions for different numbers of activated cameras are plotted in Figure 3.5 in green, for the same plane as in Figure 3.4.

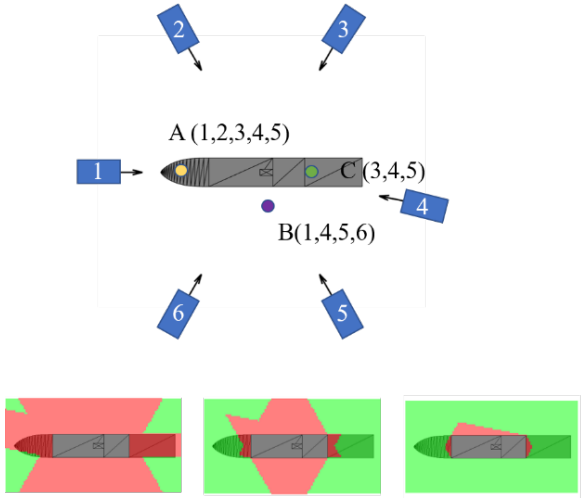

Figure 3.5.: Losses (in red) resulting from a redundant camera system depending on the mode it is operated. Bottom row: Left) Monolithic system, all 6 cameras are required for the reconstruction, Middle) Partitioned system with groups of 5, Right) Partitioned system with groups of 4.

An expression can be derived that describes $V_{loss,C}$, for a monolithic system, and it is presented below. The expression is given for a system comprising N cameras.

$$V_{\text{tot,C}} = C_1 \cup C_2 \cup \cdots \cup C_N \tag{3.4}$$

The same quantity for a system partitioned into subset of 3 cameras reads as:

$$V_{\text{tot,C}} = (C_1 \cup C_2 \cup C_3) \cap (C_1 \cup C_3 \cup C_4) \cap \cdots \cap (C_4 \cup C_5 \cup C_6) \tag{3.5}$$

The number of camera sub-systems available for reconstruction is the number of combinations of N_{min}, the minimum number of cameras required to reconstructed 3D positions, out of N, the total number of cameras available and reads as:

$$N_{sub} = \frac{N!}{N_{min}!(N - N_{min})!} \tag{3.6}$$

The losses associated with each operating mode are summarized in Figure 6, and expanded for the consideration of the cameras' elevation angles 0, 30 and 60°, (in accordance with the results shown for the illumination). It can be clearly seen that requiring fewer cameras for particle triangulation, greatly increases the number of camera sub-systems available from 1 when all 6 cameras are required, to 20 when a minimum of 3 is required. This results in a dramatic gain of approx. 60% of the DOI. It should be retained in mind, however, that reducing the number of cameras of a subset will make the system prone to generating ghost particles.

Finally, as the elevation angle is increased, the losses decrease, as expected from the analogous results from the illumination.

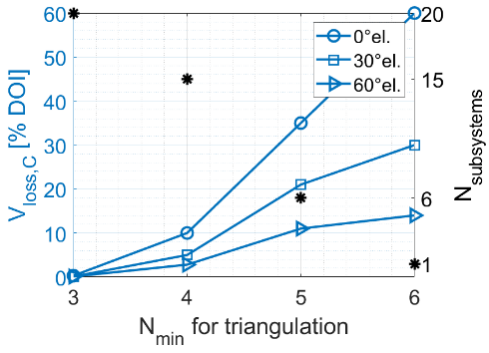

Figure 3.6.: Plot of the imaging losses and number of available camera subsystems resulting from different operating modes of the redundant camera system.

One result of Eq.3.5 is that when redundant cameras are available, and the system is operated in a partitioned mode, a larger overall measurement region can be achieved by placing the cameras such that their occluded regions intersect minimally. This corresponds to the condition whereby the cameras' placement maximizes $\beta_{i,j}$ for every subset. As a result, the system does not suffer from the conflict of V_{loss} and β described for monolithic LPT systems. Furthermore, this condition offers increased freedom in the placement of the cameras, and potential to optimize the imaging system for both minimal losses and optimal reconstruction quality. Based on Eq. 1-6, a loss parameter is defined to quantify the performance in terms of volumetric coverage, of a multi-directional system. A criterion, based on the condition that the volumetric measurement loss does not exceed 5% of the domain of interest is introduced, namely:

$$V_{loss} = DOI \cap (V_{tot,S} \cup V_{tot,C}) < 5\% DOI \tag{3.7}$$

Although arbitrary, this value suggests that multi-directional redundant camera systems should be designed to meet this criterion, when the losses due to optical obstruction are to be neglected. In Figure 3.6 the losses associated with the partitioned mode of operation of the redundant camera systems can be contained to 0.3% of the DOI, in contrast with those resulting from a single system comprising three cameras, as shown in Table 3.2. Even considering only the case of a single position (at 0 ° yaw), which will be the subject of the following sections, the redundant imaging reduces the amount of volume losses dramatically, from the initial value of 20%. This allows to satisfy the loss criterion and highlights the necessity for multi-directional imaging. The concepts given above are put into practice and illustrated with an experimental realization of a multi-directional redundant 3D LPT measurement.

3.3. EXPERIMENTS AROUND A SHIP MODEL

3.3.1. EXPERIMENTAL APPARATUS

Experiments were performed in the aero-acoustic wind tunnel AWT of the Netherlands Aerospace Center (NLR). The AWT is a closed section wind tunnel with 80 x 60 cm^2 cross section, operated at a freestream velocity of 10 m/s. AWT is configured as an open jet for the present experiment, to maximize optical access. The ship model was a simplified frigate type of 1:60 scale Van Muijden et al. (2013) mounted on a flat plate, reproducing the see surface. The model was installed upside down to simplify the placement of the cameras and illumination from the ground. The Reynolds number (Re_H = 60,000) is based on the height of the ship superstructure (H_B = 8 cm). A typical full scale Reynolds number for is in the order of 10^8. Although in general Reynolds equality is required for the wind tunnel scaling, bluff bodies with sharp angular features such as the superstructure of the ship exhibit only a weak dependence with Reynolds as long as the separated region remains in the turbulent regime. For reference, a minimum Re of 11 x 10^3 is proposed by Healey (1992), and widely accepted for ship airwake modelling. Wall et al. (2022), have also argued that increasing Re above this value the flow behavior is invariant over a wide range of Reynolds numbers. Therefore, it is argued that the effects are representative of the full scale.

Neutrally buoyant HFSB with 0.45 mm mean diameter were employed as flow tracers. An in-house developed seeding rake comprising 56 generators is installed in the settling chamber of the AWT. The pitch between generators is 15 cm in either direction. The system delivers approx. 1.4 x 10^6 tracers per second. The seeding generator unit was controlled through an in-house built fluid supply unit. At a freestream velocity of 10 m/s the seeding concentration of the undisturbed flow is estimated as approx. 1.1 tracers/cm^3, (varying from 1 to 2

tracers/cm^3 across the measurement domain) resulting in a particle per pixel value of approx. 0.01.

The particles were illuminated with a Quantel Evergreen Nd:YAG (2 x 300 mJ/pulse, λ = 532 nm). Bi-directional illumination was achieved by sending the laser beam through a beam splitter, which greatly reduces the regions of total shadow in the domain of interest. The two split beams were then expanded with f = -100 mm spherical lenses and diffused through diffuser grids to achieve a more homogeneous illumination intensity. This setup resulted in the illumination of the domain from two directions as depicted with green arrows in Figure 3.7.

IMAGING AND RECORDING

The 3D imaging system comprised seven LaVision Imager LX CCD cameras (1620 x 1220 pixels, 4.4 μm pixel pitch, 10 bits), equipped with f = 35 mm objectives, set at a numerical aperture f# = 8. The latter yielded sufficient depth of field to obtain sharp particle images along a depth of 40 cm. To achieve a compromise between the field of view (FoV) and spatial resolution, given the dimensions of the model (120 cm length to 40 cm width), the domain was analyzed in three separate sections, covered by translating the model and separated by 50 cm. This was achieved without re-arrangement of illumination and imaging systems. A schematic view of the cameras' positions and viewing directions is shown in Figure 3.7.

The largest tomographic angle in the setup is 85° and the smallest in a subsystem is 40°. The elevation of the cameras under these imaging conditions is approx. 45°. At the chosen free-stream velocity, a time separation of Δt = 350 μs yields a maximum particle image displacement of approx. 10 pixels. Measurements sequences are acquired at a rate of 7.55 Hz, with 230 recordings for each segment. Table 3.3 summarizes the measurement parameters.

Parameter	**Value**
Laser pulse separation (double-pulse) [μs]	350
Recording frequency [Hz]	7.55
Sensor size [pixels]	1620 x 1220
Image sensor pixel pitch [μm]	4.4
Magnification	0.0126
Objective focal length [mm]	35
Numerical aperture $f\#$	8
Measurement domain	0.6 x 0.5 x 0.4 m^3
Nr. of recordings	230

Table 3.3.: Volumetric measurement parameters

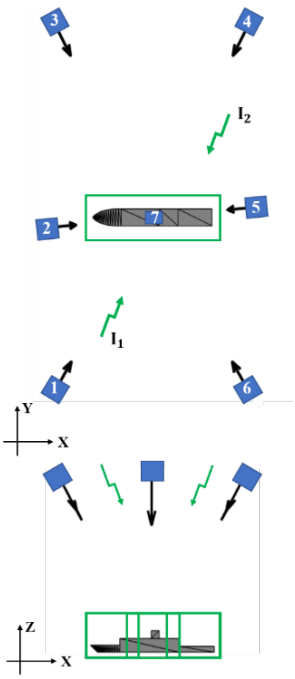

Figure 3.7.: Sketch of the 3D LPT setup (distances not to scale).

System calibration is crucial for the accurate reconstruction of particle positions. Several advancements have been recently proposed in the field of calibration from multiple cameras for large-scale experiments. One such study is that by Muller et al. (2020), where calibration was done using a freely moving calibration target. However, in the present study, to minimize the complexity of the setup, the imaging system calibration yielding the world-to-image mapping function was performed with a standard PIV calibration plate, translated along the depth, prior to model installation. The geometric calibration was followed by a correction procedure (volume self-calibration, Wieneke (2008)) reducing residual reprojection errors to a fraction of a pixel. Synchronization of illumination and image acquisition and data recording and display were achieved with a LaVision programmable timing unit (PTU-X) and controlled with DaVis 8 software.

PARTICLE RECONSTRUCTION

Data processing was done in DaVis 10, using the Shake-The-Box (STB) algorithm adapted for double-frame recordings Novara et al. (2023), in a research version of the software. Within STB, specific modifications for the processing of data ac-

quired with a system of redundant cameras are only necessary in the Iterative Particle Reconstruction part (IPR) procedure (Wieneke (2012), Jahn et al. (2021)), where the algorithm needs to be adapted to allow for sub-groups of cameras to contribute to the reconstruction. Within IPR, particles were added in 4 iterations (of the outer and inner loops of the algorithm), within an allowed triangulation error of 0.5 px. A minimum of three cameras was specified as a lower limit for particle reconstruction. The number of detected tracks (paired particles) obtained from the monolithic approach is approximately 20% that returned by the partitioned method (approx.. 15,000), as shown in Figure 3.8. The ratio of 20% for the monolithic approach is consistent with the analysis performed in section 2. For completeness, the results from some subsystems of three or four cameras are shown. Clearly, the choice of the observation direction largely impacts the volume losses and in turn the amount of detected tracks. With a minimum of only 700 tracks with the subsystem 2-5-7, due to the limited field of view of camera 7 (placed directly above the model). In general, systems of three or four cameras yield 1,000 to 3,000 tracks, which is a visibly smaller amount compared with the redundant, partitioned imaging system.

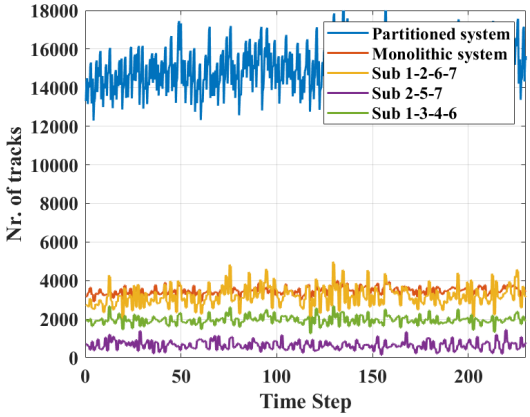

Figure 3.8.: Number of particles tracked with different approaches/camera subgroups.

VELOCITY EVALUATION

The instantaneous velocity of each particle tracer is evaluated at the midpoint of the particle pair, at scattered locations. The time-average velocity is brought into a Cartesian grid by ensemble averaging the velocity of particle tracers belonging over cubic cells of 2 x 2 x 2 cm^3 . Given the spatial concentration and the number

of recordings, each bin collects approximately 2,500 to 5,000 samples. Furthermore, the velocity vectors are spaced by 0.5 cm as a result of 75% overlap among neighboring bins. Each separate measurement domain encompasses 60 x 50 x 40 cm^3 and the velocity field is described with a grid of 158 x 131 x 105 nodes. The composite measurement covers a domain of 130 x 50 x 40 cm^3 with 260 x 151 x 80 nodes. At the edges of the DOI the concentration of detected tracers decays and with it the number of samples comprised in a single bin. The validity criterion for a velocity vector from a given bin is set to a minimum of 50 samples. Model translation resulted in small non-overlapping regions, visible as data gaps in the velocity fields presented in Section 4.1. This is due to the pyramidal shape of the FoV from each camera, unlike the assumption of parallel viewing rays taken for simplicity in the imaging analysis.

The main sources of velocity uncertainty estimation are identified as system calibration, particle triangulation and detection uncertainties, signal-to-noise (SNR) ratio of the particle images, and errors in particle matching and tracking.

Regarding the calibration and particle detection uncertainties, after performing Volume-Self-Calibration (Wieneke (2008)) on the particle images, the geometric calibration in this measurement was corrected to below 0.05 pixel accuracy. Additionally, given the relatively low ppp value of 0.01 and the tomographic aperture of most camera sub-systems exceeding 45°, the ambiguities in particle detection and triangulation are minimal with the IPR algorithm Scarano (2012), Wieneke (2012). The SNR of the pre-processed images is approx. 500, averaged across the domain, with the illumination intensity being approximately constant across the domain, spatially and temporally, and with minimal reflections due to the matte black painted model. Errors in matching and tracking are known to be higher for double-pulse measurements as compared to multi-pulse or time-resolved measurements where particles can be followed over several frames. A convergence analysis on the time-averaged results (omitted here for the sake of brevity), shows that the value of the mean velocity (for each component) converges within 2% (1%) of the free-stream value including 60 (180) measurements.

The maximum measured velocity is 11 m/s. For the minimum resolvable velocity, an estimation of the local velocity uncertainty is determined by amplitude of velocity fluctuations u' divided by the square root of amount of particles Np in a bin. The latter estimator is averaged across the measurement domain, yielding a value of approx. 0.05 m/s, which corresponds to approx. 0.5% of the maximum measured velocity. A further discussion on the variation of the velocity fluctuations across the domain, particularly over the ship-flight-deck is provided in Section 4.2.

The flow topology is illustrated displaying the time-averaged velocity field (velocity component iso-surfaces and cross sections). Furthermore, when relevant,

vorticity and Q-criterion are employed to describe the topology of vortices. The data is overlaid onto the CAD geometry of the ship model.

3.4. RESULTS

3.4.1. TIME-AVERAGED FLOW TOPOLOGY

The airwake over the ship front side exhibits flow structures characteristic of flows over delta wings (bow segment), forward facing step (FFS) in the superstructure, (Graziani et al. (2018); Largeau and Moriniere (2007), Barbosa-Saldaña and Anand (2007)), surface mounted prisms (the funnel), (Schröder et al. (2019); Sousa (2002)) and backward facing step (BFS) at the rear deck, (Chun and Sung (1998); Scarano et al. (1999); Spazzini et al. (2001); Piirto et al. (2003); Chovet et al. (2017)). Many of the mentioned studies pertain to a Reynolds number in the order of 10^3 and on a simplified 2D FFS or BFS geometry, nevertheless some topological similarities are discussed.

Figure 3.9 shows a top and side view of the combined measurements over the entire ship, where time-averaged streamwise velocity contours are plotted in two planes: immediately above the superstructure (z = 0.145 m), and along the symmetry line (y = 0). Flow separation and recirculation is observed in five regions as reported in Figure 3.9: R_1 denotes the recirculation due to the FFS imposed by the superstructure; given the sharp edge of the latter, the flow separates again when surpassing the front edge of the superstructure, resulting in R_2.

The flow separation in front of the prismatic funnel is not captured in the present experiments, likely due to the small size of its cross section and the limited spatial resolution. Instead, the separated wake past it is clearly visible as R_3. Finally, the BFS imposed by the lower flight-deck produces a relatively large, separated region R_4 that will be scrutinized further with details of the fluctuating flow field. A last region of separation is observed trailing the fight-deck due to the downstream sharp edge of the deck. For better visibility, these recirculation regions are encompassed by the zero streamwise velocity iso-surfaces in the plot.

For the flow over the FFS, compared to studies of FFS flow in a 2D configuration, the three-dimensional effects (aspect ratio of the step W/ H_f = 2.8) cause a pronounced difference. First, the finite span of the structure allows the flow to escape from the sides, which mitigates the strength of the adverse pressure gradient and delays the position of separation. The extent of the recirculation bubble at the foot is 0.8 H_f (as defined in Figure 3.1). Atop the superstructure front edge flow separates as the result of the sharp-edged structure. The reverse flow region extends downstream for a distance 2.8 H_f.

Further flow separation is encountered downstream over the funnel and above the flight-deck hangar, where the separated flow develops into 3D shear layers

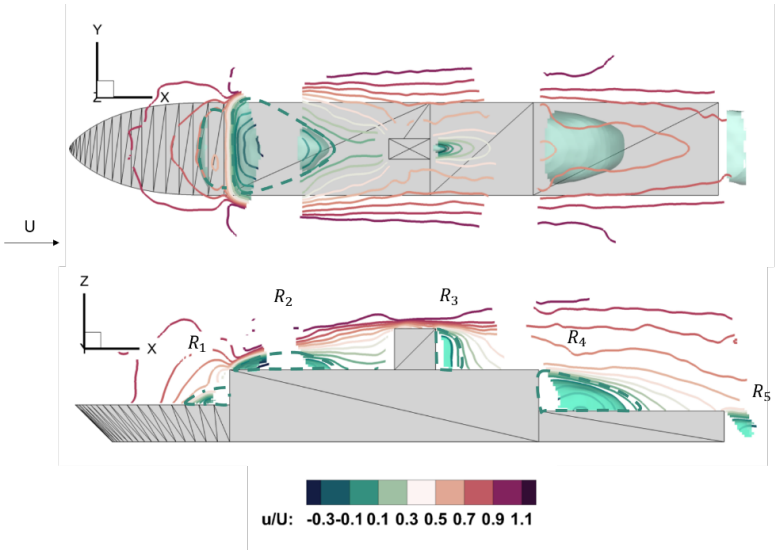

Figure 3.9.: Time-averaged streamwise velocity contours on a horizontal plane at z = 0.145 m (top) and on the symmetry plane y = 0 (bottom) along with iso-surfaces of zero streamwise velocity. Dashed lines added around the recirculation regions, partially padding the data gaps.

which enclose the regions of flow recirculation R_3 and R_4. From the velocity contours in the z-plane it can be seen that the presence of the funnel creates a velocity deficit that extend downstream over the deck region.

The flow past the hangar over the flight-deck can be compared to 2D BFS along the model plane of symmetry, however the 3D spanwise effects (AR = 2.5) are significant. The separated shear layer curves downward towards the reattachment zone and impinges on the deck wall. The distance from the vertical step wall to the impinging point is known as the reattachment length. Eaton (1980) have reported that depending upon the upstream conditions, like boundary layer state and thickness, free stream turbulence, 2D BFS flows exhibit a reattachment length varying from four to eight step heights. In the present experiment, the turbulent incoming boundary layer combined with the aspect ratio of the geometry profoundly alter the dynamics of the flow yielding a relatively short separation, observed at approximately $2.5H_B$ and with the reattachment line featuring a straight segment in the middle plane and tapered towards the side edges. This behavior is consistent with the separation length and behavior past obstacles and prisms of limited span I. Lee et al. (2004). The turbulent high-momentum flow at the sides of the separation entrains low-momentum fluid and such process justifies

the quasi-linear tapered shape of the BFS separation region. The recirculation behind the step, which features low static pressure, is enclosed by the separated free shear-layer, and this low-pressure region causes an inboard bending of the streamlines toward the mid-plane of symmetry of the deck. The recirculation zones are noted to be fairly symmetric in the time-averaged sense.

Further the streamwise vorticity distribution (Figure 3.10) indicates the salient aspects of coherent vortices developing along the ship. Two counter-rotating vortices are formed along the edges over the bow, which induce a local separation and a pronounced downwash at the symmetry plane. This vortex system is more evident by iso-surfaces of streamwise vorticity – plane in region a of Figure 10. The vorticity is normalized with the free-stream velocity and the flight-deck step length, $\omega_x^* = \omega_x / (U H_B)$. The presence of this vortex system has been previously hypothesized by Tinney and Ukeiley (2009), interpreting the surface pattern of oil flow. Based on these traces along the outer edges of the bow segment of the ship, they concluded that it corresponded to the formation and development of wing vortices, which is confirmed by this measurement.

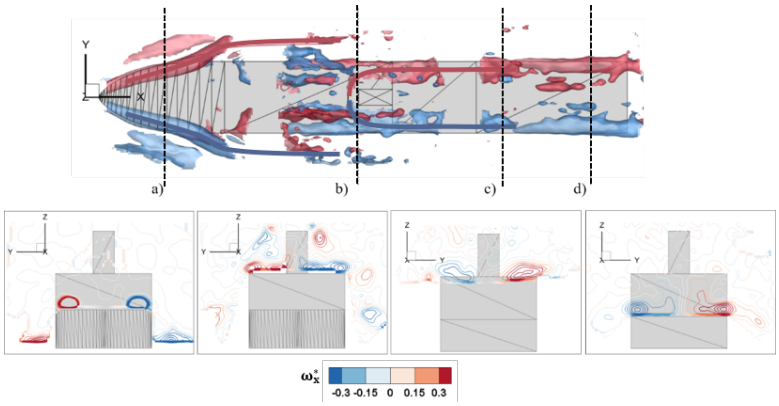

Figure 3.10.: Normalized streamwise vorticity iso-surfaces (top), and vertical planes of vorticity contours at specified stations (bottom).

Flow separation and reattachment introduce a high level of turbulent fluctuations upstream of the funnel and deck. The flow development around this structure exhibits some of the typical features reported for surface-mounted prisms, such as horse-shoe vortex, tip separation and arc-vortex at the back, (Schröder et al. (2019)), which have been schematically sketched and plotted in Figure 3.11.

The flow around the funnel results in a horseshoe vortex extending over the top of the superstructure and well downstream over the deck. Additionally, in the regions where separation over the side edges of the step is expected (section d, from Figure 3.10), the formation of edge vortices is observed, as also clarified

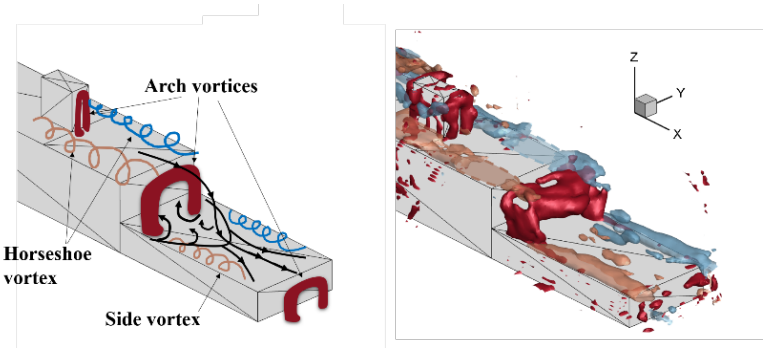

Figure 3.11.: Left) Schematic of the main flow structures expected from literature studies. Right) Iso-surfaces of w^* = -0.25 and 0.25 and Q-criterion = 0.02 s^{-2}

in Figure 3.11, due to the spanwise entrainment of fluid from below the surface of the step. These finding regarding the flow topology are in agreement with the deduced flow topology in the works of Tinney and Ukeiley (2009) and Vidales (2016).

3.4.2. UNSTEADY BEHAVIOUR ON THE FLIGHT-DECK

The time-averaged flow fields described in the previous section result from a complex instantaneous interaction between different flow structures. In order to characterize the velocity fluctuations on the deck, velocity and velocity standard deviation profiles have been extracted at the mid-hangar height z = H/2, and mid deck length x = L/2, for each component, and are plotted in Figure 3.12. The streamwise velocity component features a symmetrical distribution, with its standard deviation exhibiting a central plateau edged with two mild peaks of approximately 20% intensity, when referred to the freestream velocity.

Fluctuations in the order of 15% are observed for the vertical and lateral components, which suggests large scale unsteady behavior of the separated wake.

MODAL ANALYSIS OF THE UNSTEADY BEHAVIOUR AT THE FLIGHT-DECK

Further analysis of the wake flow topology is conducted with proper orthogonal decomposition (POD), using the method of snapshots (Sirovich (1987), Taira et al. (2017)). POD is a mathematical technique to extract the most energetic features of non-homogeneous turbulent flows. The spatial modes are ranked based on their kinetic energy (KE) levels. The first three modes are the most energetic, collecting approximately 30% of the total energy (Figure 3.13). The energy distri-

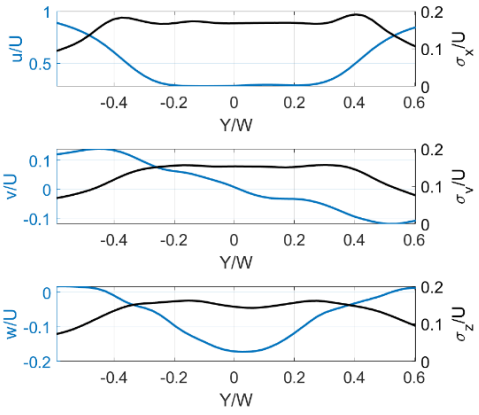

Figure 3.12.: Component-wise velocities and standard error on a horizontal plane in the mid-deck : z = $H_B/2$, x = L/2.

bution rapidly flattens at the 4^{th} mode, with the first 15 modes comprising 50% of the total energy. The latter indicates the chaotic nature of the turbulent fluctuations in the separated region, with a broad range of scales contributing to the dynamics of the flow. Here a short analysis is given for the most energetic modes.

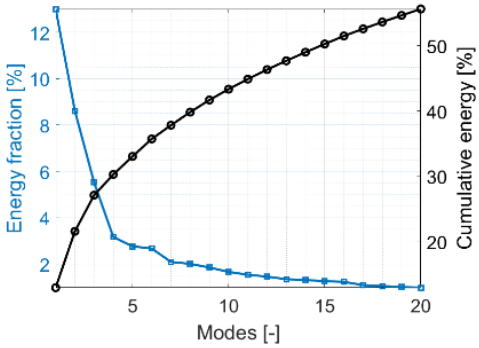

Figure 3.13.: Energy distribution in the first 20 POD modes.

The spatial organization of the first three modes is shown in Figure 3.14, by means of streamwise velocity contours selected at the mid-height plane of the flight deck. The first two modes have a similar spatial structure, exhibiting alternating streamwise velocity deficit on the port and starboard sides of the flight deck. The two modes show anti-symmetry along the mid-plane y=0, with one

mode more focused on the port side, and the other on the starboard side. If considered as a pair, they can capture lateral oscillations of the separated wake flow. Their mirror symmetry suggests that the modes are needed in combination to represent a flow behavior which is inherently symmetric (the geometry is symmetric around the mid-plane and the measurement is done at headwind condition), however their unequal energy distribution suggests that the flow might be biased towards one side. The two effects combined could be interpreted as evidence that the flow is more aligned with one mode during certain periods, and switch during others, while maintaining an overall symmetry in the time-averaged sense. This observation is in line with previous studies on ship airwakes, that attribute the most energetic flow features to similarly fluctuating, organized flow motion that is bi-stable over the flight-deck.

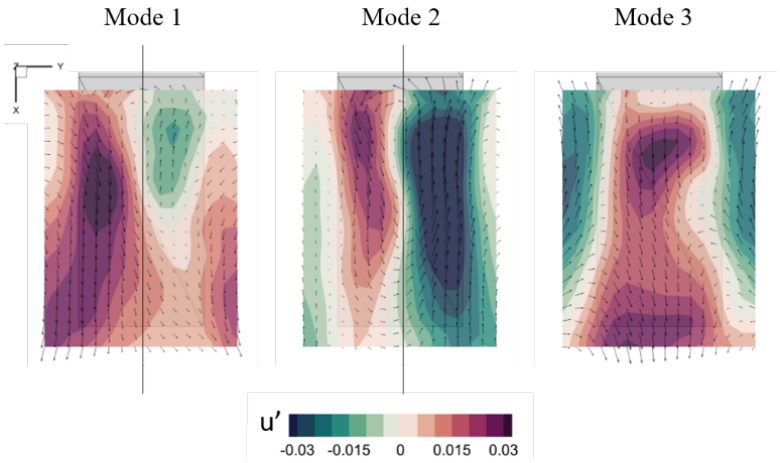

Figure 3.14.: Streamwise velocity component of the first three POD modes, on the mid-plane of the flight deck, z = HB/2.

This is reported in the works of Herry et al. (2011),Vidales (2016), Mallat and Pastur (2023), Zhu et al. (2024), among others. In order to investigate the possibility of flow bi-stability, the time coefficients of the first two modes were examined, as plotted in Figure 3.15.

Bi-stability in this context means that the recirculation region may enter a relatively stable state at either port and starboard side of the flight deck and only switch position after a long time. In order to define a sufficiently long time period that would suggest stability, a transit time scale is taken to be that taken by a fluid particle to travel across the complete model. In the present experiment, such time is approximately 120 ms. During the observation time of 30 seconds at least two cycles of fluctuations are captured, each lasting approximately 15 sec-

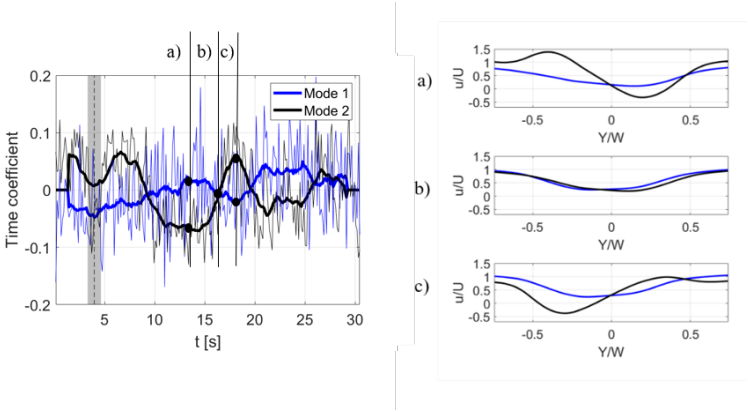

Figure 3.15.: Raw and filtered (in bold) time coefficients of Mode 1 and 2.

onds. The latter is approximately two orders of magnitude longer than the transit time, supporting the hypothesis of bi-stability of the wake.

Finally, the third mode is associated with a streamwise elongation and contraction of the wake: when the wake elongates in the streamwise direction, it contracts in the lateral direction, thus becoming narrower. Such mode structure represents a dynamic behavior typically reported in 2D BFS studies, as shear layer flapping (Driver et al. (1983)).

The present modal analysis is performed on 3D data. However, attention is placed here on the comparison between 3D data decomposition and 2D. Most of the literature has focused onto the vertical plane of symmetry of the deck y = 0. Figure 3.16 illustrates the velocity distribution for mode 1 as obtained from the 2D (left) and 3D (right) analysis. Here some marked differences are observed in terms of flow topology. Despite these differences, the 2D results compare favorably with the planar PIV experiment by Seth et al. (2021), and what was found by Tinney et al. (2020) in their numerical study.

The first and most energetic mode of the 2D POD analysis shows a streamwise velocity deficit around the reattachment region, and a velocity increase in the first half of the deck, on top of the hangar. This mode describes a dynamic behavior whereby the recirculation region elongates in the streamwise direction and contracts vertically, similar to what is observed in Mode 3 of the 3D decomposition. Additionally from the energy distribution plotted on the right of Figure 3.16, it can be seen that in the 2D case the energy captured in the first mode is approx. 30%, which corresponds to the sum of the first three modes of the 3D decomposition. Therefore, it can be concluded that the 2D POD analysis can mislead the interpretation of the large-scale flow dynamics, in that the presence

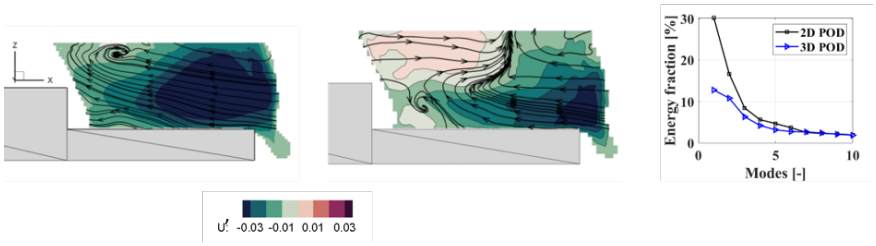

Figure 3.16.: Streamlines and contour plots of the streamwise velocity component for: Mode 1 of 2D POD (left); Mode 3 of 3D POD (middle); Plot of the energy distribution in the two decompositions.

of the wake's lateral fluctuation (which are the dominant dynamic in 3D) is projected across the measurement plane, but not captured in the lateral motions. The 3D analysis shows that in fact the wake dynamics are characterized by a lateral flapping of the wake and the change in size of the recirculation bubble behind the superstructure. This is obscured in the 2D POD analysis, highlighting the need for large-scale volumetric flow measurements.

3.5. CONCLUSION

A large-scale volumetric velocimetry measurement with helium-filled soap bubbles has been performed at the AWT of the NLR with a multi-directional, redundant camera system and multiple illumination directions, to measure the flow field around a ship model at 10 m/s free-stream velocity. The measurement volume attains approximately 0.5 m^3 and it is extensively covered using seven cameras and two illumination directions. The foundational elements of multi-directional redundant illumination and imaging are discussed, with the approaches needed in large-scale 3D LPT experiments that extend the measurement domain and enable unsteady aerodynamic analysis. An optical loss parameter has been defined as a guideline for volumetric measurements that feature rotations of the model, most specific in the field of wind engineering. Overall, the results showed that a redundant system of cameras, operated in a partitioned mode significantly decreases volume coverage losses in the measurement domain and therefore allows the study of the global unsteady behavior in multi-directional 3D-LPT systems. The technique is demonstrated on the relevant problem of ship-wind interaction where velocity measurement were obtained around the ship. Multiple zones with shear layers and recirculation regions on both the superstructure and flight-deck. 3D POD was used to analyze the large-scale unsteady motions on the flight-deck, where the first three modes

identify lateral flapping of the wake and the change in size of the recirculation bubble behind the superstructure. The primary modes occur close to the flight deck, at a scale in the order of the deck length, and support previous finding of recirculation region bi-stability.

4

ASYMMETRIC TIME-SEQUENCES FOR MULTIPLE-EXPOSURE 3D PTV

1

[1] Parts of this chapter have been published in: Scarano, F., Hysa, I., Grille Guerra, A., Tuinstra, M., & Sciacchitano, A. (2025). Asymmetric time sequence for multiple-exposure 3D PTV. *Experiments in Fluids*, *66*(4), 74

4.1. INTRODUCTION

State-of-the-art three-dimensional particle tracking is based on 3D particle detection (IPR, Wieneke (2012)). Particle pairing, initially based on predictor-corrector techniques (Malik and Dracos (1993)) has been recently revised profoundly and coupled within the image processing analysis, resulting in a powerful and computationally efficient method (Shake the Box, Schanz et al. (2016)). Most of the current research focuses on single-pulse, double- or multiple-frame recordings, which requires high-speed illumination and imaging for the latter. Techniques based on multiple-exposure (ME) recordings have been popular at the time of photographic PIV, but rapidly declined with the advent of kilohertz rate illumination and imaging systems. However, ME recording may become relevant again, considering the recent developments towards multi-camera redundant systems (Hysa et al. (2023)), where a multitude of imagers are used in double-frame recording mode. Furthermore, time-resolved analysis of particle motion requires increasingly high imaging rates when aerodynamic flows at velocity higher than 10 m/s are to be investigated. In those situations, it is common to revert to double-frame recording, to detriment of the velocity dynamic range and measurement reliability in general. ME imaging can potentially solve the above trade-off, provided that the information lost in the single-frame recording can be recovered. The analysis of ME recordings has been and still remains a challenging problem, due to the loss of time-tag of the detected particles. For instance, Utami and Ueno (1984) performed a manual analysis of four-pulse recordings (Figure 4.1). Yet, the direction of motion needed to be determined by additional criteria. Early works dealt with planar illumination, mostly, and the problem of truncated traces by out-of-plane motion was approached by using a dot-streak-dot encoding of the particle image (Agüí and Jimenez (1987)). A solution to the problem of directional ambiguity was proposed by Grant and Liu (1990), with the pulse tagging technique, whereby the preceding and following pulses were differing in their intensity. Even though the research shifted its focus towards algorithms for the analysis of single-frame single exposure recordings, ME or streaks analysis maintain its research scope (Qureshi and Tien (2022), among others). A specific development of the Shake-the-Box technique for double-exposure recordings has been proposed, whereby a total of four exposures are collected on a double-frame recording. The directional ambiguity is approached making use of either a tentative search or making use of a particle-space correlation to produce a statistical velocity predictor (Novara et al. (2019)).

For a multiply exposed recording, the two main problems are the time-tag (i.e. establishing the correspondence of each dot to a time instant) and the trajectory-tag (i.e. associating multiple dots with the same physical tracer and defining its trajectory). The latter is also known for single-exposure systems as the pairing

problem. When the density of particle images in the recording is increased, the distance between particle images becomes comparable to the distance travelled between pulses and the probability of false pairing grows exponentially, as discussed in the early works of Maas et al. (1993). Finally for 3D measurements, for a given concentration of the tracers, recording multiple positions of the particle tracers on a single image increases the image density and the probability of ghost particles.

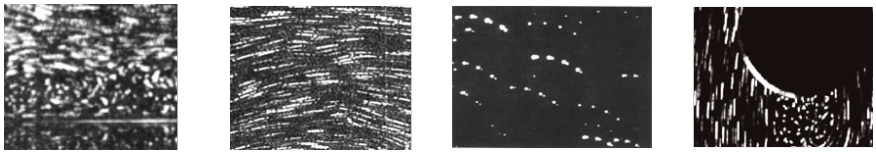

Figure 4.1.: Examples of ME recordings for PTV analysis of fluid flows. From left to right: four-pulse(Utami and Ueno (1984))); pulse-streak-pulse(Agüí and Jimenez (1987)); pulse-tagging(Grant and Liu (1990)); streak velocimetry(Qureshi and Tien (2022)).

The present study examines the problem of time-tag and trajectory-tag assignment for multiply exposed recordings. The principle to resolve the directional ambiguity is that of sequence tagging, i.e. a specific pulse sequence is utilized, where the time intervals are irregular and do not exhibit time-symmetry. The result is an irregular sequence of dots, here called a trace, to be compared to the imposed sequence of illumination. The principle has been introduced in Hysa et al. (2022), who examined the impact of the sequence structure on the trace detectability. In the present study, a kinematic similarity criterion is introduced, which at the same time allows recognizing the trace as a sequence of dots along the particle trajectory (trajectory-tag) and resolves the directional ambiguity of said dots (time-tag). Furthermore, the kinematic similarity criterion is combined with an additional constraint on the particle acceleration (trace regularity) whereby departure from similarity is penalized along with the L-2 norm of the acceleration along the trace. The two criteria yield a composite signal with the associated signal-to-noise ratio that is the backbone of the current method. The working principle is first illustrated with a numerical example and then demonstrated, using an experimental database of 3D measurements around a wall-mounted cube immersed in a turbulent boundary layer at Re = 80,000 (Hendriksen et al. (2024)).

4.2. TRACE DETECTION

When a tracer particle is illuminated while moving along its trajectory, it produces a pattern that depends upon its velocity and acceleration, the illumination sequence and the viewing direction. Once particle images are reconstructed in 3D space, the dependance upon the viewing direction is eliminated. Continuous illumination yields streaks, while regular pulses return mostly dotted straight or curved lines. Variations of the above have been illustrated in Figure 4.1, where most often, the sequence is obtained by equally spaced light pulses or a combination of dots and streaks. For a chosen time separation, the larger the number of pulses N, the higher is the measurement precision, as the velocity dynamic range is found to scale with $N^{3/2}$(K. Lynch and Scarano (2013)). A non-regular sequence has the potential to disambiguate the direction of motion. The principle, though intuitive, is schematically represented in Figure 4.2. A chosen sequence of illumination pulses (temporal template) with varying time separation translates into a sequence of dots (marks) in the image (trace) spaced by corresponding travelled paths. Let us define the particle trajectory Γ Figure 4.2-left with the sequence of N time instants corresponding to the light pulses $\tau = t_1, t_2, \ldots, t_N$, with $t_1 = 0$ and $t_N = T$. We indicate the normalized vector of time instants as $\tau^* = \tau$ / T, such that $\tau^* \in [0, 1]$.

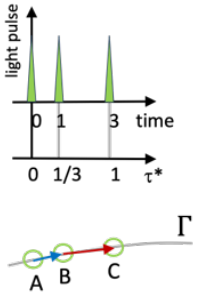

Permutation	Paths	$\varepsilon_{\sigma\tau}$	ε_{α}	$\Pi\varepsilon$
A – B – C		0.0	0.0	0.0
A – C – B		1.33	4.0	5.33
B – A – C		0.67	3.5	2.33
B – C – A		2.0	3.5	7.0
C – A – B		2.0	2.5	5.0
C – B – A		2.0	1.5	3.0

Figure 4.2.: Left: Three-pulse sequence temporal template and the corresponding trace (bottom). Right: time-tag permutation list and corresponding paths (blue for the first displacement and red for the second one). Output of CKS, CKR and composite detection criteria.

The particle position at such time instants is given as the vector of marks $X_p = x_1, x_2, \ldots, x_N$. Correspondingly, we indicate the travelled distance as $\sigma = s_1, s_2, \ldots, s_N$ with $s_1 = 0$. The normalized abscissa is $\sigma^* = \sigma / s_N$, resulting into $\sigma^* \in [0, 1]$. In the hypothesis that the variations of the particle tracer tangential velocity can be neglected along the trace, τ^* and σ^* should obey the criterion of kinematic similarity (CKS), i.e.:

$$\epsilon_{\sigma\tau} = \sum_{i=1}^{N} [(\sigma_i^* - \tau_i^*)^2]^{1/2} \tag{4.1}$$

Such criterion needs to be evaluated for all possible choices of the time-tag, which corresponds to the N! permutation of their index. The situation is illustrated in Figure 4.2-right, where the order of the time-tags (A-B-C) is varied according to the permutations, each corresponding to a possible path. The latter is inspected by Eq. 4.1, yielding the residual $\epsilon_{\sigma\tau}$. For this given set of N particle marks, a trace of rank N (ξ_N) can be detected based on the criterion that selects the case (viz. permutation) with minimum disparity between the temporal template and the normalized path:

$$\min_{\xi} \{\epsilon_{\sigma\tau}\}_K \tag{4.2}$$

Where K is the number of possible permutations from the N considered particle images (K = N !). The evaluation of such criterion is illustrated in the first column on the right of Figure 4.2 for the case N = 3. An additional criterion, frequently adopted in PTV analysis is based on the piecewise estimation of the acceleration of the particle. The criterion of kinematic regularity (CKR) reads as:

$$\min_{\xi} \{\epsilon_{\alpha}\}_K \tag{4.3}$$

Where ϵ_α is defined as the sum of the standard deviation from each component of the velocity vector along the piecewise trajectory. An example for this criterion is also given in Figure 4.2 for the simplified case of a trajectory with negligible Lagrangian acceleration. The above criteria are imposed simultaneously and combined through their product $\Pi\epsilon = \epsilon_{\sigma\tau}$ x ϵ_α; the latter yields a composite signal defined in the space of particle time-tag permutations. Correspondingly, a composite detection criterion (CDC) is defined as follows:

$$\min_{\xi} \{\Pi\epsilon\} \tag{4.4}$$

The last column in Figure 4.2 shows this quantity and indicates how the combination of these two criteria improves the trace detectability, identifying the correct permutation of time-tag as that exhibiting the furthest distance between the absolute minimum and the second lowest value. Based on the latter quantities a signal-to-noise ratio can be introduced in the space of the permutation index as the ratio between absolute minimum and the second lowest value of the composite detection criterion. In this example, the second lowest value is 0.67, 1.5 and 2.33 for $\epsilon_{\sigma\tau}$, ϵ_α and $\Pi\epsilon$ respectively. The value corresponding to the correct

sequence in this example is zero, given the ideal conditions considered (no noise and zero acceleration). In realistic condition, an estimate of such minimum is typically o(0.1), when considering the combined effect of measurement and trajectory modelling uncertainties altogether not exceeding 10%. When the two criteria are multiplied, the composite criterion is expected to yield a minimum in the order of 10^{-2}. Instead, the spurious permutations yield values remaining in the order 1 or larger. As a result, the signal-to-noise ratio of the composite criterion is expected in the order of 100 or above, which indicates a favorable condition in terms of trace detectability.

4.2.1. NUMERICAL EXAMPLE

With the purpose to illustrate the principle of the algorithm a simplified numerical example is presented here, where a set of particle images belongs from one complete trace and two additional marks spurious to the trace. Figure 4.3 illustrates two conditions: on the left, the spurious marks lie at distance from the trace, whereas on the right, they appear along the trace and may be confused with it.

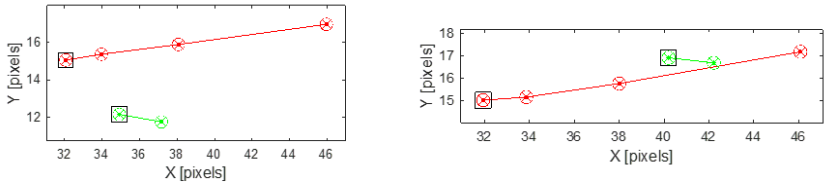

Figure 4.3.: A set of 6 candidate particle samples, of which 4 pertain to a trace (red labels) and 2 are from an incomplete, truncated, trace. Left: distance between spurious particle images and trace is larger than particle displacement. Right: distance is smaller than displacement.

The detection criteria are numerically evaluated and the result is shown in Figure 4. The top row displays the evaluation of the red trace on the left of Figure 4.3: 1) the residual of particle position as expected from the kinematic similarity; 2) the residual from the piecewise acceleration; 3) the composite criterion.

In this case, the four marks composing the trace are correctly selected, given that the spurious marks are sufficiently apart. The criteria are evaluated for all 24 permutations (4!) of such four marks. It can be observed that the minimum for CKS is in the order of 10^{-2} and that of CKR in the order of 10^{-1}. The composite criterion yields therefore a minimum in the order of 10^{-3}, which compared to the second lowest value of unit order of magnitude yields a signal-to-noise ratio SNR in the range of 10^{3}. The situation on the right of Figure 3 features the spurious

marks (green) in close proximity of the main trace (in red). In this case, the four marks selected for the analysis contain one spurious mark and the results are shown in the bottom row of Figure 4.4. Both CKS and CKR exhibit a minimum in the unit order of magnitude. As a consequence, also the composite criterion returns a minimum of unit order, not significantly separated from the second lowest value. The low level of the SNR ($SNR_{CDC} < 2$) allows to conclude that the selected set of marks does not belong to the same particle and the trace is not accepted as a valid measurement.

In the latter example, the importance of preselecting the sets of marks that candidate to form a trace is emphasized. From combinatorial analysis, the number of possible combinations of M marks by groups of N is given by:

$$C(M,N) = \frac{M!}{(M-N)!N!} \tag{4.5}$$

It should be retained in mind that the value of C increases very rapidly with M. Thus, any algorithm using this approach requires a careful choice of the minimum neighborhood for trace evaluation. In absence of additional criteria that limit the selection of the samples, it is therefore necessary that the number of marks considered to identify a trace are taken in relatively small subgroups by preselection (e.g. M < 10 and N < 5). For every candidate trace, the detectability criteria need to be evaluated for every permutation of the time-tag, with a total of K = N ! possibilities as illustrated in Figure 4.2, where N = 3 and K = 6. Combining both requirements returns a total number of evaluations, P, that scales as:

$$P = CM! = \frac{M!N!}{(M-N)!N!} = \frac{M!}{(M-N)!} \tag{4.6}$$

Due to the computational burden associated with the proposed method, approaches that reduce the complexity of both the candidate trace selection and time-tag permutation have been explored and their effect on the computation time required are discussed in section 6.

4.3. NUMERICAL ALGORITHM

The above principles are implemented in a numerical algorithm, schematically depicted in Figure 4.5. The process considers as input the recording of multiply exposed images of particles (box a) such as illustrated in Figure 4.7-right. Particle image triangulation (e.g. IPR, box b) yields 3D particle positions, however at unknown time instants (box c), of which an example is illustrated in Figure 4.8. The algorithm interrogates particle exposures selecting them one by one (box d). A search region is chosen around the exposure (box e), based either on the maximum expected velocity or a local estimate of the velocity, when available (Figure

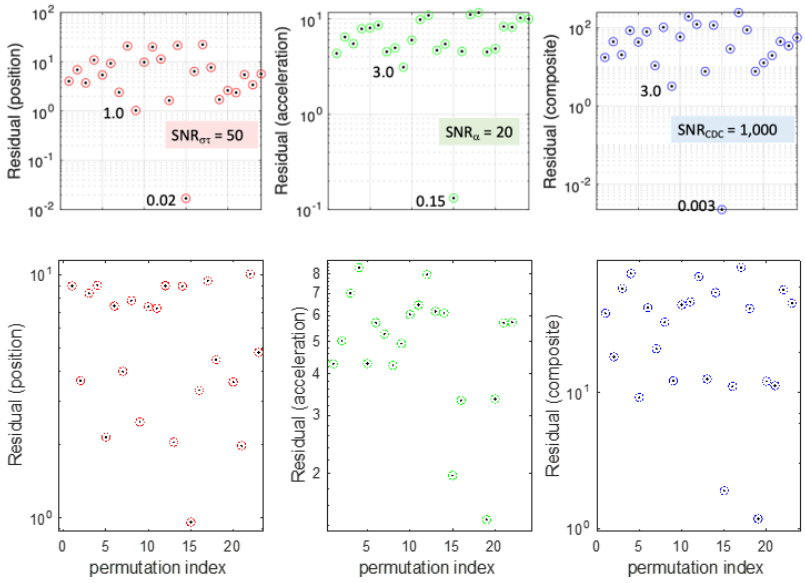

Figure 4.4.: Values of the position residual (left, criterion of kinematic similarity), acceleration residual (middle, criterion of kinematic regularity) and their product (right) as a function of particle permutation within a set. Top row corresponds to Figure 2-left, where all selected marks belong to a physical trace. Values of first and second minimum are indicated, that lead to the SNR. The bottom row corresponds to Figure 2-right, where a spurious mark is included in the quartet, as spurious marks occur in vicinity of the trace.

4.9-right), and the total time elapsed between the first and the last pulse. The minimum search diameter d_s must include the entire trace, which turns into the condition that $d_s >= VT$. In this case, when marks at the edge of trace are selected, the search region does not include the whole trace and the search fails. When a mark in the middle of the trace is considered, the search region includes the whole trace, which may be detected if it obeys the composite detection criterion. This is schematically illustrated in Figure 4.9-right. Assuming that M marks fall within the search region (box f) around the selected mark, the combinations with N-1 candidate marks is considered (each group of N marks includes the selected mark). All combinations of M-1 marks by groups of N-1 are considered (box g).

For each combination, all possible time-tag permutations are considered (box h, see also Figure 4.2-right), over which the CDC from Eq. 4.4 is applied (box i).

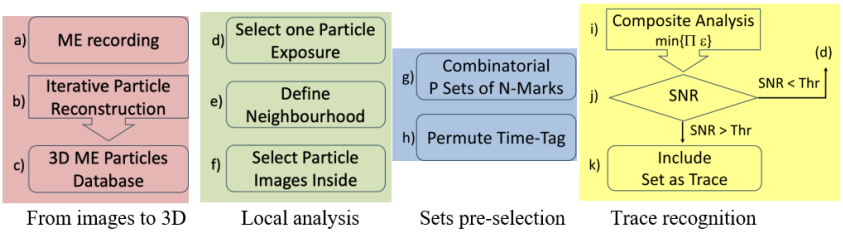

Figure 4.5.: Flow chart describing the main operations of the trace algorithm. Main blocks highlighted in the lower row.

The value of the SNR (such as in Figure 4.4) with respect to a chosen threshold value (box j) determines accepting the set as a trace (box k) or discarding it and move back (to box d). The process terminates when all particle exposures have been considered or assigned.

4.4. EXPERIMENTAL DATABASE

Experiments are conducted in the W-tunnel, a low-speed open jet facility at the aerodynamics laboratories of the Aerospace Engineering Department of TU Delft. A cube of side-length 12 cm is installed on a flat plate immersed in a stream at 10 m/s. A turbulent boundary layer develops on the plate with approximately 2 cm thickness. The cube height-based Reynolds number is Re = 80,000. The flow is seeded with helium filled soap bubbles (HFSB, neutrally buoyant, 300 μm median diameter) released by a 200-generator seeding rake integrated in the wind tunnel. The tracers' concentration is approximately 1 bubble/cm^3. The layout of illumination and imaging systems is shown in Figure 4.6: two LED-Flashlight 300 arrays from LaVision produce pulsed illumination at a rate of 3 kHz. Seven high speed CMOS cameras (Photron FastCam SA-1, 1 Mpx, 5,400 fps, 12 bits) capture the light scattered by the HFSB tracers. The 7 cameras are distributed with their view such to cover the entire object and the flow field around it, to study accurate object position registration (Hendriksen et al. (2024)) and its integration within the 3D particle tracking measurement (Wieneke and Rockstroh (2024)). In the present study, a thin section of data is considered for sake of conciseness. The data domain encompasses the (X,Y,Z) range ([–15, 20], [–2,2], [–12, 12]) cm^3 respectively. Although the measurements are conducted at a constant rate of 3kHz, irregular time separation is simulated by skipping frames in the analysis. Ground-truth data is obtained making use of the Lagrangian Particle Tracking Shake-the-Box algorithm (available in the LaVision DaVis 10 software) for the full time-resolved sequence.

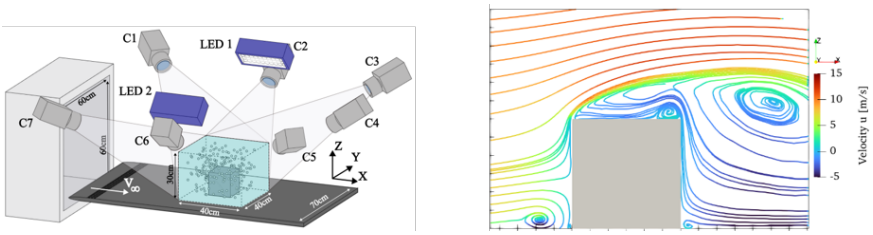

Figure 4.6.: Left: experimental arrangement and layout of the 3D particle tracking system. Right: time average, velocity color-coded, streamlines pattern in the median plane. (tick marks spaced by 2 cm).

4

By recording particle images during ME, the imaged density of particle images increases significantly. This aspect poses limitations to the maximum spatial concentration of the tracers and is discussed in the remainder. Figure 4.7 illustrates the above by comparing particle image recordings in the regimes of single (left) and four (right) exposures in sequence of pulses at τ = 0, 0.33, 1.0, 2.0 ms. The latter is obtained as the sum of intensity from the single exposure images. In the present work, the analysis is performed simulating the ME recordings and analyzing directly the reconstructed 3D position of particles. Figure 4.8 presents the 3D particle tracers positions for the case of double- and ME with uniform time separation, which is chosen to illustrate the problem of directional ambiguity arising from double exposure or ME with regular time intervals.

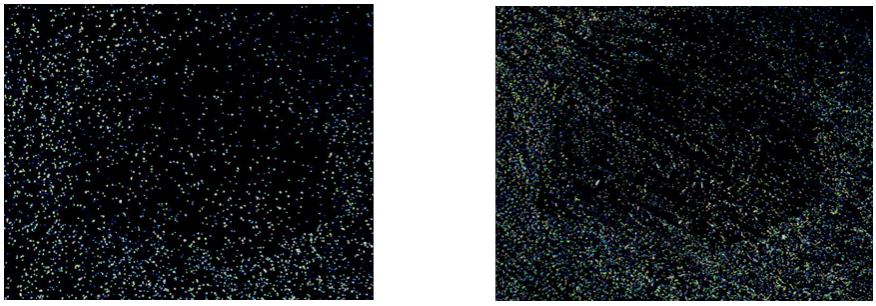

Figure 4.7.: Images of HFSB tracers from a single (left) and triple exposure recorded from one of the seven cameras. Exposures at τ = 0, 0.33, 1 ms.

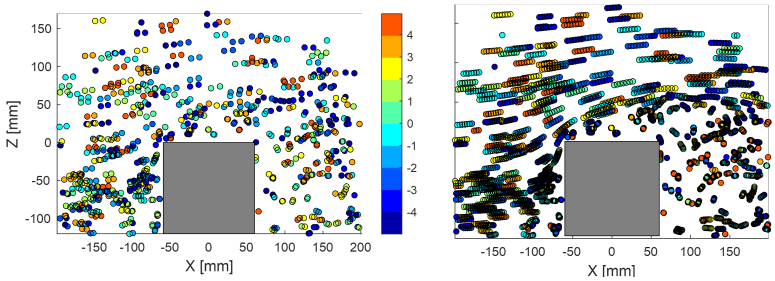

Figure 4.8.: 3D particles positions from the experimental database. Color coded depth position (in mm). Left two time instants separated with 1 ms. Right: six time instants with 0.33 ms uniform time separation.

4.5. RESULTS

In Figure 4.9 the example of a four-pulse single-frame recording is shown, according to the time instants sequence τ = 0, 0.33, 1.0, 2.0 ms. An enlarged view (Figure 4.9-right) of a region of the flow allows to appreciate the particle positions and their arrangement into traces that resemble the template imposed by the pulse sequence. The illustration shows the example of a few particles taken for the neighborhood analysis. Clearly a spherical search region conservatively admits a larger number of particles in the set for the analysis. The minimum radius can be put to half of the expected travelled distance. As a result, only when the particle sample in the middle of the trace is interrogated the trace can be fully comprised and detected (green shaded circle).

Instead, when particle samples at the edge of the trace are considered, the search will fail (red shaded circle). It can be easily seen that a-priori knowledge of the local velocity significantly reduces the search volume and the corresponding number of particle samples included in the analysis (green shaded rectangle).

An illustration of the detection process is given in Figure 4.10, where particles are displayed along the velocity vector (top-left), as obtained from the time-resolved analysis of STB. The velocity vector information, however, is not used in the detection process here. When the particle samples at the edge of the trace are considered, the search region does not include the entire trace and most detections fail (top-right). For samples inside the trace, depending on the local velocity, some sets return a correct trace or a spurious one (bottom-left). Finally, the particle samples close to the trace mid-point mostly include the full set of samples comprised in the trace and return a correct measurement (bottom-right).

When the number of pulses N is increased, the probability of erroneously detection further decreases as a result of the increased uniqueness of the sequence.

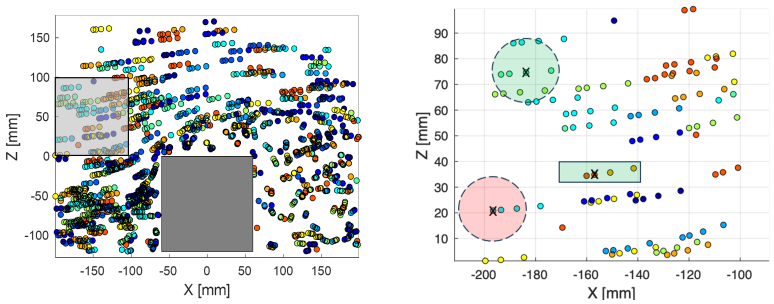

Figure 4.9.: Particles positions from the experimental database. Color coded depth position (in mm). Left: 4-exposure recording with irregular (increasing) time separation. Right: zoomed view from the shaded square in the left picture. Isotropic (circles) and adapted (rectangle) neighborhoods are shown. The green color indicates that all exposures from the trace are captured. The red color indicates incomplete set of exposures.

This aspect can be regarded as the analogous of increasing the number of particle tracers in the correlation window for PIV analysis, which is known to increase the signal-to-noise ratio of correlation. However, adding more pulses to the sequence has two important shortcomings: 1) the overall number of particle images in the recording increases and the probability of ghost particles with it; 2) adding pulses and increasing the total time of the sequence increases exponentially the computational burden associated with a large search region for the trace. The number of pulses is varied from 3 to 6 adopting a simple rule for the time separation, which increases linearly between pulses. This is realized by skipping frames from the time-resolved sequence. The case with N = 3 considers frames 0, 1 and 3. Furthermore for N = 4, frames 0, 1, 3 and 6 are considered. The longest sequence (N = 6) has been taken with a different rule for the time separation, which avoids the excessive length of the trace and at the same time gives an indication of the effect of N maintaining the same travelled path as for the case N = 5.

The corresponding pulse time and their separation are given in the first rows of Table 4.1. The original single-exposure recordings feature approximately a density of particle images of 0.02 particles-per-pixel (ppp). Therefore, the density of particle images for the ME recordings is obtained multiplying the single-exposure value by the number of exposures N. The detection criterion (box j in Figure 4.5) has been set conservatively at SNR > 100. Furthermore, varying this threshold in the range 30 to 300 has shown not to bring considerable differences

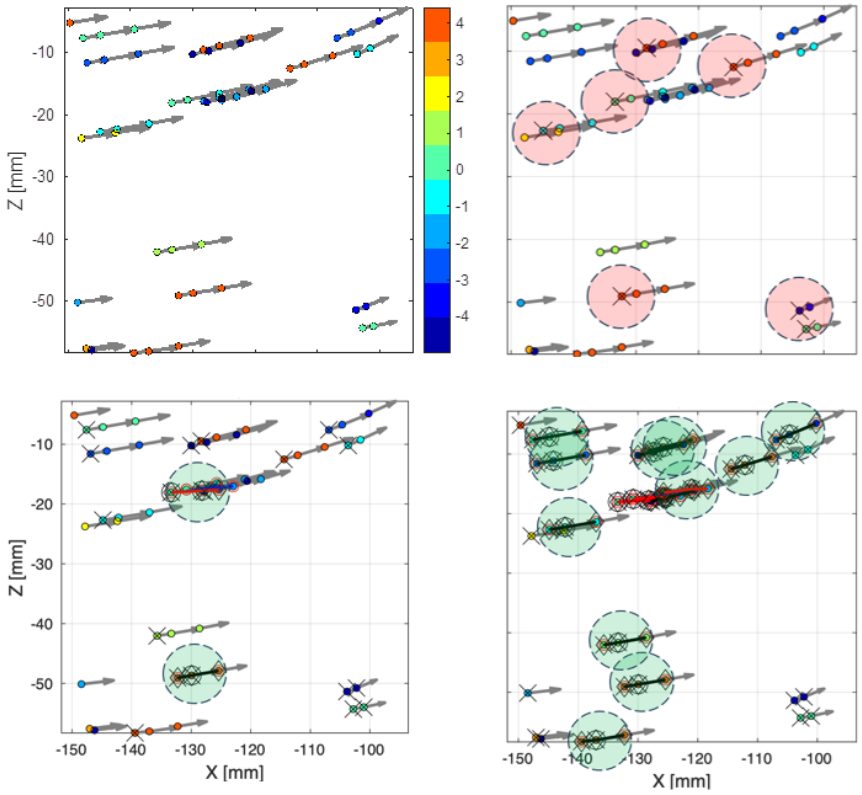

Figure 4.10.: Particle selection and trace detection in a sample region. Top-left: particles and velocity vectors from the STB analysis. Top-right: selected particles (denoted by a black cross) that do not lead to a trace because their neighborhood does not include enough samples. Bottom-left: when a particle's neighborhood contains sufficient samples, the set is subject to the composite detection criterion. Two traces are detected (around the large-circled particle), of which one is erroneous (in red). Bottom-right: the process advances for all the particles. Most errors occur in regions of nearly overlapping traces.

in the results.

The number of detected particles increases linearly with N, but the number of STB traces remains approximately constant. The same occurs for the number of detected traces. The relative detection rate is defined as the number of detected traces compared to the traces obtained with time-resolved single frame analysis

performed with the STB algorithm.

The results indicate that for the minimum trace, composed of three samples, a relatively high rate of detection is obtained (81 %), with the number of spurious detections amounting to 5.6 %. Increasing the number of pulses to 4 reduces the detection rate. However, the additional pulse yields a significant benefit in terms of reliability, with the error rate dropping below 1%. Further increases in the exposures involve more computations. Yet, the detection rate declines further, to a minimum in the range explored here, of 60% for N = 6, and a negligible error rate (0.1%). The latter effect is ascribed to the hypotheses of constant velocity, at the basis of the detection criterion. Dynamic thresholding and/or multi-pass interrogation are expected to possibly solve for this effect. Their implementation and validity, however, go beyond the scope of this study and are not included here, for conciseness.

N	**3**	**4**	**5**	**6**
Frame Index	0-1-3	0-1-3-6	0-1-3-6-10	0-1-3-6-7-10
Time [ms]	0-0.33-1.0	0-0.33-1.0-2.0	0-0.33-1.0-2.0-3.3	0-0.33-1.0-2.0-2.33-3.3
ppp*	0.06	0.08	0.1	0.12
N_p**	4147	5233	6814	8176
N_{tracks} **(TR-STB)**	1370	1358	1363	1362
N_{tracks} **(ME-PTV)**	1144	926	861	826
Detection rate	81%	68%	63%	60%
Erroneous***	62	27	2	1
Error rate	5.6%	2.9%	0.3%	0.1%

Table 4.1.: Settings of ME recording and summary of results from the experimental database.

* Based on the estimated ppp from single exposure ** Number of detected particle exposures, based on TR-STB *** Criterion for erroneous trace Err_U>0.3V_∞

4.6. ALGORITHM ACCELERATORS

One of the challenges of the proposed methodology is the computational burden associated with the combinatorial nature of it. The requirements quickly increase when considering more exposures due to the associated larger neighborhood search radius, the number of trace candidates (Eq. 4.5) and time-tag permutations. A powerful way of relaxing the computational requirements is the use of a velocity predictor to adapt the search region around a particle, as sketched in Figure 4.9-right by employing a rectangular shape instead of an isotropic search radius. The use of a predictor could come from an iterative implementation of the method, or within a spatial dilation of the measured domain. Both methods are subject to further research.

4.6.1. LINEAR-FIT PRE-SELECTOR

Besides the use of a predictor, two different strategies have been explored to reduce the cost of the candidate trace selection (box g in Figure 4.5) and time-tag permutation (box h) respectively. The first approach consists of preselecting a particle trace based on their straight alignment, evaluated with a least squares linear fit (linear fit pre-selector). Assuming that M marks fall within the search region around the selected mark, the combinations with N-1 candidate marks are considered (each group of N marks includes the selected mark). The set with the lowest residual is considered as candidate trace and undergoes the time-tag permutation analysis. This simplifies the evaluations of the detectability criteria from P possibilities (Eq. 4.6) to C evaluations (Eq. 4.5) of the linear fit followed by N ! time-tag permutations. The approach is illustrated in Figure 4.11 for a three-pulse sequence.

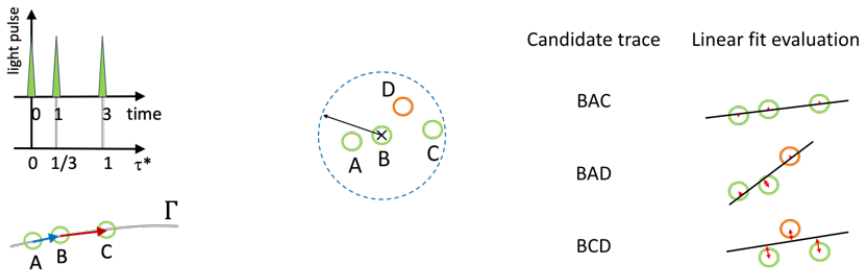

Figure 4.11.: Left: three-pulse sequence temporal template and the corresponding trace (bottom). Middle: search region and neighborhood around the selected mark. Right: linear fit evaluation of all trace possibilities, with the residuals shown in red.

4.6.2. DIRECTION DISAMBIGUATION

Once a candidate trace has been selected, the time-tag permutation analysis (block h) can be simplified by restricting the search to only those combinations where the velocity direction between subsequent illuminations does not vary beyond 90 degrees. The latter is considered a conservative criterion, considering that for most cases, a spurious time-tag permutation results in almost complete reversal of some displacements along the trace. The operation is computationally efficient considering that the trajectory has been approximated as rectilinear and the criterion is coded as sign reversal detection (dot product of subsequent displacement vectors, Figure 4.12). The result yields only two possible permutations (instead of N!). The two candidates are then inquired with the composite

detection criterion, as illustrated in the last column of Figure 4.12, for a three-pulse sequence.

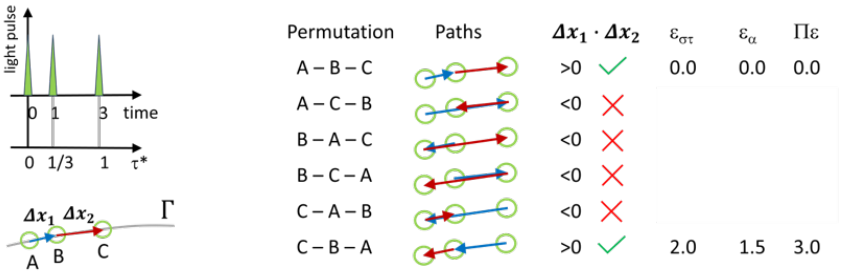

Figure 4.12.: Left: three-pulse sequence temporal template and the corresponding trace (bottom), together with the displacement vector Δx_1 and Δx_2. Right: time-tag permutation list, corresponding paths (blue for the first displacement and red for the second one), direction disambiguation and output of the detectability criteria for the appropriate permutations.

4.6.3. COMPUTATIONAL EFFORT

The effect of the proposed accelerators in the computational effort of the ME evaluation algorithm is summarized in Table 4.2, by comparing the CPU time required to evaluate the recordings presented in Table 4.1. The analysis compares the most expensive analysis, that makes no use of the above accelerators, the linear fit pre-selector and the linear fit followed by the direction disambiguation. All computations have been performed in a workstation equipped with an Intel Xeon W-2223 CPU.

N	3	4	5	6
CDC (no accelerator)	0.3 s	3 s	14 h	>1 day
Linear fit pre-selector	0.3 s	1 s	1 min	15 min
Linear fit + directional detector	0.2 s	0.5 s	20 s	3 min

Table 4.2.: CPU time required for the evaluation of the ME algorithm database.

The results indicate an explosive computational burden with trace length/rank when for the evaluation makes no use of accelerators. The linear-fit pre-selector provides already a strong reduction of the number of combinations, resulting in a substantial reduction of the computational effort the longer traces. Finally, the one-directional time-tag brings a modest reduction of computational effort,

yet appreciable for the longer sequences. It must be noted that the additional restrictions posed by the accelerators (straight trajectory, no direction reversal) may not hold true in highly turbulent regions, where the tracers follow highly curved trajectories. This may increase the occurrence of false negatives (missed detections) of such trajectories. Still, the accelerators represent a powerful tool to produce a first estimate of the velocity field, for use as a predictor in an iterative algorithm.

4.7. POTENTIAL AND BOTTLENECKS OF ME PTV

Several aspects deserve attention for the further pursuit of this technique. The main positive points are that the use of traces from ME recordings significantly lowers hardware requirements: the ME-PTV does not require high-speed imagers, neither short interframe separation time. It is therefore expected that experiments can be conducted using ordinary single-frame monochrome cameras. A second positive aspect is the reduction of data storage, as the velocity measurement is based on a single image. Furthermore, the free choice of the number of exposures allows to tune the image density. Finally, when compared with double-frame single-exposure, traces of 3 or more exposures offer a higher measurement dynamic range (Novara et al. (2023)), which compares to state of the art techniques based on time-resolved single-exposure recordings (e.g. STB). Among the most problematic aspects of this technique are the regions with low to zero velocity, where samples of the particle image will overlap and will not yield a distinct entry for the particle position. The current technique fails to detect traces in such conditions and additional criteria will be needed for the treatment of low-velocity conditions. A second point of attention is the limit of seeding concentration: the ME recording multiplies the number of particle images in a single recording and as such, it aggravates the problem of ghost particles formation. This aspect can be mitigated with the use of a multitude of cameras (e.g. N_{cam}> 10), currently not practiced in conventional 3D PIV experiments due to costs and complexity.

4.8. CONCLUSIONS

A novel measurement approach (ME-PTV) is proposed, to analyze the 3D motion of particle tracers, based on multi-exposed recordings. The specific choice of irregular timing of illumination produces traces from particle images, with a specific pattern, easier to recognize and at the same time, solving the problem of the unknown time-tag. The detection of a trace is based on kinematic similarity, reinforced with a kinematic regularity criterion that penalizes particle accel-

eration. All together these two criteria allow identifying traces from clusters of measured particle positions. The method requires the definition of a detection criterion, based on the SNR of the composite signal. The application to experimental data shows a maximum detection rate above 80% when N = 3, declining to approximately 60% for N = 6. Correspondingly, the error rate attains 6% and 0.1% for the above choices. More than 90% of the detected traces exhibit a SNR larger than 100, indicating the robustness of the trace detection algorithm. The sequence length is limited by the upper limits on image density and the occurrence of ghost particles. Furthermore, long traces involve an increasing computational effort due to the combinatorial nature of the search and detection algorithm. Based on the current study traces with 3 to 4 pulses are sufficient to guarantee a high detection rate error rate in the order of 1%. The lower limit of measurable velocity, due to the effect of overlapping particle images, is left out to the scope of the present work and will be the subject of further research.

II

APPLICATIONS

5

3D Quantitative Flow Visualization around a Thrust-Reverser

1

[1] Parts of this chapter have been published in: Hysa, I., Tuinstra, M., Sciacchitano, A., Scarano, F., Schwartz, N., Harrison, C., & Gebbink, R. (2023). Three-dimensional quantitative flow visualization around a thrust reverser. *AIAA*, *61*(12), 5404–5414.

5.1. INTRODUCTION

Aircraft engine thrust can be redirected by thrust reverser (TR) devices to rapidly decrease the aircraft speed at landing, after touchdown (Van Hengst (1992), Strash et al. (2000)). During aircraft operations, the behaviour of TR is critical: when the flow is reversed, the exhaust flow may be re-ingested, i.e. the circumstance whereby, the engine exhaust flow is redirected upstream of the engine and captured again at its inlet. Re-ingestion must be avoided as it negatively affects the engine lifetime and performance (Asbury and Yetter (1998), Bryanston-Cross and Sale (1992), Amin and Richards (1984)). Furthermore, the reversed flow up- or side-wards may interfere with control surfaces at the tail segments Van Hengst (1992) producing unwanted disturbances to the aircraft control, impairing safety.

Qualitative flow visualization techniques were most commonly adopted in the past to examine these two phenomena, as they provide an immediate and intuitive approach to the investigation of the flow topology. Studies using steam injection Van Hengst (1992) have shown that the two separate reversed jet plumes rapidly develop into three-dimensional flow patterns. Re-ingestion resulting from the interaction of the lower jet plume with the ground has also been observed Amin and Richards (1984). However, accurate predictions to optimize TRs' design and their operation require detailed quantitative flow information. At present, the aerodynamic design verification of such systems relies upon a combination of wind tunnel experiments and numerical simulations.

Most research works that report quantitative measurements of TR in wind tunnels make use of more traditional techniques, namely force balance (Strash et al. (2000), Asbury and Yetter (1998)), pressure (Asbury and Yetter (1998), Bryanston-Cross and Sale (1992)) and temperature measurements. The latter are used as a way to assess the conditions leading to re-ingestion by (moderate) heating of the jet plume and measurement of the intake flow temperature.

Van Hengst (1992) made use of surface tufts on the nacelle to study the flow topology induced by the TR, and the occurrence of flow separation on the rudder, in particular. Additionally, the reversed jet plume was visualized by vaporizing liquid nitrogen, as well as by steam injection. Amin and Richards (1984) also conducted visualization experiments in a water tunnel, injecting colored dye into the reversed jet, and compared their results to mist visualizations in the wind tunnel. These methods were effective to deliver a qualitative insight into the overall flow behavior and topology; however, the interpretation of the plume visualizations requires caution in that the smoke density varies and decays rapidly as a result of turbulent diffusion. Furthermore, the detailed analysis at specific planes of interest is hindered by the fact that only the plume bulk can be inferred. Finally, the comparison among experiments or with data obtained from numerical simulations requires quantitative data to lead to a conclusive investigation.

Early quantitative visualizations of the flow in a TR model were afforded by Bryanston-Cross and Sale (1992), who conducted planar particle image velocimetry (PIV) measurements that characterize the flow leaving the thrust reverser kicker plate. Their measurements indicated the suitability of PIV to investigate this complex flow problem, but were limited to the state of the art technology of PIV at the time (1992).

Over the past decade PIV has progressed to a reliable whole field measurement technique, which makes it a powerful tool in industrial aerodynamic research. One of the largest stereoscopic PIV systems was employed at NASA, where Wadcock et al. (2013) performed measurements in the wake of a full-scale rotor in forward flight encompassing a field of view (FoV) exceeding 4 m^2. Experiments of comparable scale include the helicopter rotor wake measurements at the German-Dutch Wind Tunnels (DNW) (Raffel et al. (2004), De Gregorio et al. (2012)). The study by the German Aerospace Center (DLR) group (Raffel et al. (2004)) involves cameras and lasers in a traversing system of 10 m x 15 m long. In an aircraft half-model wake measurement by the research group at the French Aerospace Lab ONERA (Carmer et al. (2008)), a ten-camera system with a purpose-built support was employed to cover the measurement entire domain.

Despite its advancements, as indicated by the complexity of these experimental setups, the application of PIV in aeronautics keeps posing a number of challenges: primarily, the region of interest often exceeds the size of the measurement domain, due to limitations in illumination and camera resolution. This challenge has been addressed by the introduction of larger, neutrally buoyant tracers: helium-filled soap bubbles (HFSB) (Scarano et al. (2015)). The superior light scattering of HFSB, compared to micron-size droplets Caridi et al. (2016) allows planar measurements over several square meters Spoelstra et al. (2019) using ordinary PIV illumination and imaging hardware. Such tracers, are however less abundant in the flow field and the resulting images feature a sparse distribution, compared to the experimental conditions of traditional PIV systems based on micron-size droplets. At lower levels of the seeding density, the recordings are optimally treated with particle tracking techniques, as opposed to cross-correlation analysis. The use of Lagrangian particle tracking Schanz et al. (2016) is proven effective for the reconstruction of particle tracks in volumes of the order of 1 m^3. In large-scale volumetric LPT experiments with HFSB, often volume partitioning has been practiced. Jux et al. (2018) measured a 2 m^3 volume by means of 450 sub-volumes, with coaxial volumetric velocimetry (CVV) and robotic arm manipulation (Schneiders et al. (2018)). Recently Schröder et al. (2022) illuminated a single, large volume (12 m^3) in a closed test room with a massive array of pulsed LEDs and captured the particles motion with multiple high-resolution cameras.

The application of HFSB and LPT in industrial wind tunnels is less frequent, given the time investment for system setup, conflicting with the high operational costs of large wind tunnels. In particular, for such applications, many efforts have been devoted to develop systems able to produce a large amount of HFSB and distribute them homogeneously and non-intrusively in the wind tunnel stream (Faleiros et al. (2019), Gibeau and Ghaemi (2018)). Using HFSB, Faleiros et al. Faleiros (2021) conducted stereoscopic PIV measurements in the wake of a tilt-rotor aircraft at the Large Low-speed Facility (LLF, 9.5 x 9.5 m^2 test section) of the DNW encompassing a of FoV 1.1 x 1.1 m^2. Also robotic PIV has been demonstrated by Sciacchitano et al. (2018) to perform quantitative flow measurements around a turboprop aircraft at the Low-Speed Tunnel (LST, 3 x 2.25 m^2 test section) of DNW, covering a measurement volume of 0.15 m^3.

In the present work large-scale 3D measurements are performed making use of HFSB as tracers in the LST (DNW) around an aircraft model with engines in TR configuration. The two main jet plumes resulting from the TR flow have been modelled as a free jet in cross-flow (top side) and a confined jet impinging on the ground board (bottom side), and are discussed under various jet to cross-flow velocity ratios. Similarities with simplified studies of jets in cross-flow (Barata et al. (1991), Barata et al. (1993), Nguyen et al. (2019)) have been drawn, with the purpose of discussing the large-scale flow organization.

The present objective is to advance the current state of the art of TR flow visualization by introducing large scale volumetric velocimetry, which allows resolving the flow field with higher detail while retaining the advantage of capturing large volumes, typical to smoke or steam visualization techniques. The chosen full-field 3D LPT approach, (as opposed to employing traversing systems) significantly decreases the wind tunnel operation time. A specific challenge of the present experiment is the setup of two separate seeding systems to trace the flow both in the wind tunnel stream as well as that exhausted by the TR jets. For the latter, a dedicated seeding generator is developed and integrated into the nacelle. The resulting measured flow-fields are used to elucidate the full three-dimensional complexity of the flow, illustrating the added value of the measurement technique to research and development of new aircraft.

5.2. EXPERIMENTAL APPARATUS AND MEASUREMENT CONDITIONS

5.2.1. WIND TUNNEL AND AIRCRAFT MODEL

The experiments were performed in the Low Speed Tunnel (LST) of the German-Dutch Wind Tunnels (DNW). LST is an atmospheric closed-return wind tunnel with a contraction ratio of 9. The test section has a width of 3 m, a height of 2.25

m and a length of 5.75 m. A 1:12 scaled model of a business jet aircraft featuring aft-fuselage mounted jet engines with bucket-type TR, installed in the test section is shown in Figure 1. The aircraft model has a total length of 2.092 m with a wingspan of 2.112 m. The pylons and nacelles were designed to allow thrust reversal on-ground. The centreline of the model nacelles was placed at a vertical distance of 0.3 m to the ground board.

The model was installed in the test section with a landing attitude in close proximity to a fixed ground-board, where it was attached with three struts, adjusted such that the model attitude was –1.3° for pitch and 0° for roll and yaw angle. Flaps were set at 42° angle and a set of inner wing speed brackets was also in place. The incidence of the horizontal stabilizer was put at its nominal setting of –2° angle. The rudder and elevator angles were set at 0° angle.

5.2.2. ENGINES AND TR

The model engines simulated both the inlet and exhaust flow. The latter was generated by compressed air, while the inlet flow was controlled via a suction system. The exhaust was reversed by setting the nacelle doors to TR configuration at angles θ_1 and θ_2 as sketched in Figure 5.2. The nacelle length is 520 mm.

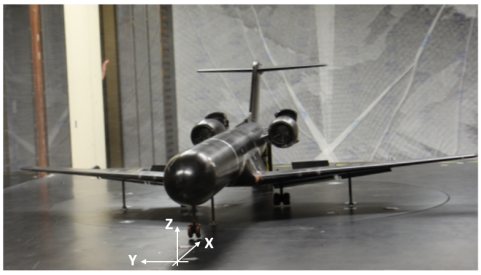

Figure 5.1.: Aircraft model installed in the DNW-LST and system of axes.

For an accurate simulation of the engine flow, the compressed air required to generate the exhausts was heated before being fed into the nacelles. A flow conditioning device was installed in each nacelle, consisting of a throttle plate upstream and downstream of its metal foam discs, with the purpose of homogenizing the exhaust velocity.

The compressed air mass flows to each individual engine were measured with high accuracy via two sonic venturis. The nozzle pressure ratio (NPR) is defined in Eq. 5.1 :

$$NPR = \frac{p_{t,nozzle}}{p_\infty} \tag{5.1}$$

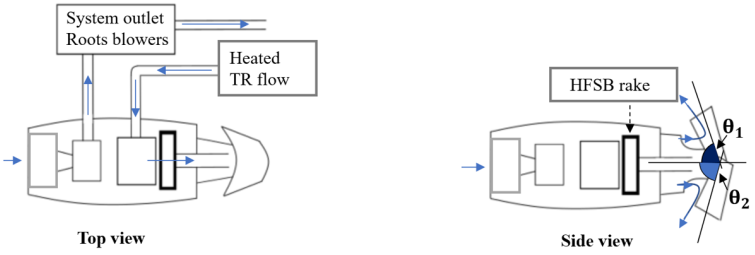

Figure 5.2.: Schematic representation of the engine in TR configuration with air suction at inlet, heated air supply at the exhaust and HFSB rake installed.

Where $p_{t,nozzle}$ is the total pressure measured with the pressure rake which was placed slightly ahead of the HFSB rake in order to avoid its contamination, and p_∞ is the static pressure of the free stream. These quantities were measured in real-time and the input voltage to the pressure regulator was set to achieve the desired NPRs. The exhausts were equipped with four rakes each containing three total pressure probes and one temperature probe. The rake legs were positioned at azimuth angles of 0, 90, 180 and 270°. The inlet ducts of the engines were equipped with six rakes, each containing four thermocouples, which were used for the re-ingestion detection. The azimuth angles of the rake legs are 0, 60, 120, 180, 240 and 300°. The locations of the thermocouples are shown in Figure 5.3. The temperature at each point was measured with an uncertainty of 0.5 – 1 K and the averaging measurement time for each point was 10 seconds. The measured inlet temperatures were used to check for re-ingestion.

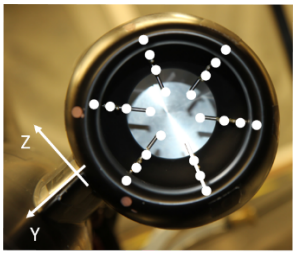

Figure 5.3.: Photograph of the engine inlet where the thermocouples' positions are denoted by white circles.

The re-ingestion parameter r, defined in Eq. 5.2 is the temperature difference between the total temperature at the engine inlet T_{inlet} (averaged across all inlet rakes) and the free stream total temperature T_∞, normalized by the difference

between the mean exhaust jet total temperature T_j (averaged across all exhaust rakes) and the free stream. This parameter is non-zero when re-ingestion occurs, and zero otherwise.

$$r = \frac{T_{inlet} - T_\infty}{T_j - T_\infty} \tag{5.2}$$

The chamber aft of the inlet duct was connected to a hole in the pylon through which access was gained to a plenum in the aft end of the fuselage. The inlet mass flow of both the port and starboard engine inlets were routed to this plenum. A Roots-type blower was connected to this same fuselage pipe to generate the suction. A mass flow meter in the suction pipe towards the Roots blower measured the total amount of air sucked.

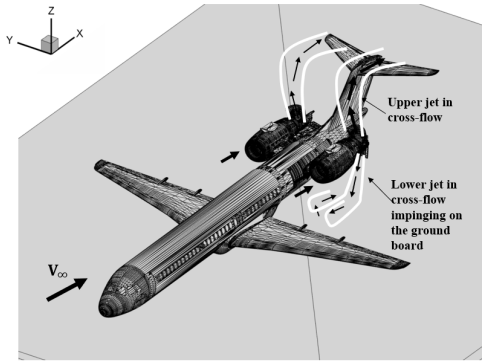

Figure 5.4.: CAD drawing of the aircraft model and coordinate axis in the origin of the measurement domain. Main flow features are outlined schematically.

The experiments reproduced full-scale conditions according to the criteria that the ratio of the momentum of the jet exhaust flow to the freestream flow denoted by λ in Eq.5.3, was kept constant between the full scale and model scale:

$$\lambda = \frac{\rho_j {V_j}^2}{\rho_\infty {V_\infty}^2} = const. \tag{5.3}$$

A simplified description of the flow arrangement is illustrated in Figure 5.4. The reversed jets develop across the outer stream in a flow-field that can be approximated as two inclined jets in relative proximity in cross flow. Whereas the upper jet plume is free to propagate upwards , the lower jet plume impinges on the ground. Under the assumption of flow symmetry due to zero yaw angle, the LPT measurements were conducted around only one of the engines.

5.2.3. 3D PTV APPARATUS AND PROCEDURES

In this section the integration of the large-scale LPT system in the LST wind tunnel is described. Details are given of the seeding systems, volume illumination and imaging as well as the data processing needed to produce the analysis of the time-averaged velocity fields.

WIND TUNNEL STREAM SEEDING

Two HFSB seeding systems were used in this experiment. A large seeding rake was used to seed the wind tunnel free stream and a small, tailor-made rake to seed the TR jet emanating from the engine exhaust. The freestream seeding rake comprised 10 wings, each with 20 HFSB generators, with a total of 200 HFSB generators. The generators were designed and CNC-manufactured at the NLR. A schematic of the nozzle of one of the generators is given in Figure 5.5, along with its main dimensions summarized in Table 5.1.

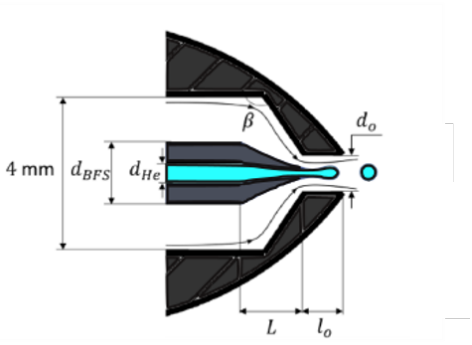

Figure 5.5.: Schematic section view of the bubble generators used in the experiments.

Parameter	Value
β	125 deg
d_{BFS}	2 mm
d_{He}	0.6 mm
d_0	1 mm
L	2 mm
l_0	1 mm

Table 5.1.: Dimensions of the NLR generator

The NLR design of the nozzle consists of a conical contraction region upstream of the orifice ($\beta > 90°$), in order to avoid flow separation at the junction between the cylindrical part and the end of the wall, where residues of recirculating soap fluid may accumulate under specific conditions.

The bubbles are introduced into the flow downstream of the tunnel's turbulence screen in order to avoid contaminating them. They are introduced in the settling chamber, so that most the flow interference caused by the rake decays along the wind tunnel contraction. The system releases tracers at a rate of 5 x 10^6 tracers/s with median diameter of 0.45 mm. A photograph of the seeding rake placed in the settling chamber of the DNW-LST is shown in Figure 5.6. A custom made Fluid Supply Unit (FSU) was used to control the supply lines for air, helium and soap, with attention to meet the neutral buoyancy for the tracers according to Faleiros et al. (2019). The two separate rakes were connected to the same FSU. The helium supply line was pressure controlled and the mass flow was monitored. The compressed air supply line was mass flow controlled. The soap flow was regulated by controlling the pressure of the soap tank and monitoring the mass flow the using the Mini Cori Flow from Bronkhorst. The soap solution used was the SAI 1035 from Sage Action, Inc. A particle filter was implemented in the soap supply line to prevent blockage of the mass flow meter or the flow restrictors. Digital pressure sensors were connected to the fluid supply lines at the freestream seeding rake in the settling chamber to remotely monitor for possible leakage.

Figure 5.6.: Wind tunnel seeding rake installed in the settling chamber.

ENGINE FLOW SEEDING

To seed the jet exiting the thrust reverser, a HFSB seeding rake was designed for the isolated nacelle. It is equipped with 8 bubble generators (total production rate 0.2×10^6 tracers/s) mounted in an aerodynamically shaped 3D-printed support. The rake was positioned such that the exit plane of the generators was slightly downstream of the internal total pressure rakes, to prevent total pressure rakes being contaminated by soap. Figure 5.7 shows a photograph of the internal seeding rake and its installed position inside the nacelle. Measurements were performed with different seeding conditions. First, experiments only seeding the engine jet were performed to visualize the trajectory of the exhaust bulk flow and compare them with temperature based re-ingestion detection. Later experiments with the seeded free-stream were made to quantify the interactions between the TR flow and the free-stream.

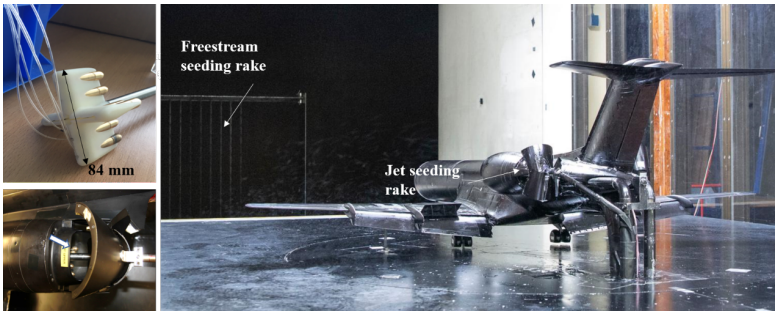

Figure 5.7.: Top left: internal jet seeding rake dimensions; Bottom left: position of the rake after installation in the engine; Right: overall view of the wind tunnel model with the free stream and the jet seeding rakes.

VOLUME ILLUMINATION

A Quantel EverGreen EHP30 (Nd:YAG laser, 300mJ/pulse) laser was used as an illumination source. The laser was illuminating the volume from approximately the same direction as the cameras. The laser beam was first expanded with a spherical lens and further sent through a beam diffuser. The laser was mounted on an X95 beam outside of the test section. This light source provided enough illumination intensity to cover a volume in excess of 1 m^3, when using HFSB. The laser was operated in double-pulse mode at a frequency of 10 Hz, with pulse separation ranging from 140 to 400 μs, depending on the flow speed.

IMAGING AND RECORDING

Three scientific CMOS cameras (sCMOS, PCO.Edge 5.5) were used to record the light scattered by the tracers within a measured volume of approximately 0.5 m^3. While it is possible in theory to perform 3D particle reconstruction with only two cameras, most volumetric PIV/PTV experiments involve three or four cameras in order to minimize false particle reconstructions Wieneke (2012). The choice of three cameras (instead of four) was done in favour of simplicity, and it was possible in this case due to the particle concentration being below 0.1 particle per pixel (see Section C.5 for more details on particle concentration). At higher seeding densities, more than three cameras might be necessary for accurate 3D particle reconstruction.

The dimensions of the measurement domain, along with the respective positions of the cameras and the laser are illustrated in Figure 5.8. The cameras were arranged in a 2D configuration, mounted on X95-beams outside of the test section, and spanning the plane highlighted with blue in the sketch. The total aperture of the system is 35°. The measurement volume in the streamwise extent covers the engine inlet, thrust reverser and aircraft tail. In the vertical direction, the volume encompasses the ground and the horizontal stabilizer. An overview of the imaging parameters is given in Table 5.2.

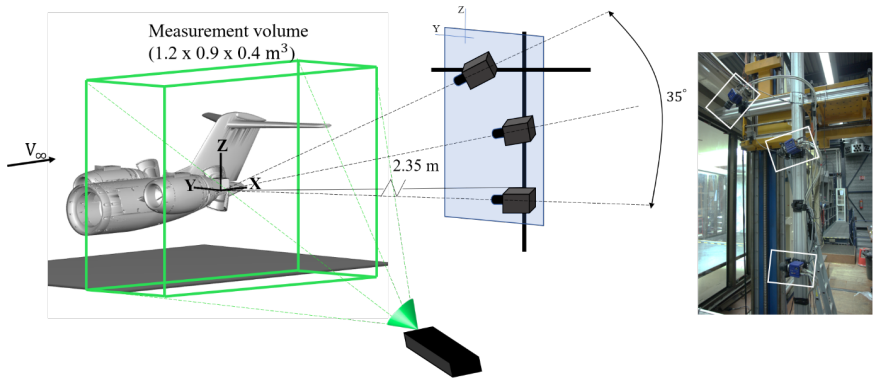

Figure 5.8.: Left: Schematic illustration of illumination and imaging layout. The measurement volume is highlighted in the green box. The laser and the cameras are on the same side of the model. Orientation axis is centered at the origin of the PIV measurement volume; Right: Photograph of the cameras installed outside of the test section.

The arrangement of the laser and cameras results in some regions without optical access due to shadows. The shadows result from the TR doors and the wing. Additionally, the nacelle casts a shadow in the region between the nacelle and

Parameter	Value
Laser pulse separation (double-pulse) [μs]	150
Recording frequency [Hz]	10
Sensor size [pixels]	2560 x 2160
Image sensor pixel pitch [μm]	5.6
Magnification	0.018
Objective focal length [mm]	35
Numerical aperture	5.6
Nr. of recordings	250
Measurement volume [m^3]	1.2(X) x 0.4(Y) x 0.9(Z)

Table 5.2.: Summary of imaging parameters

the fuselage. The model was completely painted in black, however some reflections did result, most notably around the engine inlet and in the TR doors due to accumulation of soap, as can be seen in Figure 5.9, left. The geometrical image of HFSB tracers covers approximately 1.4 pixels in the images. The small angle between illumination and imaging causes the two glare points, characteristic of the HFSB imaging, to merge into a single one Faleiros (2021). The final diameter of the such glare reflection is approx. 3 px, mostly as a result of diffraction. Image pre-processing was applied to improve the detectability of particle images for the LPT analysis, with the resulting images and a close-up of the particles - shown in Figure 5.9, right.

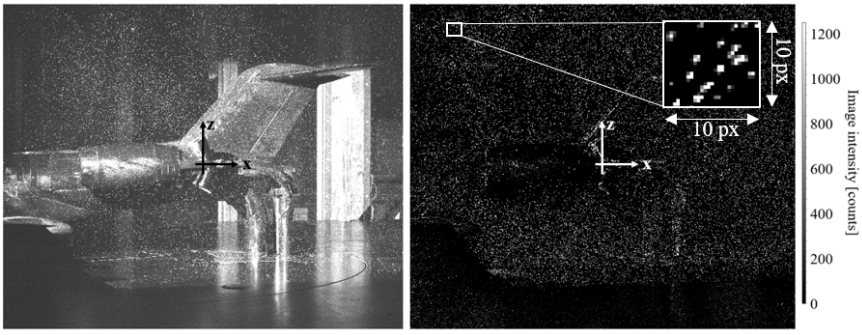

Figure 5.9.: Left: raw image from camera 3. Right: same image after pre-processing (counts refer to both images).

Digital image processing was performed with the purpose of eliminating background reflections, in order to maximize the amount of detected particles : minimum pixel intensity subtraction over time (with a filter length of 7 recordings);

sliding spatial minimum intensity subtraction based on a neighborhood of 7 x 7 pixels; intensity normalization based on a local intensity averaged over a window of 150 x 150 pixels. Finally, the intensity of each frame was normalized to the first frame.

DATA PROCESSING

For the measurements conducted with seeding in the free-stream a total of approx. 200.000 particles are captured in each recording (particle image density of 0.05 particles per pixel), corresponding to a tracers' concentration of 0.5 particle/cm^3. About 75.000 of the detected particles are accepted into valid tracks. In the freestream, a particle is displaced of approx. 5 pixels between the two frames. The particles 3D positions are obtained with the iterative particle reconstruction (IPR) algorithm Wieneke (2012), and tracked using the Shake-the-Box algorithm for two-pulse recordings Novara et al. (2023), implemented in LaVision DaVis 10.1.2 software. The instantaneous velocity is obtained at scattered locations and converted to a Cartesian grid over cubic cells of 1 cm^3. Each velocity sample falling within the a cell forms an ensemble yielding the time-averaged velocity vector at the cell center. The measurements domain encompasses 120 x 40 x 90 cm^3 and the velocity is described with a grid of 230 x 80 x 181 nodes (adjacent cells overlap by 50%) and 5 mm vector spacing. With this 10 mm bin size, and the recording frequency of 10 Hz, biases associated with the ensemble binning scheme such as double counting of particles take effect in regions with absolute value of velocity below 0.01 m/s. Most of the low speed regions of interest such as the wake of the jet feature higher velocities, and overall the number of bins with velocities lower than 0.01 m/s comprise less than 1% of the domain volume. Therefore this is not considered to be a significant factor in this measurement. Every bin comprises approx. 5.000 samples, however the concentration varies across the measurement domain. A criterion of at least 50 valid data tracks per bin is set. At these conditions the bin size is $1/10^{th}$ of the jet diameter. A measurement of the spatial dynamic range, DSR of 120 is attained from the ratio between the largest and smallest measurable scales. The measurement accuracy is evaluated via the dynamic velocity range (DVR), defined as the ratio between the maximum and minimum resolvable levels of velocity. In the present case the maximum velocity occurs at jet centerline. For the minimum resolvable velocity an estimation of the velocity uncertainty is required. Following Agüera et al. (2016), the measurement uncertainty is statistically determined by the ratio between the relevant velocity fluctuations (axial and vertical velocity standard deviation in this case) and the square root of the amount of samples per bin. In the regions of the jet core, where the highest turbulent fluctuations were recorded, the measurement uncertainty is approx. 0.4 % of the maximum measured velocity. In the rest of

the domain this value is below 0.1%. Taking an average value of the u' and N_p across the domain results in DVR = 200. For the purposes of flow topology visualization and re-ingestion detection measurements with jet seeding only were conducted. For these measurements there were on average 20.000 particles continuously tracked between the two frames. The bin size for the averaging was chosen to be 20 mm with 75% overlap in order to achieve velocity convergence with reduced particle density. Approx. 1.200 particles are sampled per bin (in the region of the seeded domain). The measurement uncertainty is in the order of 0.6% of the peak measured velocity in the seeded domain. This uncertainty increases to up to 1% in the limits of the domain due to the reduced seeding in these regions. It is important to note that even though the tracking technique is called Lagrangian Particle Tracking, the two-pulse measurement does not allow for the reconstruction of long Lagranian trajectories in time. This is particularly relevant to keep in mind with regard to the re-ingestion detection results shown in the next section. Re-ingestion identification was accomplished by inference on the presence of particles in regions close to the engine inlet, rather than by following particular trajectories from the exhaust back to the inlet. Further analysis of the time-averaged binned velocity vector fields is performed in Tecplot 360 EX R2, where the volumetric flow field data is overlaid onto the CAD geometry of the wind tunnel model.

5.3. EXPERIMENTAL RESULTS AND ANALYSIS

5.3.1. GLOBAL FLOW TOPOLOGY

The time averaged velocity fields obtained with the two different seeding strategies, i.e. homogeneous seeding and jet-only seeding, are shown in Figure 5.10 next to a photograph taken during a visualization experiment produced with steam injection at comparable freestream velocity and NPR ($V_{jet}/V_\infty = 2.5$). The steam visualization was obtained on the same aircraft model, but employing a different thrust reverser configuration. Therefore, the goal is not one-to-one comparison, rather the presentation of the advancement that quantitative flow visualization offers over the qualitative state of the art. The streamlines extracted from the velocity field results elucidate a number of flow features. Initially the jet plumes propagate in the direction set by the TR door orientation, before bending downstream due to momentum exerted on them by the freestream flow. Behind the jet a quasi-stagnant region is created in which the horizontal tail and the control surfaces are immersed. The lower jet plume is obstructed by the ground plane, as also seen in the steam visualization. A separation bubble is observed, where the incoming boundary layer separates under the effect of the increased pressure at the jet stagnation point. This recirculation region is identified as the

primary mechanism for jet plume re-ingestion. With NPR increase the separation bubble size will also increase until the point (part) of the jet plume is re-ingested into the inlet.

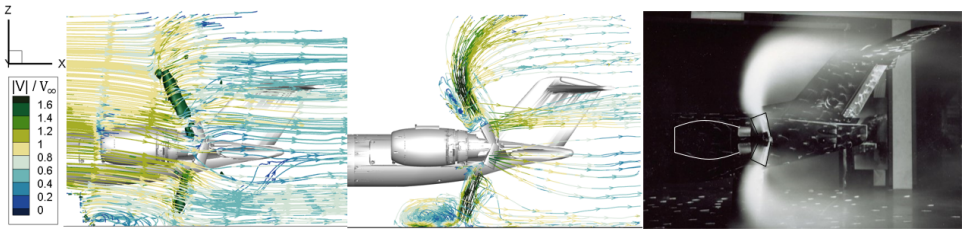

Figure 5.10.: Left: time-averaged velocity field from the LPT measurement visualized with color-coded streamlines homogeneous domain seeding; Middle: Same point with jet seeding only; Right: reversed jet visualized with steam (nacelle and TR doors have been highlighted).

As discussed in previous studies, the interaction of a jet impinging on a flat surface has a complex flow field. In these works planar PIV in the midplane through the jet, laser doppler velocimetry and quantitative flow visualizations were employed to study the jet properties in simplified conditions. The principal factors affecting the resulting flow-field properties were identified as: nozzle shape, the jet to crossflow velocity ratio, the nozzle to ground plate distance, the presence of confinements, the number of jets and their relative proximity. The variation of these factors was studied and the flow was typically divided in a number of characteristic regions Barata et al. (1991). For the study at hand the two jet plumes coming out of the TR can be understood as follows: the top plume as a free inclined jet expanding into crossflow and the lower one as an inclined jet in crossflow impinging on a ground plate. Here the distance to the ground plate is fixed to the landing configuration distance, and so is the TR doors shape. The factor that was varied is the jet to freestream velocity ratio. The current case is made more complex by the TR door geometry, the presence of distortions upstream in the cross-flow due to the presence of the wing, fuselage and nacelle, and the inclination of the jet to the freestream, as outlined in Figure 5. Additionally, the NPR and freestream velocity conditions are significantly different, so the goal in this section is not direct quantitative comparison, instead it is revealing the large-scale structures present in the flow.

Following Nguyen et al. (2019) the jet plume is roughly separated in three regions as illustrated in Figure 5.11. These include a region where the flow behaves like a free jet; an impingement region, where the flow structure is affected by the presence of the impingement plane; and a wall jet region, where the flow devel-

ops in the radial direction along the impingement surface. This wall jet is then observed to recirculate in vortical structures similar to what is observed by Barata et al. (1993), although different in magnitude. For the investigation of exhaust re-ingestion, the propagation of the wall jet upstream of engine intake, as well as the extent of the recirculation region above the ground plane are critical.

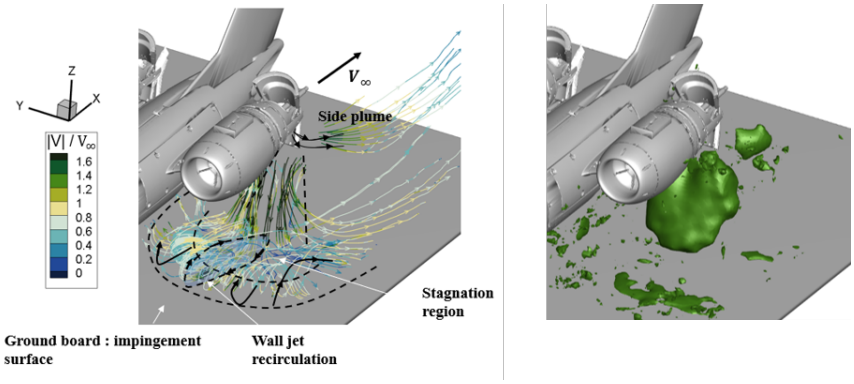

Figure 5.11.: Left: Lower jet flow structures visualized with streamlines. The rest of the flow-field has been omitted for clarity. Right: Velocity magnitude iso-surface at $V/V_\infty = 1.3$.

Additional to the main jet plume, secondary small plumes are captured by this experiment, i.e. flow leaking from the side of the TR door close to their hinge point. Such side plumes are also reported from previous steam visualizations of Van Hengst (1992). They can be clearly observed on the outer side of the engine (negative y-direction), however it is not possible to observe the occurrence of this side plume on the side of the fuselage due to limited optical access and the shadow of the engine on that side. In multi-jet impingement studies it is reported that the jets of the two operational engines will interact with each other, establishing a plane of symmetry in between on which the flow topology is mirrored. Inspection of the flow topology from the rear of the airplane, depicted in Figure 5.12, shows that the wall jet recirculation is asymmetrical, having a smaller radius and a higher vertical velocity component magnitude on the side next to the fuselage. This is explained by a stagnation region in the symmetry plane near the ground surface, created at the locations where the two wall jets impinge onto each other. The 'free side' of the recirculation bubble on the other hand is wider and with lower vertical velocity components. The wall jet is only lifted from the surface and is then deflected downstream further in the x-direction as can be more clearly seen in Figure 5.10 left.

In contrast to the lower plume, the upper plume is unobstructed, slowly reori-

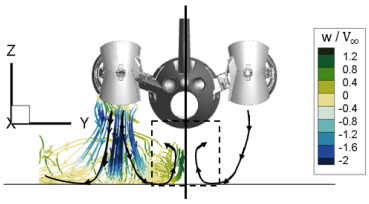

Figure 5.12.: Back view of the lower jet visualized with streamlines. The region where interactions between the two jets is expected is outlined in the dotted box and the plane of symmetry along the x-z plane is denoted with the black line.

enting in streamwise direction by the exerted momentum of the free-stream flow. The flow field of the upper jet can be divided into four-regions: the jet-crossflow interface, the jet core, the jet wake and the flow leakage from the gap between the TR doors, illustrated in Figure 5.13. The jet-crossflow interface constitutes a stagnation region, which is also to be seen in the right, where streamlines around the center-plane through the jet emanating from the freestream region have been plotted (the jet has been omitted for better visibility). It can be seen that the freestream is deflected around the jet sideways, up to the point denoted by the arrowhead, at which point the flow starts to get deflected upwards.

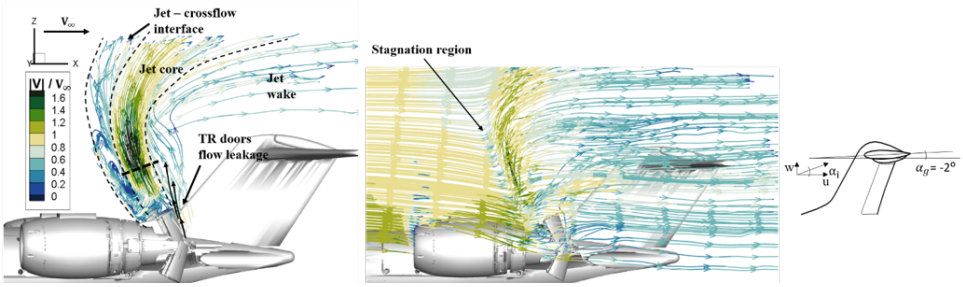

Figure 5.13.: Left: Top jet plume regions visualized with streamlines. Middle: Freestream flow deflection around the jet. Right: Schematic of the local flow over the horizontal tail.

The upper plume flow is of no relevance for flow re-ingestion. However it can play a role in the controllability of the aircraft due to the possible interaction with the rudder. Particularly in cases of landing with a sideslip angle the plume hitting the rudder can be detrimental to aircraft control (Van Hengst (1992), Amin and Richards (1984)). In the conditions with 0° sideslip measured in this experiment, this situation is not observed in any of the measured points. However, it is seen

that the pitch control surfaces (elevators, horizontal tail) are immersed in the wake of the jet.

To quantify to what extent the local velocity ahead of the tail is altered by the presence of the plume, an effective angle of attack of the tail is be defined as:

$$\alpha_{effective} = \alpha_i + \alpha_g \tag{5.4}$$

Where the angle of the local flow over the tail α_i , and the geometrical angle of the horizontal stabilizer α_g are shown schematically in Figure 5.13, right. As noted in Section II, the horizontal tail is set at α_g fixed at -2°. α_i is calculated from the atan (w/u) ahead of the tail. This angle is rather small (< 0.1°) in all conditions, except for the two with the highest λ (Eq.5.3). In the condition of λ = 35, the incoming flow to the horizontal tail is at approx. 3°, resulting in an effective of attack $\alpha_{effective}$ of 1° . For the case of λ = 24, the incoming flow is oriented at 1.8°, resulting in approx. 0° effective angle.

5

The core region of the jet is characterized by a maximum jet velocity along the centerline with a bell-shaped mean velocity profile. This is illustrated in Figure 5.14 which shows the time averaged velocity profile and the standard deviation of the axial and radial velocity components extracted along the line denoted across the jet core in Figure 5.13, left. Here a local coordinate along the jet normal direction is normalized by the jet exit diameter j_d (determined by the geometry of the engine).

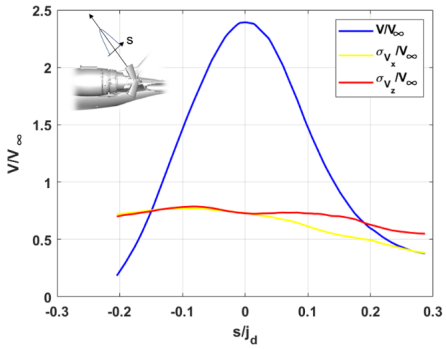

Figure 5.14.: Velocity magnitude profile of the jet core, along with the axial and radial velocity fluctuation components.

The velocity fluctuations along the axial and radial directions are in the order of 100% of freestream velocity values. This is not typical of fully developed top-hat profile jets where the fluctuations are small in the core and peak in the shear layers around the edges. Instead this jet is unsteady and fluctuating strongly along

the entire jet diameter.

Additional flow features such as the flow leakage between the deployed TR doors are observed. This is the flow escaping from a gap in between the deployed TR doors and relates to TR efficiency considerations, due to the fact that the amount of flow effectively reversed is decreased by these leakages. For the current TR model the area of this gap measured from the TR geometry is approximately 5% of the total opening area for flow reversal.

5.3.2. COMPARISON WITH TEMPERATURE BASED RE-INGESTION DETECTION

Re-ingestion detection measurements with temperature rakes have been conducted for a velocity sweep with fixed NPR (which was the highest NPR tested as it is the most critical for re-ingestion). The re-ingestion parameter r, as defined in Eq. 5.2, is zero for cases where no re-ingestion is detected, and positive otherwise, with a higher value suggesting larger parts of the plume are re-ingested. These results are plotted in Figure 5.15.

The LPT measurements for the same velocity sweep have been plotted in the midplane through the nacelle in Figure 5.16, where each condition is directly compared to the temperature results. Measurements with jet seeding were considered, in order to unambiguously detect the presence of particles originating from the jet. Therefore in the interpretation of the results the presence of particles at the engine inlet or ahead of it is taken as evidence of re-ingestion.

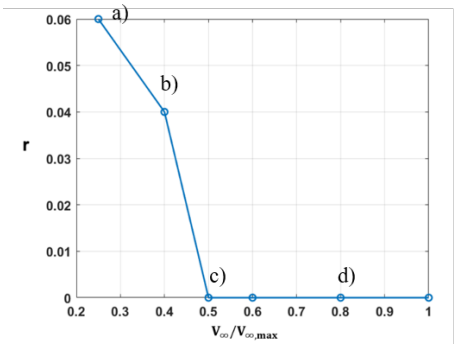

Figure 5.15.: Temperature rake re-ingestion parameter vs. freestream velocity. Cases a), b), c), d) correspond to the cases in the following velocity contour plots.

It can be seen that these time-averaged results show good agreement. As discussed in the previous section, the mechanism that gives rise to re-ingestion is

the recirculation of the wall jet resulting from the lower plume impinging on the ground board. The size of this recirculation region both in the axial as well as vertical direction are critical in terms of closeness to the engine inlet.

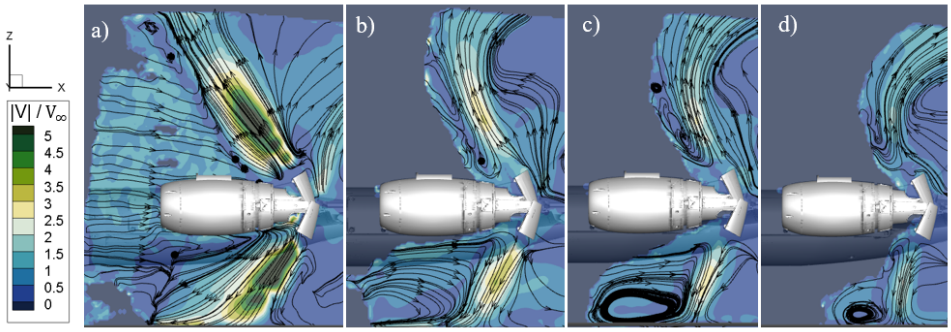

Figure 5.16.: Normalized velocity contours and surface streamlines in the mid-plane through the nacelle. Freestream velocity increasing left to right, NPR fixed. Regions with no vector information are a result of limited particle count from the jet seeding.

In both conditions a) and b) it appears that the recirculation extends further upstream under the wing, but due to the shadows of the wing (as well as the fact that this region is in the limit of the domain) the measurement there is not available.

The magnitude of re-ingestion is also in agreement between the temperature measurements and LPT, whereby the higher re-ingestion parameter corresponds to a higher amount of particles detected. The rest of the points have zero re-ingestion. The LPT measurements confirm this. In point c) the size of the re-circulation bubble is considerably smaller, and does not seems to approach the inlet on average, and in the last point d), the freestream to jet momentum is increased to the point that the forward propagation of the jet is minimal.

The LPT results can be seen as complementary to the temperature measurements, in that they elucidate the aerodynamics leading to re-ingestion.

5.3.3. PARAMETRIC ANALYSIS WITH NPR AND MOMENTUM RATIO

In this section results of measurements with varying conditions are presented: a flow topology variation with a freestream velocity sweep at fixed NPR, and the jet profile variation with NPR sweeps at two different freestream velocities.

The two main jet plumes and the side plumes have been visualized with velocity iso-surfaces and plotted for a velocity sweep in Figure 5.17. The value taken to obtain the iso-surfaces is varied for each condition for better visibility. The

jet to freestream momentum is increasing left to right (as the freestream velocity decreases), and as expected so is the forward propagation of the jet. It can also be observed that the jet diameter increases as well in this direction, i.e. the jet expands more when V_{jet}/V_∞ is higher, and is thinner otherwise.

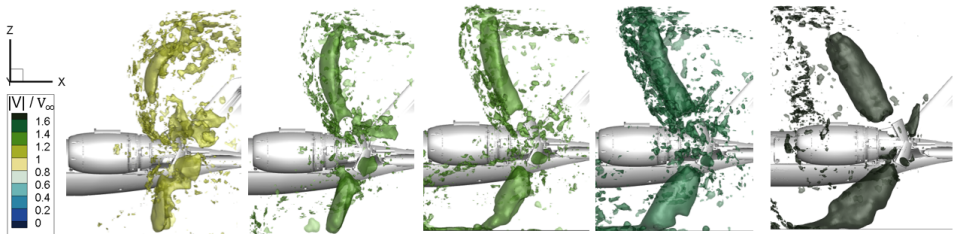

Figure 5.17.: Velocity iso-surfaces for increasing V_{jet}/V_∞ left to right.

Additionally measurements with NPR sweeps at two fixed freestream velocities have been performed. Here seven different NPR values are plotted in Figure 5.18 with conditions of V_{jet}/V_∞ varying from 1.5 to 6. The legend of the graph in the left denotes the jet momentum to freestream ratio λ as defined in Eq. 5.3. The dashed lines represent the first NPR sweep at $V_{\infty,1}$ and the solid lines represent the second NPR sweep at a lower freestream speed of $V_{\infty,2} = 0.4\ V_{\infty,1}$. The jet profiles are extracted normal to the jet for all the different conditions along a constant radial distance from the top TR door.

Not only the jet velocity, but also its orientation varies with the different conditions. This is shown in Figure 18 right, where the angle the jet centerline makes with the horizontal is normalized with the angle of the upper TR door and plotted. The color coding matches the conditions on the left, with the solid circles corresponding to the solid lines, and the asterisks corresponding to the dashed lines.

It can be observed that as the jet to freestream momentum increases, the jet is more strongly reversed, as is to be expected. The last two conditions (green and red dashed lines and asterisk angle) correspond to effectively no jet reversal. The jet does not propagate forward but is defected downstream under these conditions, as demonstrated by the fact that the angle it makes with the horizontal is larger than the geometrical angle of the TR door. It can also be observed that conditions with different velocity and NPR, but a very similar momentum ratio ($\lambda = 5$ and $\lambda = 4.7$, denoted by the black dashed line and the red solid line), likewise have an almost identical velocity distribution as well as deflection angle, which is in line with the scaling theory.

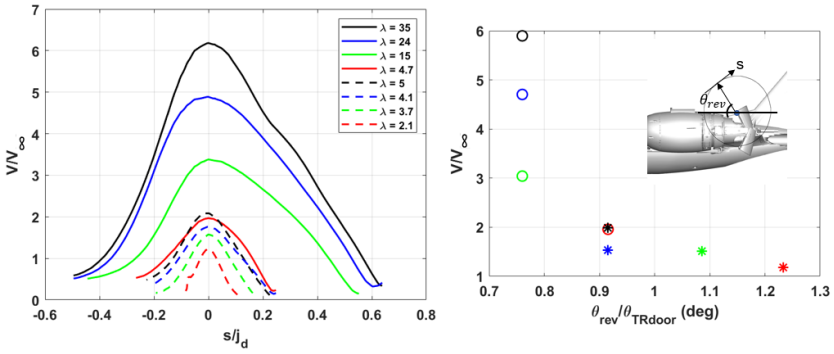

Figure 5.18.: Jet mean velocity profiles for measurements featuring NPR sweeps at two different velocity freestream values.

5

5.4. CONCLUSION

A quantitative flow visualization technique was successfully demonstrated for the investigation of thrust reverser flows in an industrial wind tunnel environment. The large-scale volumetric velocimetry measurement was made possible by employing Helium-Filled Soap Bubbles as flow tracers. Flow seeding was achieved with two separate seeding rakes, one integrated inside the nacelle and one in the wind tunnel settling chamber. The need to introduce particle tracers in the engine exhaust flow complexifies the implementation of this kind of measurements, and in this case it was dealt with by employing a small HFSB generator array tailor-made to fit the engine nacelle. The most effective visualization strategy was found to be to perform measurements with jet-only seeding, alongside the jet and free-stream flow seeding. Testing was completed in typically 3-5 minutes per condition following a full-field approach, as opposed to scanning the domain, where the time needed for the measurements is multiplied by the number of scanning planes/volumes. The wind tunnel experiments were conducted at the DNW-LST on a 1:12 scaled thrust reverser, part of a full aircraft model. A measurement volume of 0.5 m^3 was attained, capturing the full complexity and three dimensionality of the flow field. Employing Lagrangian particle tracking, a quantitative assessment of the flow velocity was achieved, with a vector resolution of 1 cm. A key advantage over classical flow visualization techniques is that the flow field may be studied at specific planes and from various perspectives. Several flow features were elucidated, such as flow reversal, jet plume recirculation due to ground effect, flow leakage and re-ingestion. In conclusion, large-scale velocimetry offers key insights into the flow features that lead to re-ingestion, complementary to the inlet temperature probe based

detection criterion.

6

3D PTV around a Ship at Varying Wind Directions

1

[1] Parts of this chapter are presented in the 21st International Symposium on Flow Visualization, Tokyo, Japan.

6.1. INTRODUCTION

The continuous progress in particle tracking velocimetry over the last years has enabled large-scale volumetric measurements to be carried out in increasingly more advanced applications. Nevertheless, particularly in volumetric measurements, a frequently encountered bottle-neck is the limited spatial coverage around test object with complex geometries, arising from shadows, blocked line of sight of the cameras, and the requirement for dedicated image processing algorithms, as elaborated on Chapters 2 and 3. The study presented in Chapter 3 focused in the field of wind engineering, particularly the aerodynamics of the top-side of ships, where the problem of blocked optical access is particularly restricting due to the necessity to measure the flow field at various incoming winds (equivalent in the wind tunnel to various model rotation angles). Although this work demonstrated the potential of multi-directional systems to measure all around the test object – in this case a Simplified Frigate Ship (SFS), the experimental campaign was carried out at a single wind direction (headwind), not fully disclosing its capability.

A study of Lagrangian particle tracking (LPT) in the presence of obstructing objects was carried out by Wieneke and Rockstroh (2024), where Object-Aware LPT was presented. Using an implementation of depth maps of the known test object geometry within Shake-the-Box (Schanz et al. (2016)), the authors showed that they were able to retrieve data in partially occluded regions of the measurement domain. They validated their algorithm on synthetic data, as well as on an experimental dataset of the flow around a cylinder in water.

The work presented here is a higher technological level implementation of the study of Chapter 3, with the goal to evaluate the impact of multi-directional volumetric velocimetry systems not only for complex geometries, but also for multiple configurations. The results aim to capture the realistic description of the aerodynamics on the landing deck of naval vessels across these configurations.

The demand for helicopter and Unmanned Aerial Vehicle (UAV) operations on naval vessels, particularly frigates, necessitates a thorough understanding of the aerodynamic environment at the helideck. The Ship Helicopter Operational Limits (SHOLs) testing procedure consists of sea trials and velocity measurements in wind tunnel tests on scaled models of the vessels (Forrest et al. (2012), Shukla et al. (2019)). The superstructure of navy ships consists of non-streamlined shapes with sharp edges, that cause areas of flow separation with steep velocity gradients, unsteady recirculating flows and turbulent eddies of varying sizes and energies (Seth et al. (2021)).

SHOL investigations at multiple wind directions with high-fidelity computational methods are expensive, and the different variations of low-fidelity models need extensive experimental data for validation.

To this end, a description of the experimental apparatus employed in this experimental campaign for the flow measurements around a scaled model of an Ocean Patrol Vessel (OPV) is given in the following section. The results of the time-averaged velocity and vorticity fields are shown in the Results section, along with a comparison with selected results from the Simplified Frigate Shape (SFS) geometry. Finally modal decomposition of the flow-field over the flight-deck is presented to investigate the large-scale coherent structures in the flow field.

6.2. EXPERIMENTAL APPARATUS AND MEASUREMENT CONDITIONS

The experiments were performed in the Low Speed Tunnel (LST) of the German-Dutch Wind Tunnels (DNW). The characteristics of the test section are detailed in Chapter 5.

6.2.1. SHIP MODEL

The model used was a 1:70 scaled down and slightly simplified version of the OPV, depicted on the right of Figure 6.1. Its dimensions include a length of 1549 mm, a width of 229 mm, and a height of 389 mm. Starting from the bow, the model features a superstructure that extends aft. The bridge is positioned forward of the mast, which sits atop the superstructure. The superstructure includes the hangar at its rear, with the helideck positioned at the aft of the model.

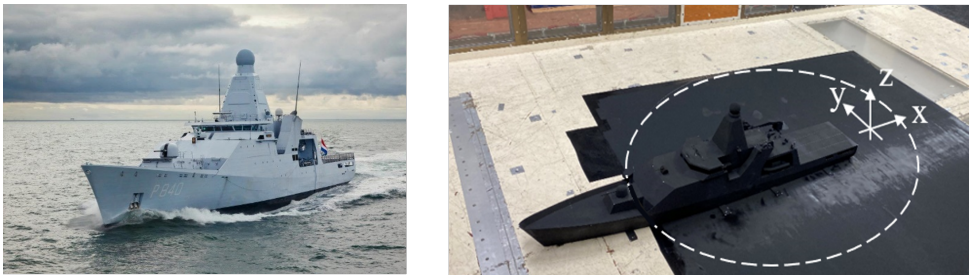

Figure 6.1.: Left: Photograph of the Ocean Patrol Vessel at sea. Right: Photograph of the ship model installed in the test section of the LST, along with system of coordinates.

The main dimensions of the baseline OPV model are shown in the Figure 6.2. The length L = 401.86 mm, and width B = 220.57 mm of the helideck, and the height of the hangar H = 85.71 mm, are used to normalize the results. The model was mounted on the test section turntable in order to measure at different in-

coming wind configurations from -90° - 90° with 45° steps with an empty helideck. Additionally a configuration with the removed mast was tested.

The Reynolds number based on the height of the hangar over the flight-deck is Re_H 28.000, and the case for Reynolds independence that was made in Chapter 3, is also valid here, given the non-streamlined features in the superstructure.

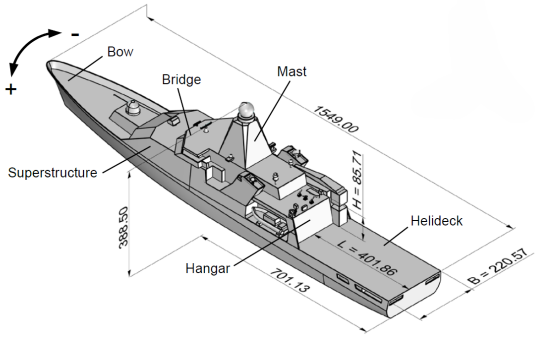

Figure 6.2.: Main dimensions in mm and nomenclature of the different ship parts.

6.2.2. 3D PTV APPARATUS AND PROCEDURES

FLOW SEEDING

Neutrally buoyant HFSB with 0.45 mm diameter were employed as flow tracers. An in-house developed seeding rake comprising 56 generators in an 8x7 grid was installed in the settling chamber of the LST. The pitch between generators is 15 cm in either direction. The system delivers approximately 1.4x10^6 tracers per second, distributed over a cross-section of approx. 60 x 50 cm^2. The contraction of the wind tunnel is 1:9. The seeding generator unit was controlled through an in-house built fluid supply unit. At the freestream velocity tested, the seeding concentration is estimated as approx. 1 tracer/cm^3, resulting in a particle per pixel value of 0.01.

VOLUME ILLUMINATION

The particles were illuminated with two Quantel Evergreen Nd:YAG (2 x 300 mJ/pulse). Illumination from four directions was achieved by sending the laser beams through beam splitters, minimizing the regions of total shadow in the domain of interest. The beams were then expanded with f= -100 mm spherical lenses and diffused through diffuser grids to achieve a homogeneous illumination intensity and re-

move speckle patterns. The directions of the illumination are shown in the sketch in Figure 6.3.

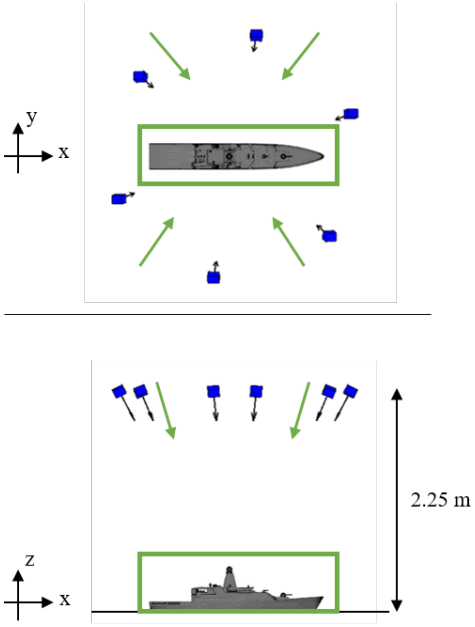

Figure 6.3.: Schematic of the multi-directional setup.

IMAGING AND RECORDING

The 3D imaging system comprised of six sCMOS cameras (2560 x 2160 pixels, 6.5 μm pixel pitch, 16 bits) equipped with f = 35 mm objectives, set at a numerical aperture $f_{\#} = 8$. The latter yielded sufficient depth of field to obtain sharp particle images along a depth of 40 cm.

As the model has a rather large aspect ratio of approx. 7, to achieve a compromise between the field of view and spatial resolution, the domain was measured in 4 separate sections, covered by translating the model in such a way as to ensure sufficient overlap.

This was achieved without re-arrangement of the illumination and imaging system. The cameras were arranged such as to minimize the losses in every viewing direction, in accordance with the considerations that were explained in Chapter 3.

The pulses time separation of dt = 600 μs yields a particle image displacement of approx. 10 pixels in the freestream.

The calibration was performed with a standard PIV 2D calibration plate, translated along the depth of the volume, prior to model installation. The geometric calibration was followed by volume-self calibration Wieneke (2008), reducing residual reprojection errors to a tenth of a pixel.

Synchronization of illumination, image acquisition and data recording were achieved with a LaVision programmable timing unit (PTU-X) and controlled with Davis 10.

Figure 6.4.: The full 3D PTV setup.

A photograph from the PIV setup in the test section is shown in Figure 6.4. The model and background were painted matt black, in order to minimize reflections, however in the end analysis some reflections in some of the cameras were unavoidable. Background subtraction and image normalization filters were applied to the raw images in order to increase the signal to noise ratio of the particle images.

Table 6.1 summarizes the PIV measurement parameters.

DATA PROCESSING

Data processing was carried out with a research release of Davis 11, that implements Object Aware Velocity Estimation. A brief overview of the method is provided here and for a detailed description of the algorithm the reader is referred to Wieneke and Rockstroh (Wieneke and Rockstroh (2024)).

Object shape and position were included from the drawings of the model. The

Parameter	Value
Laser pulse separation (double-pulse) [μs]	600
Recording frequency [Hz]	10
Sensor size [pixels]	2560 x 2160
Image sensor pixel pitch [μm]	6.5
Magnification	0.0195
Objective focal length [mm]	35
Numerical aperture f#	8
Measurement domain	0.6 x 0.5 x 0.4 m^3
Nr. of recordings	500/1000

Table 6.1.: Summary of measurement parameters

model alignment to the data was performed manually, by matching some pre-designated markers on the object with the geometry. The accuracy of the alignment is in the range of 1-5 mm, most likely resulting from small differences between the drawing and the manufactured model.

The images raw data quality was found to vary greatly between the cameras, with some cameras having SNR 200 averaged across the domain after pre-processing, and other cameras being dominated by reflections. This is illustrated in Figure 6.5, where the views of two diametrically opposed cameras are shown, for both raw and pre-processed images. In this case the camera with the images to the right was disabled during processing, in order to avoid potential ghost particles reconstructions. The domain coverage was not affected by this due to the redundancy of optical coverage in this specific region.

After pre-processing, the instantaneous velocity of each tracer particle is evaluated at the midpoint of the particle pair, at scattered locations. The time-averaged velocity is brought into a Cartesian grid by ensemble averaging the velocity of particle tracers belonging over cubic cells of 20 mm. Given the spatial concentration and the number of recordings, each bin collects approx. 5000 samples (averaged across the domain). Each separate measurement domain encompasses 60 x 50 x 40 cm^3. At the edges of the domain of interest the concentration of detected tracers decays and with it the number of samples comprised in a single bin. The validity criterion for a velocity vector from a given bin is set to a minimum of 50 samples.

The main sources of velocity uncertainty estimation are identified as resulting from system calibration, particle triangulation and detection uncertainties, signal-to-noise ratio of the particle images, and errors in particle matching and tracking.

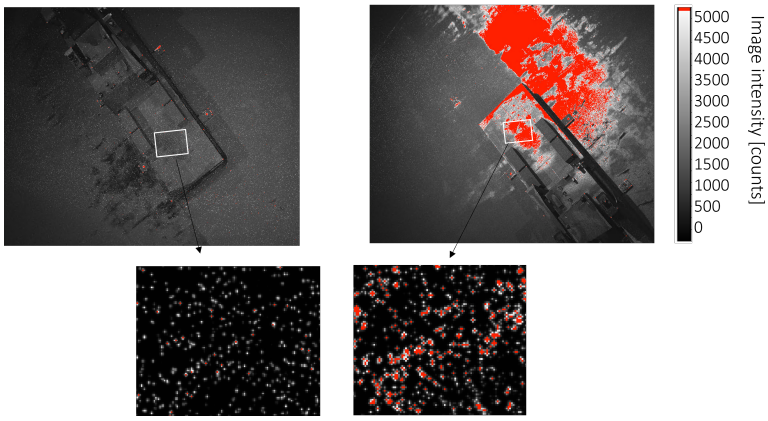

Figure 6.5.: Raw (top) and pre-processed (bottom) images from cameras 1 and 4, aligned approximately diametrically opposed to each other.

Regarding the calibration and particle detection uncertainties, after performing VSC in the particle images, the geometric calibration in this measurement was corrected to below 0.2 pixels for most points. Additionally, given the relatively low ppp value of 0.01 and the tomographic aperture of most camera subsystems exceeding 45 degrees, the ambiguities in particle detection and triangulation are in theory minimal with the IPR algorithm. However the SNR of part of the measurement points was not too high due to the reflections. Illumination intensity varied across the domain as well as temporally due to some issues with back-reflections to the laser head. Additionally, errors in matching and tracking are known to be higher for double-pulse measurement as compared to multi-pulse of time-resolved measurements where particles can be followed over several frames. However the 500/1000 images acquired guarantee convergence of the time-averaged results.

The maximum measured velocity is 5.5 m/s. For the minimum resolvable velocity, an estimation of the local velocity uncertainty is determined by the amplitude of the velocity fluctuations u' divided by the square root of the amount of particles in a bin. The latter estimator is averaged across the measurement domain, yielding a value of approx. 0.02 m/s, which corresponds to 0.3% of the maximum measured velocity. A further discussion of the variation of the velocity fluctuations across the domain, particularly over the ship-flight-deck is provided in section of the unsteady effects.

6.3. EXPERIMENTAL RESULTS AND ANALYSIS

This section presents the time-averaged results of the velocity and vorticity fields around the ship model, starting with the head-wind condition which was compared one-to-one with SFS from Chapter 3. Further the variations in the velocity field with different incoming wind direction are presented for the full-field results, and finally the flow field over the helideck is analysed with Proper Orthogonal Decomposition, revealing the dominant flow dynamics.

Comparisons with other experimental studies are not possible at this time as an experiment with this geometry is not reported in literature, however comparisons are made with the Simplified Frigate Shape, and CFD studies performed on slightly more complex geometries such as the work from D. Lee et al. (2005) and Guillot and Walker (2000), as well as for model at varying incoming wind directions by Tai (1999) and Polsky (2002).

6.3.1. COMPARISON WITH THE SFS

The time averaged normalized streamwise velocity results are plotted in Figure 6.6 on a vertical plane positioned at the centerline of either ship, left the SFS and right the OPV. In this plot line contours and iso-surfaces of zero streamwise velocity are plotted and compared between the models.

Starting from left to right, there is a flow acceleration region over the curvature of the bow over the OPV that is not captured in the SFS measurement. Moving downstream to the recirculation regions R_1 and R_2 present in the SFS are not observed in the OPV due to the more streamlined shape of the bridge region, where the effect of the forward facing step significant in the SFS is not present in the OPV due to the smoother tapered bridge geometry.

Instead a smaller region labelled r_1 is seen behind the equipment mounted atop the bow base. Similarly r_2 and r_3 result from smaller features on the bridge and sides of the OPV. These minor but notable regions only have local influences and are dominated by the larger flow features.

Next, R_3 is used to denote the region behind the prism atop the superstructure in the SFS, corresponding to the mast on the OPV, and since this structure is present in both, it is denoted with the same label. However its shape and downstream extent are different. Even though the mast also acts as a bluff body the more complex and tapered shape results in a region that is longer along the vertical axis behind the more spherical top, and decreases in width vertically down.

Further downstream on the helideck, the recirculation there is labelled R_4. For the case of the SFS it is a simple 3D Backward Facing Step, and for the OPV is more tapered and consisting of two consecutive steps, that have been denoted by $R_{4,1}$ and $R_{4,2}$. In this case only $R_{4,2}$ is of particular interest for the helideck,

and its characteristics are studied on more detail on the following section. $R_{4,1}$ and $R_{4,2}$ are connected by the same iso-surface in the OPV, resulting in a significantly more complex recirculation region, as compared to the rather simpler and symmetrical bubble from the SFS. This profile of the OPV compares closely with the contours that were found by Tai (1999), in their study of a similar geometrical shape at headwind.

Finally the recirculation at the rear R_5 is present in both models, and features a similar shape.

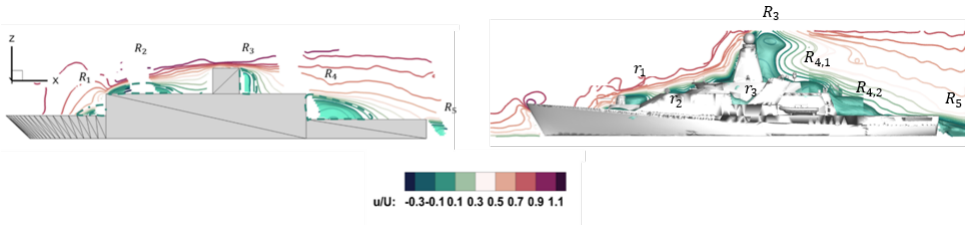

Figure 6.6.: Time-averaged velocity profiles on the vertical symmetry plane for the SFS and OPV.

Further the vorticity field is compared between the two configurations in the head-wind condition, by means of plotting Q-criterion iso-surfaces, normalized by the freestream velocity and hangar height. Q-criterion is preferred over vorticity as it provides some simplicity of interpretation by indicating presence of vortices instead of the rotationality captured in the vorticity which might be caused by shear. The same value of iso-surface is shown for reference. In the left of Figure 6.7 the top view of the Q-criterion iso-contours for the SFS and the OPV are shown next to each other, on the right an isometric view of the OPV is shown.

In both configurations the presence of two vortices along the edges of the bow are observed, that induce local separation and a pronounced downwash on the symmetry plane. It was observed that this structure persisted while increasing the value of the iso-surface and is approax. 4 times stronger in the OPV. This is denoted by Q1 in the iso view, along with the streamlines that denote the clear rotationality of the flow in this section.

Additonally in the OPV an additional scarf vortex is observed around the protruding structure ahead of the bridge, and a smaller arch vortex behind it. Further downstream the vorticity over the bridge of the ship is significantly lower for the OPV, as the shape is more streamlined and the separation and reattachment less pronounced, compared to the sharp edges of the FFS present in the SFS. Another scarf vortex is present along the front side of the bridge, and further downstream ahead of the mast.

The flow development around the mast shows some of the same large-scale features in both configurations. There is a horseshoe vortex in front of the mast in both cases which trails downstream, and an arch vortex behind it. In the case of the SFS that structure more closely resembles an arch, (the term is typically used in literature to describe the vortex behind surface mounted cubes), which is more similar to the SFS shape. In the case of the OPV it is still present, but it is more elongated and tapered, as the width of the mast is also varying vertically.

At the same value of the iso-surface, moving dowstream a series of these arch vortices are observed in the OPV, denoted by Q2 in Figure 6.7, resulting from the double-step configuration of the tapered hangar and finally behind the rear.

Despite the slight model assymetry, for the OPV at headwind the Q-criterion is fairly symmetrical, as in the SFS.

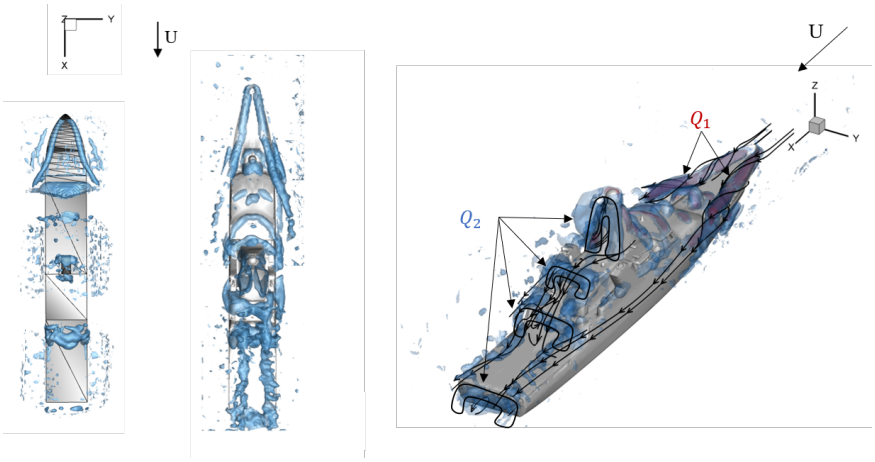

Figure 6.7.: Comparison of the time-averaged $Q^* = 0.02$ iso-surface in blue and $Q^* = 0.08$ in dark red at the bow. Left for the SFS and right for the OPV.

An additional feature that is observed on the deck of the OPV are the side-deck vortices, more clearly present from the top view, which were also present in the SFS but at a lower intensity. Separation is present over the edges of the deck due to spanwise entrainment of fluid from below the surface of the step resulting in recirculation. This is also clear from the streamlines, although it is less pronounced compared to the bow.

From both velocity and vorticity comparisons, it is immediately clear that the flow over the OPV shows a higher complexity of flow structures and features more scales than the SFS. While the SFS is more robust baseline for methodological assessments, and suitable for general airflow investigations, the more complex

shape makes possible better insight into key flow features, and captures more realistic alterations in airflow behaviour.

6.3.2. GLOBAL FLOW-FIELD OVER THE SHIP AT VARYING WIND DIRECTIONS

This section analyses the airflow around the configuration depicted in Figure 6.2, beginning with an overview of the airflow variations at different yaw angles. A plot of zero streamwise velocity iso-surface at the full range of yaw angles tested, is shown in Figure 6.8, with the accent placed on the flow separation and recirculation around the model.

These iso-surfaces encompass recirculation regions resulting from flow separation around various features of the ship. By visual inspection it is clear that the resolution of the measurement is sufficient to capture the wake of the finer structures at a much smaller scale compared to the overall scale of the ship. Additionally no gaps are observable in the data around optically occluding structures.

As the yaw angle increases, the airflow above the helideck becomes less influenced by the airwake from the ship's superstructure, which results in the flow features of positive and negative yaw angles becoming more similar. Any differences above the helideck are due the the presence of the crane at the starboard side of the deck. At higher yaw angles the recirculation zone shifts towards the port side for positive yaw and starboard for negative yaw.

It can be seen that the size and shape of the recirculation regions is influenced by the ship yaw angle, with an overall smaller wake for the headwind condition, and with flow dominated by separation from the superstructure in the crosswind conditions. Zooming in on the deck, the recirculation bubble is largest for the headwind, but extends further downstream the deck for the 45 degree cases.

In general, the flow behaviour directly downstream of the hangar is more complex compared to the aft of the ship, due to a stronger influence of the superstructure and equipment.

For the headwind case, the recirculation region above the helideck is asymetrical with a larger streamwise and vertical extend on the port side. This asymetry arises partly from the asymetrical placement of the equipment on the superstructure but mainly from the crane. This region has a streamwise extent of L_r/L = 0.63 over the helideck from the hangar edge.

Small differences between the 45 and -45 degree cases are seen due to the asymmetry of the model and the presence of the crane. For the 90 degree case the wake is fully swept away from the deck.

At the yaw angles of ±90 degrees, the flow above the helideck accelerates above the freestream velocity due to the blockage of the model, introducing a high velocity gradient, with a flat recirculation region originating from the leading edge in the wind above the helideck.

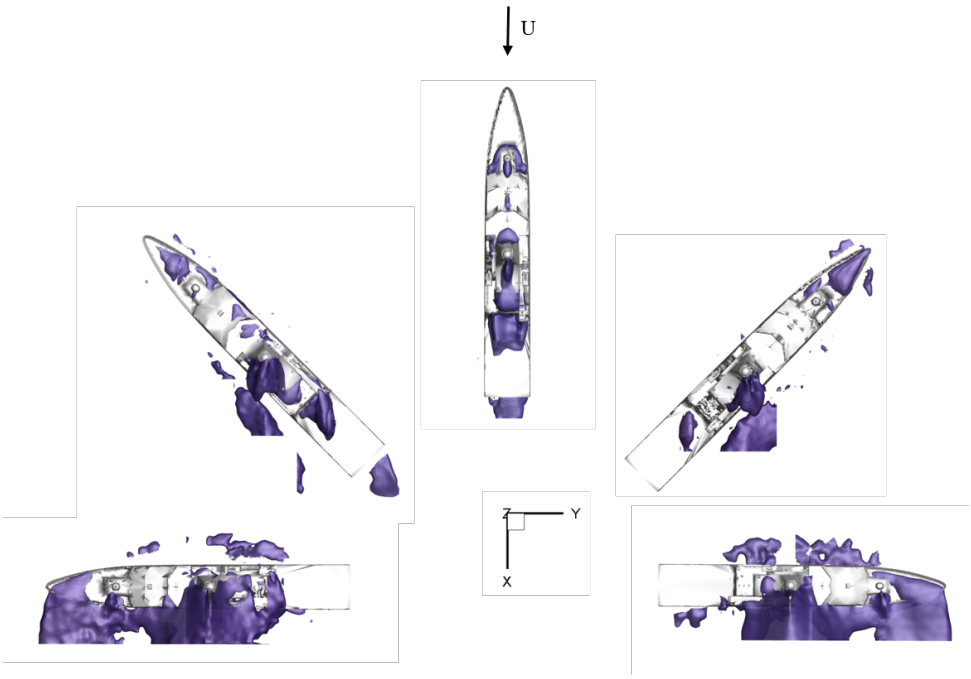

Figure 6.8.: Time-averaged u=0 (streamwise velocity component) iso-surface at incoming wind directions.

Particularly important for the SHOL is the region closer to the mid-deck Forrest et al. (2012). Velocities and turbulent kinetic energy (TKE) profiles are extracted along the line denoted in Figure 6.9. From the velocity profiles it follows that this station is within the wake of the superstructure/hangar at the angles of 0 and 45 degrees, but that the wake is swept sideways for the 90 degree case.

First for the 0 degree headwind conditon: the velocity profile indicates the asymmetry of the downstream extent of the recirculation bubble, which is also observed in Figure 6.8, and the turbulent kinetic energy (TKE) profile has a peak around this zone, at around 20% of the freestream velocity, flattening at around 15% closer to the centre, and close to zero outwards of the deck.

The TKE distribution is increased at the edges of the helideck, as observed for both the SFS (Chapter 3) and the OPV, with the difference that for the SFS the distribution was symmetrical.

For the 45 degree case, a velocity increase is seen closer to the edge in the side of the incoming freestream as the flow accelerates over that side of the deck, followed by a sharp decline as it enters the wake, which extends to the edge of the deck. The turbulence is very low in the incoming flow region, increases to about

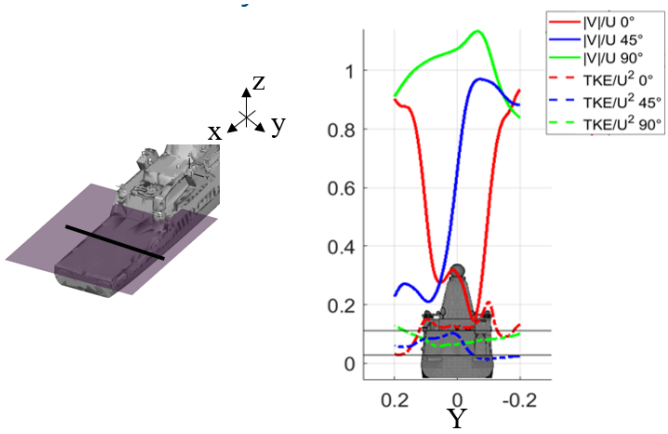

Figure 6.9.: Normalized velocity profiles in the heli-deck at different wind directions.

20% in the shear layer that separates the wake and the flow region, and then goes slightly down beyond that point.

For the 90 degree case, the flow over the deck resembles a forward facing step. A region of flow acceleration is observed as the flow goes over the edge, with a slight deceleration along the deck width, and further decrease downstream of the deck as it enters the small recirculation region behind it. The turbulent kinetic energy profile is fairly flat, at a relatively high level of 10% due to the fluctuations created by the shear layer present in the FFS-similar flow, with a spike after the deck edge.

While for the 0 and 45 degree yaw angles the airflow above the helideck is dominated by the airwake of the upstream structure of the OPV, resulting in a complex flow behaviour, for the 90 degree case, the flow accelerates over the helideck, causing a higher velocity gradient. Both the airwake as well as the higher velocity gradient can influence flight operations above the helideck Shukla et al. (2019).

6.3.3. FLOW DYNAMICS

Although the focus of the measurement was time-averaged measurement as have been presented so far, part of the flow dynamics over the helideck are recovered by POD (Sirovich (1987)). For the POD analysis, the sparse instantaneous data was binned in larger bins of 5 cm with 90% overlap. A sub-section of the domain over the flight-deck, excluding the domain sides and the geometry was considered. The gaps in the instantaneous data were filled with binning with the VIC# implementation in DaVis based on VIC+ Schneiders et al. (2017). A total of 1000

images were considered for the analysis, but the energy distribution in only the first 500 modes is plotted in the left of Figure 6.10.

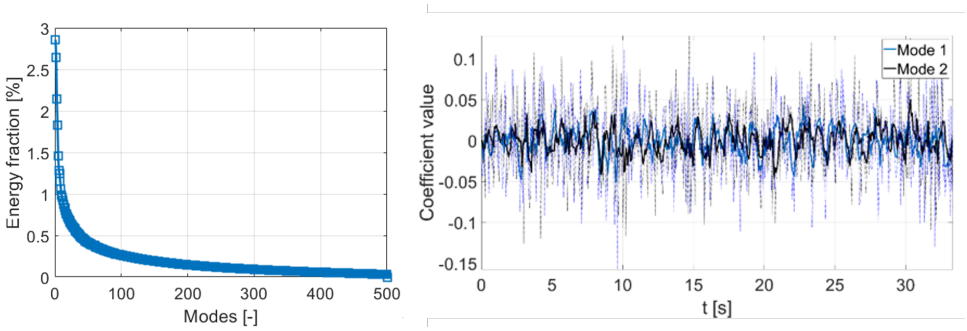

Figure 6.10.: Left: Energy distribution in the first 500 POD modes; Right: Temporal coefficients of Modes 1 and 2

The flat energy distribution suggests that no single mode dominates in capturing the energy of the system, and it is instead distributed evenly across multiple modes. This indicates that the flow is predominantly stochastic in nature, with multiple significant dynamical features contributing to the overall behaviour, even more so that the SFS. For comparison around 3% of the energy is captured in the first two modes for the OPV at headwind, compared to approx. 12% in the case of the SFS.

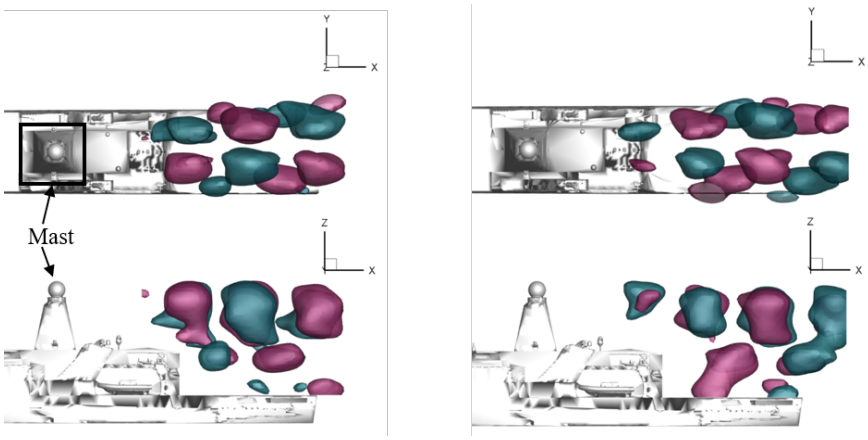

Figure 6.11.: Top and side view of modes 1 and 2, iso-surfaces of u' = − 0.01 m/s

The first two modes seem to be paired and since they have the highest overall energy, their spatial structures are visualized in Figure 6.11.

The two modes exhibit alternating velocity patterns that appear to represent vortex shedding from the mast. In order to investigate this further the temporal modes have been extracted and plotted in the right of Figure 6.10, however extracting the frequency of the shedding from their evolution possibly requires data of higher resolution, remaining inconclusive from this investigation.

Nevertheless, the spatial structure of the modes does seem to represent the alternating vortices in the wake of the structure. Additionally these modes show anti-symmetry with approximately 90 degrees phase shift as determined by visual inspection.

It appears from this that the downstream convection of this shedding is the primary deterministic feature of the flow field over the helideck, the rest is random. This structure is different from the first two modes of the SFS on the helideck, as can be seen by their side-by-side plots in Figure 6.12.

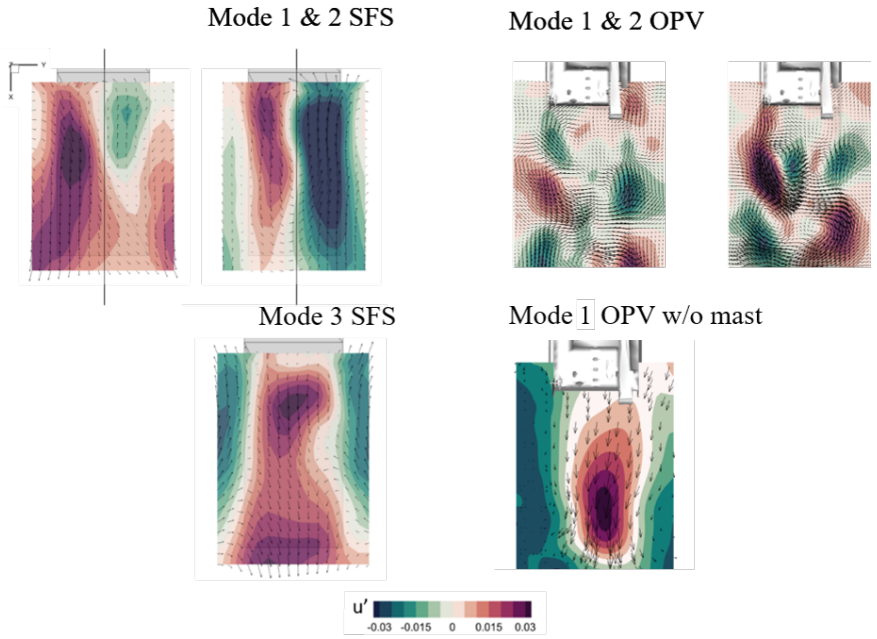

Figure 6.12.: Comparison of the POD modes between different configurations. Top: Modes 1& 2 for the SFS and OPV; Bottom: Mode 3 for the SFS and Mode 1 of the OPV in the configuration without the mast.

In the SFS, the first two modes were concluded to represent the flapping of the wake from side to side, and the examination of the temporal coefficients led to the observation of flow bi-stability. This is not seen in the case of the OPV, suggesting that it is 'broken' due to the small but significant amount of asymmetry

in the model.

In order to test if the effect on the deck is indeed because of the mast, the configuration of the ship without the mast was also investigated, with the POD done in exactly the same way, as was described in the beginning of this section.

From this comparison, it can be seen that the ship without the mast is closer to a 3D BFS, and the first mode from this configuration is similar to the third mode from the SFS configuration corresponding to the lengthening and shortening of the recirculation region along the streamwise direction Driver et al. (1983).

The higher modes feature little energy content, so their examination is skipped from this discussion.

6.4. CONCLUSION

This work reports on a selection of results for the Ocean Patrol Vessel ship model which have been obtained in the 3D PTV experimental campaign with extended optical access at the LST of DNW. Using HFSB as flow tracers, four-directional illumination and six-directional imaging, the flow field around the ship was measured at various incoming wind directions.

The results have shown that the flow field around the ship has been captured in a volume of approx. 0.5 m^3 with minimal gaps due to optical blockage, as is clear by the level of detail present in the velocity fields close to and around the model. The 3D velocity and Q-criterion fields elucidate the complexity of the flow both in the larger scales and the finer structures on the ship superstructure. The results allow for detailed comparisons between different configurations. Focusing on the helideck, which is most crucial for helicopter and drone operations, it has been shown that as well as the air-wake at low yaw angles, as the velocity gradients above the deck at higher yaw angles are significant, and should be carefully considered for flight operations.

From the direct comparison between the Simplified Frigate Shape and the Ocean Patrol Vessel, it was shown that whereas the former is suitable for general airflow investigations and to provide initial insights into key flow features, the latter, more complex shape provides the realistic alterations in airflow behaviour. Additionally from the modal decomposition of the flow field over the deck, the differences between the models were observed to be substantial, with the ocean patrol vessel shape capturing the vortex shedding from the mast as a primary deterministic feature of the flow field over the helideck.

It has been shown that volumetric velocimetry with multi-directional illumination and imaging systems can provide spatially comprehensive data around complex models, measured at varying conditions (varying wind angles) without rearrangements of the PTV setup. The technique was shown to be sufficiently ro-

bust and mature to be used in large-scale testing facilities with promising results. The ability of the technique to provide insight into global unsteady flow analysis was demonstrated.

7

CONCLUSIONS AND PERSPECTIVES

This concluding chapter outlines the technical developments and applications of large-scale volumetric PTV, in the context of facilitating a greater dissemination of this measurement technique for aeronautics.

The applications draw on the advantages of recent progress in tracer particle technology and efficient 3D Particle Tracking algorithms, to further develop methodology that captures relevantly large volumes with improved optical access and increased dynamic velocity range.

The demonstrated robustness of the technique promises time-savings in industrial environments and opens the opportunity for the study of global flow dynamics around relevantly complex geometries from time-averaged velocity data.

The main conclusions by section are summarized in the following, each followed by the author's outlook on further research interest.

7.1. MEASUREMENT TECHNOLOGY DEVELOPMENT

7.1.1. MULTI-DIRECTIONAL VOLUMETRIC VELOCIMETRY SYSTEMS

The extension of optical access around geometrically complex objects is a relatively new topic in PTV, as typical investigations in laboratory level are focused on simplified geometries or wakes. Modern tracers, software and hardware developments have made it possible to perform this kind of measurements at large-scale, therefore making the problem of domain erosion due to blocked optical access more prominent.

Especially when considering applications that feature model rotations, or different configurations of the same model, the limitations of blocked optical access become more strict due to the inefficiency of rearranging the volumetric PTV setup. To overcome these limitations a multi-directional illumination and imaging system is proposed. The core of the approach is the idea that different subsets of cameras can observe different regions of the flow, and these can be

combined in a single system to provide more comprehensive measurement results. Additionally, the redundancy of cameras ensures robustness to reflections, making measurements possible even in areas with particularly extensive reflections in one of the cameras (that would have otherwise made the measurement in these regions impossible in a system with 3-4 cameras).

First a basic framework for the quantification of the combined losses from illumination and imaging is considered. A volumetric loss criterion has been defined which can be used to provide a guideline for the experimental setup design phase. In systems with redundancy, volumetric losses that are below 5% of the domain of interest are recommended. Next, the regions in the domain where particle reconstruction is possible are studied based on the different logics of combining the cameras into subsystems. By employing a domain partitioning approach, wider optical access is afforded.

The methodology has been proven to be effective considering two experimental cases in wind engineering applications around ship models. In the first case, the methodology has allowed an increase in the achievable measurement domain by approximately 20% of the domain of interest, with nearly 5 times more particles tracked with the full camera system in a partitioned mode, as compared to 'standard' 4 standalone camera subsystems.

Finally, through making use of proper orthogonal decomposition the dynamics of the flow are recovered from the low frequency (10 Hz) velocity measurement, and it has been possible to make observations about the dynamic organization of the flow in the regions of interest.

Results of the obtained flow field in terms of reliability and accuracy have been compared to the available literature to show good agreement and add detail on the three-dimensional flow structures.

The main bottleneck of this type of acquisition is the increased complexity/costs of the setup and the increased amount of data acquired. Additionally its application might be limited in environments that do not allow for the free placement of the cameras.

A few ideas could be useful for further research to consider the mitigation of these issues. From a purely geometrical perspective, to minimize volumetric losses, 'merging' the cameras and the illumination is ideal. This would ensure that the cameras do not encounter shadows, and additionally simplify the setup (as is already the case with robotic-PIV). One way to achieve this, hardware-wise, would be with the use of an LED ring (or laser) attached to every camera.

A further step that would decrease setup time would be to mount (pre setup) the cameras and illumination to a fixed dome-like frame, that could be placed inside the test section to circumvent optical access limitations. This comes at the loss of some generality, as it is not possible to optimize a single setup for mea-

surements around every model; as well as with the need to quantify the blockage effect of this frame in the tunnel.

Potential further applications of this kind of measurements lies with aeroelastic studies, where model deformations could be measured simultaneously to the flow field, as well as for measurements around moving objects.

7.1.2. MULTIPLE EXPOSURE FOR VOLUMETRIC VELOCIMETRY

The scarcity of HFSB at higher flow velocities and the limited dynamic velocity range of double-pulse conventional PTV systems has motivated the study of multi-exposure recordings for 3D PTV, where multiple (more than two) recordings of the tracers in the same frame allow for the reconstruction of longer particle trajectories.

However, the analysis of the multiply exposed recordings is challenged by the unknown time identity of each particle exposure, as well as the unknown organization into physical trajectories. Using a sequence of illumination pulses with a constant time separation leads to the motion directional ambiguity problem. An irregular sequence of time separation for the illumination pulses allows recognizing the time identity of the unique sequence of positions in the image. This approach has been adopted in this study.

Based on the assumption of the linearity of particle tracks, a criterion of kinematic similarity is formulated that unambiguously recognizes the particle trajectories. A combinatorial algorithm is proposed whereby a signal-to-noise ratio is introduced for every candidate trajectory. This criterion is combined with another criterion that favours minimum velocity fluctuations along a trajectory.

The algorithm is assessed using experimental data produced with time-resolved analysis using Shake-The-Box. Recordings with three-pulses yield a correct trajectory rate of 85%. The latter declines with the number of pulses, but the error rate decreases with the number of pulses shows that the erroneous particle matching rate from 5.6% for three pulses, to 0.1% for six pulses. This confirms that the method is more reliable when more pulses are comprised in the sequence.

The proposed methodology has to further be tested on multiply exposed recordings in order to characterize its limits with respect to measurement noise and image particle density. The latter is particularly relevant for large-scale volumetric applications.

The main bottleneck of this method is the increased image analysis complexity, and the potential increase in illumination complexity to generate the illumination sequence, particularly as more pulses are considered. Additionally, particle trajectories with velocity close to zero are challenging for the method to discern.

One potential solution for this would be using the technique in combination with double-frame cameras, where inter-frame separations in the order of μs are possible. This is particularly attractive when done with a single exposure in the first frame and multiple exposures in the second, as the second frame of most double-frame cameras has a longer exposure time, naturally allowing multiple exposure.

7.2. IMPACT OF LARGE-SCALE VOLUMETRIC VELOCIMETRY IN AERODYNAMIC DEVELOPMENT

The ability of PTV to elucidate flow fields around complex geometries in large-scale environments, is particularly impactful when considered in combination with its ability to provide validation data for Reynolds-Averaged Navier-Stokes simulations.

In this light, two experiments that were carried out at the Low-Speed Tunnel of the German-Dutch Wind Tunnels and their unique experimental setups and results have been presented.

The first one is a measurement around a thrust-reverser of an engine attached to a complete aircraft. By employing flow seeding achieved with two separate seeding rakes, one integrated inside the nacelle and one in the wind tunnel settling chamber, the flow of the jet as well as the flow field around it were measured with a resolution of 5% of the engine inlet diameter. The large-scale flow topology was investigated to reveal flow reversal, jet plume recirculation due to ground effect, flow leakage from the thrust-reverser doors and re-ingestion. It was shown that large-scale volumetric velocimetry offers key insights into the flow features, and is complementary to more traditional temperature probe based re-ingestion detection criteria.

The second experiment presents results around the Ocean Patrol Vessel ship model which have been obtained in the 3D PTV experimental campaign with extended optical access, and a spatial resolution of 1% of the heli-ship deck length. Using four-directional illumination and six-directional imaging, the flow field around the ship was measured at a spectrum of incoming wind directions (varying ship yaw angles).

The results have shown that the flow field around the ship at different configurations has been captured in volumes of approx. 0.5 m^3 with minimal gaps due to optical blockage, with a high level of detail present in the velocity fields close to and around the model. The 3D velocity and vorticity fields elucidate the complexity of the flow both in the larger scales and the finer structures on the ship superstructure. The results allow for detailed comparisons between different configurations.

It has been shown that volumetric velocimetry with multi-directional illumination and imaging systems can provide spatially comprehensive data around complex models, measured at varying conditions without rearrangements of the PTV setup. The technique is sufficiently robust to be used in large-scale testing facilities with promising results. Additionally, the ability of the technique to provide insight into global unsteady flow analysis was demonstrated.

In conclusion, both applications presented here are representative of measurements that would otherwise not be possible, or very limited with traditional PIV/PTV systems. Combining the above advancements, it is concluded that the developed PTV system and analysis methods merge to a distinct and effective solution for PTV systems in large-scale industrial applications.

7.3. FURTHER POTENTIAL IMPACT

There is certainly further potential of volumetric velocimetry. One aspect that would play a significant role in its greater dissemination would be online data processing for the full datasets. Further extending this with improved data visualization technology, for example 3D holographic data visualization, displayed shortly after each measurement around the model so that the researchers and engineers can walk through the flow field perceiving its full details. This technology is not too futuristic, and in the author's opinion would broadly increase the enthusiasm for the technique.

Another area of research with potential is the study for producing particle tracers that are safe to our health, and that don't pollute the tunnel circuit. Here solutions can be envisaged in the chemical engineering of novel particles, or further downstream, techniques for capturing the tracers so that they don't remain in the tunnel after the experiment.

Finally, the ability of PIV to measure large flow fields non-intrusively, at a very large range of velocities, from close to zero to supersonic, makes it an invaluable tool in the further development of wind tunnels themselves. This could be in the form of (re)calibration of existing tunnels, obtaining highly resolved data for wall corrections, as well as verification of novel wind tunnel designs. In the best case scenario it can provide valuable physical data to inspire new design ideas.

BIBLIOGRAPHY

Adrian, R. J. (1984). Scattering particle characteristics and their effect on pulsed laser measurements of fluid flow: Speckle velocimetry vs particle image velocimetry. *Appl. Opt.*, *23*(11), 1690–1691.

Adrian, R. J. (1986). Image shifting technique to resolve directional ambiguity in double-pulsed velocimetry. *Applied optics*, *25*(21), 3855–3858.

Adrian, R. J. (1991). Particle-imaging techniques for experimental fluid mechanics. *Annual review of fluid mechanics*, *23*(1), 261–304.

Adrian, R. J. (1997). Dynamic ranges of velocity and spatial resolution of particle image velocimetry. *Measurement Science and Technology*, *8*(12), 1393.

Adrian, R. J. (2005). Twenty years of particle image velocimetry. *Experiments in Fluids*, *39*, 159–169.

Adrian, R. J., & Westerweel, J. (2011). *Particle image velocimetry*. Cambridge university press.

Adrian, R. J., & Yao, C. S. (1985). Pulsed laser technique application to liquid and gaseous flows and the scattering power of seed materials. *Applied optics*, *24*(1), 44–52.

Agüera, N., Cafiero, G., Astarita, T., & Discetti, S. (2016). Ensemble 3D PTV for high resolution turbulent statistics. *Measurement Science and Technology*, *27*(12), 124011.

Agüí, J. C., & Jimenez, J. (1987). On the performance of particle tracking. *Journal of fluid mechanics*, *185*, 447–468.

Amin, N. F., & Richards, C. J. (1984). Thrust reverser exhaust plume reingestion model tests. *Journal of Aircraft*, *21*(6), 401–407.

Anderson, J. (2011). *Fundamentals of aerodynamics (SI) units), 6th edition*. McGraw-Hill.

Asbury, S., & Yetter, J. (1998). Static performance of a wing-mounted thrust reverser concept. *34th AIAA/ASME/SAE/ASEE Joint Propulsion Conference and Exhibit*, 3256.

Atkinson, C., & Soria, J. (2009). An efficient simultaneous reconstruction technique for tomographic particle image velocimetry. *Experiments in Fluids*, *47*(4), 553–568.

Barata, J., Bernardo, N., Santos, P., Silva, A., & Resende, R. (2013). Experimental study of a ground vortex: The effect of the crossflow velocity. *Journal of aircraft*, *50*(1), 298–302.

Barata, J., Durao, D., Heitor, M., & McGuirk, J. (1991). Impingement of single and twin turbulent jets through a crossflow. *AIAA Journal*, *29*(4), 595–602.

Barata, J., Durão, D., Heitor, M., & McGuirk, J. (1993). On the analysis of an impinging jet on ground effects. *Experiments in Fluids*, *15*(2), 117–129.

Barbosa-Saldaña, J. G., & Anand, N. K. (2007). Flow over a three-dimensional horizontal forward-facing step. *Numerical Heat Transfer, Part A: Applications*, *53*(1), 1–17.

Barlow, J. B., Rae, W. H., & Pope, A. (1999). *Low-speed wind tunnel testing*. John wiley & sons.

Beresh, S. J. (2021). Time-resolved particle image velocimetry. *Measurement Science and Technology*, *32*(10), 102003.

Birvalski, M., Toxopeus, S., G., S., & D., P. (2024). Comparison of full-scale PIV measurements with cfd simulations of a ship propeller inflow. *21st International Symposium on the Application of Laser and Imaging Techniques to Fluid Mechanics, Lisbon, Portugal*.

Bosbach, J., Kühn, M., & Wagner, C. (2009). Large scale particle image velocimetry with helium filled soap bubbles. *Experiments in Fluids*, *46*, 539–547.

Brücker, C. (1997). 3D scanning PIV applied to an air flow in a motored engine using digital high-speed video. *Measurement Science and Technology*, *8*(12), 1480.

Bryanston-Cross, P., & Sale, R. (1992). The quantitative visualisation of the flow in a 1/10th scale model thrust reverser at the aircraft research association, bedford. *37th International Gas Turbine and Aeroengine Congress and Exposition*.

Buchmann, N. A., Atkinson, C., Jeremy, M. C., & Soria, J. (2011). Tomographic particle image velocimetry investigation of the flow in a modeled human carotid artery bifurcation. *Experiments in Fluids*, *50*, 1131–1151.

Burns, D. E., & Parker, P. A. (2020). Additively manufactured wind-tunnel balance. *Journal of Aircraft*, *57*(5), 958–963.

Caridi, G. C. A., Ragni, D., Sciacchitano, A., & Scarano, F. (2016). Hfsb-seeding for large-scale tomographic PIV in wind tunnels. *Experiments in Fluids*, *57*, 1–13.

Caridi, G. C. A. (2018). *Development and application of helium-filled soap bubbles: For large-scale PIV experiments in aerodynamics* [Doctoral dissertation, Aerospace Engineering, Delft University of Technology].

Carmer, C. F., Heider, A., Schröder, A., Konrath, R., Agocs, J., Gilliot, A., & Monnier, J. C. (2008). Evaluation of large-scale wing vortex wakes from multi-

camera PIV measurements in free-flight laboratory. *Particle Image Velocimetry: New Developments and Recent Applications*, 377–394.

Chovet, C., Lippert, M., Foucaut, J. M., & Keirsbulck, L. (2017). Dynamical aspects of a backward-facing step flow at large Reynolds numbers. *Experiments in Fluids*, *58*(11), 162.

Chun, K. B., & Sung, H. J. (1998). Visualization of a locally-forced separated flow over a backward-facing step. *Experiments in Fluids*, *25*, 133–142.

Cierpka, C., & Kähler, C. (2012). Cross-correlation or tracking-comparison and discussion. *16th international symposium on applications of laser techniques to fluid mechanics, Lisbon, July*, 9–12.

De Gregorio, F., Pengel, K., & Kindler, K. (2012). A comprehensive PIV measurement campaign on a fully equipped helicopter model. *Experiments in Fluids*, *53*, 37–49.

Discetti, S., & Coletti, F. (2018). Volumetric velocimetry for fluid flows. *Measurement Science and Technology*, *29*(4), 042001.

Doh, D. H., Cho, G. R., & Kim, Y. H. (2012). Development of a tomographic PTV. *Journal of mechanical science and technology*, *26*, 3811–3819.

Dooley, G. M., Krebill, A. F., Martin, J., Buchholz, J. H., & Carrica, P. M. (2020). Structure of a ship airwake at multiple scales. *AIAA Journal*, *58*(5), 2005–2013.

Driver, D., Seegmiller, H., & Marvin, J. (1983). Unsteady behavior of a reattaching shear layer. *16th Fluid and Plasmadynamics Conference*, 1712.

Eaton, J. K. (1980). *Turbulent flow reattachment: An experimental study of the flow and structure behind a backward-facing step*. Stanford University.

Elsinga, G. E., Scarano, F., Wieneke, B., & van Oudheusden, B. W. (2006). Tomographic particle image velocimetry. *Experiments in Fluids*, *41*(6), 933–947.

Elsinga, G. E., Westerweel, J., Scarano, F., & Novara, M. (2011). On the velocity of ghost particles and the bias errors in tomographic-PIV. *Experiments in Fluids*, *50*, 825–838.

Erdogdu, A., Hüttig, S., Londono Alfaro, J., T., G., & Schröder, A. (2024). Large-scale side by side stereo-PIV measurement in an automotive wind tunnel: Aerodynamic influence of ride height variations. *21st International Symposium on the Application of Laser and Imaging Techniques to Fluid Mechanics*.

Fahringer, T. W., Lynch, K. P., & Thurow, B. S. (2015). Volumetric particle image velocimetry with a single plenoptic camera. *Measurement Science and Technology*, *26*(11), 115201.

Fajardo, C., & Sick, V. (2009). Development of a high-speed UV particle image velocimetry technique and application for measurements in internal combustion engines. *Experiments in Fluids*, *46*(1), 43–53.

Faleiros, D. E. (2021). *Soap bubbles for large-scale PIV: Generation, control and tracing accuracy* [Doctoral dissertation, Aerospace Engineering, Delft University of Technology].

Faleiros, D. E., Tuinstra, M., Sciacchitano, A., & Scarano, F. (2018). Helium-filled soap bubbles tracing fidelity in wall-bounded turbulence. *Experiments in Fluids*, *59*(3), 56.

Faleiros, D. E., Tuinstra, M., Sciacchitano, A., & Scarano, F. (2019). Generation and control of helium-filled soap bubbles for PIV. *Experiments in Fluids*, *60*, 1–17.

Forrest, J. S., Owen, I., Padfield, G. D., & Hodge, S. J. (2012). Ship-helicopter operating limits prediction using piloted flight simulation and time-accurate airwakes. *Journal of Aircraft*, *49*(4), 1020–1031.

Fuchs, T., Hain, R., & Kähler, C. (2016). Double-frame 3D-PTV using a tomographic predictor. *Experiments in Fluids*, *57*, 1–5.

Gibeau, B., & Ghaemi, S. (2018). A modular, 3D-printed helium-filled soap bubble generator for large-scale volumetric flow measurements. *Experiments in Fluids*, *59*, 1–11.

Grant, I., & Liu, A. (1990). Directional ambiguity resolution in particle image velocimetry by pulse tagging. *Experiments in Fluids*, *10*(2), 71–76.

Gray, C., Greated, C., McCluskey, D., & Easson, W. (1991). An analysis of the scanning beam PIV illumination system. *Measurement Science and Technology*, *2*(8), 717.

Graziani, A., Kerhervé, F., Martinuzzi, R. J., & Keirsbulck, L. (2018). Dynamics of the recirculating areas of a forward-facing step. *Experiments in Fluids*, *59*, 1–18.

Grille Guerra, A., Scarano, F., & Sciacchitano, A. (2024). On the scalability of helium-filled soap bubbles for volumetric PIV. *Experiments in Fluids*, *65*(2), 23.

Guillot, M., & Walker, M. (2000). Unsteady analysis of the air wake over the lpd-17. *18th Applied Aerodynamics Conference*, 4125.

Häfeli, R., Altheimer, M., Butscher, D., & Rohr, P. (2014). PIV study of flow through porous structure using refractive index matching. *Experiments in Fluids*, *55*, 1–13.

Hain, R., & Kähler, C. (2007). Fundamentals of multiframe particle image velocimetry. *Experiments in Fluids*, *42*, 575–587.

Healey, J. V. (1992). Establishing a database for flight in the wakes of structures. *Journal of Aircraft*, *29*(4), 559–564.

Hendriksen, L., Sciacchitano, A., & Scarano, F. (2024). Object registration techniques for 3D particle tracking. *Measurement Science and Technology*, *35*.

Herry, B. B., Keirsbulck, L., Labraga, L., & Paquet, J. B. (2011). Flow bistability downstream of three-dimensional double backward facing steps at zero-degree sideslip. *Journal of Fluids Eng.*, *133*(5), 054501.

Hodge, S. J., Zan, S. J., Roper, D. M., Padfield, G. D., & Owen, I. (2009). Time-accurate ship airwake and unsteady aerodynamic loads modeling for maritime helicopter simulation. *Journal of the American Helicopter Society*, *54*(2), 22005–22005.

Hoyer, K., Holzner, M., Lüthi, B., Guala, M., Liberzon, A., & Kinzelbach, W. (2005). 3D scanning particle tracking velocimetry. *Experiments in Fluids*, *39*, 923–934.

Huhn, F., Schanz, D., Gesemann, S., Dierksheide, U., van de Meerendonk, R., & Schröder, A. (2017). Large-scale volumetric flow measurement in a pure thermal plume by dense tracking of helium-filled soap bubbles. *Experiments in Fluids*, *58*, 1–19.

Hysa, I., Scarano, F., Sciacchitano, A., & Tuinstra, M. (2022). Incommensurable time intervals for multi-exposure PTV. *20th International Symposium on Application of Laser and Imaging Techniques to Fluid Mechanics*.

Hysa, I., Tuinstra, M., Sciacchitano, A., Scarano, F., Schwartz, N., Harrison, C., & Gebbink, R. (2023). Three-dimensional quantitative flow visualization around a thrust reverser. *AIAA*, *61*(12), 5404–5414.

Hysa, I., Tuinstra, M., Sciacchitano, A., Scarano, F., van der Meulen, M. J., Rockstroh, T., & Roosenboom, E. W. (2024). A multi-directional redundant 3D-LPT system for ship–flight–deck wind interactions. *Experiments in Fluids*, *65*(8), 126.

Jahn, T., Schanz, D., & Schröder, A. (2021). Advanced iterative particle reconstruction for lagrangian particle tracking. *Experiments in Fluids*, *62*, 1–24.

Jux, C. (2022). *Development of robotic volumetric PIV: With applications in sports aerodynamics* [Doctoral dissertation, Aerospace Engineering, Delft University of Technology].

Jux, C., Sciacchitano, A., & Scarano, F. (2020). Flow pressure evaluation on generic surfaces by robotic volumetric PTV. *Measurement Science and Technology*, *31*(10), 104001.

Jux, C., Sciacchitano, A., Schneiders, J. F., & Scarano, F. (2018). Robotic volumetric PIV of a full-scale cyclist. *Experiments in Fluids*, *59*, 1–15.

Kähler, C. J., Scharnowski, S., & Cierpka, C. (2012a). On the resolution limit of digital particle image velocimetry. *Experiments in Fluids*, *52*, 1629–1639.

Kähler, C. J., Scharnowski, S., & Cierpka, C. (2012b). On the uncertainty of digital PIV and PTV near walls. *Experiments in Fluids*, *52*, 1641–1656.

Keane, R. D., & Adrian, R. J. (1992). Theory of cross-correlation analysis of PIV images. *Applied scientific research*, *49*, 191–215.

Kempaiah, K. U., Piovesan, T., Zachos, P. K., Michaelis, D., Gebbink, R., van Rooijen, B., Prieto, D. G., MacManus, D., Sciacchitano, A., & Sheaf, C. (2023). High-resolution turbofan intake flow characterization by automated stereoscopic-PIV in an industrial wind tunnel environment. *Measurement Science and Technology*, *35*(2), 025210.

Kühn, M., Ehrenfried, K., Bosbach, J., & Wagner, C. (2012). Large-scale tomographic PIV in forced and mixed convection using a parallel smart version. *Experiments in Fluids*, *53*, 91–103.

Kulkarni, P. R., Singh, S. N., & Seshadri, V. (2005). Flow visualization studies of exhaust smoke-superstructure interaction on naval ships. *Naval Engineers Journal*, *117*(1), 41–56.

Kuratani, N. (2024). Application of onboard PIV to front wheelhouse wake behaviour under stationary crosswind conditions. *21st International Symposium on the Application of Laser and Imaging Techniques to Fluid Mechanics*.

Largeau, J. F., & Moriniere, V. (2007). Wall pressure fluctuations and topology in separated flows over a forward-facing step. *Experiments in Fluids*, *42*(1), 21–40.

Lee, D., Sezer-Uzol, N., Horn, J., & Long, L. N. (2005). Simulation of helicopter shipboard launch and recovery with time-accurate airwakes. *Journal of Aircraft*, *42*(2), 448–461.

Lee, I., Ahn, S., & Sung, H. J. (2004). Three-dimensional coherent structure in a separated and reattaching flow over a backward-facing step. *Experiments in Fluids*, *36*, 373–383.

Lilienthal, O. (1889). *Der vogelflug als grundlage der fliegekunst*. Gaertners Verlagsbuchhandlung, Berlin.

Liu, T., & Salazar, D. M. (2022). Planetary cloud tracking. *Experiments in Fluids*, *63*(5), 76.

Lynch, K., & Scarano, F. (2013). A high-order time-accurate interrogation method for time-resolved PIV. *Measurement Science and Technology*, *24*(3), 035305.

Lynch, K. P., & Scarano, F. (2014). Material acceleration estimation by four-pulse tomo-PIV. *Measurement Science and Technology*, *25*(8), 084005.

Maas, H. G., Gruen, A., & Papantoniou, D. (1993). Particle tracking velocimetry in three-dimensional flows: Part 1. photogrammetric determination of particle coordinates. *Experiments in Fluids*, *15*(2), 133–146.

Maekawa, A., & Sakakibara, J. (2018). Development of multiple-eye PIV using mirror array. *Measurement Science and Technology*, *29*(6), 064011.

Malik, N. A., & Dracos, T. (1993). Lagrangian PTV in 3D flows. *Applied Scientific Research*, *51*, 161–166.

Mallat, B., & Pastur, L. (2023). Aerodynamics of realistic frigate geometries: Conditions for bi-stable wake dynamics. *Ocean Engineering*, *277*, 114311.

Mani, M., & Dorgan, A. J. (2023). A perspective on the state of aerospace computational fluid dynamics technology. *Annual Review of Fluid Mechanics*, *55*(1), 431–457.

Manovski, P., Novara, M., Mohan, N., Geisler, R., Schanz, D., Agocs, J., Godbersen, P., & Schröder, A. (2021). 3D lagrangian particle tracking of a subsonic jet using multi-pulse Shake-The-Box. *Experimental Thermal and Fluid Science*, *123*, 110346.

Miklosovic, D., Snyder, M., & Kang, H. (2011). Ship air wake wind tunnel test results. *29th AIAA Applied Aerodynamics Conference*, 3155.

Muller, K., Hemelrijk, C., Westerweel, J., & Tam, D. (2020). Calibration of multiple cameras for large-scale experiments using a freely moving calibration target. *Experiments in Fluids*, *61*(1), 7.

Nguyen, D., Maher, B., & Hassan, Y. (2019). Effects of nozzle pressure ratio and nozzle-to-plate distance to flowfield characteristics of an under-expanded jet impinging on a flat surface. *Aerospace*, *6*(1), 4.

Novara, M., & Scarano, F. (2013). A particle-tracking approach for accurate material derivative measurements with tomographic PIV. *Experiments in Fluids*, *54*, 1–12.

Novara, M., Schanz, D., Geisler, R., Gesemann, S., Voss, C., & Schröder, A. (2019). Multi-exposed recordings for 3d lagrangian particle tracking with multi-pulse shake-the-box. *Experiments in Fluids*, *60*, 1–19.

Novara, M., Schanz, D., Reuther, N., Kähler, C., & Schröder, A. (2016). Lagrangian 3D particle tracking in high-speed flows: Shake-The-Box for multi-pulse systems. *Experiments in Fluids*, *57*, 1–20.

Novara, M., Schanz, D., & Schröder, A. (2023). Two-pulse 3D particle tracking with Shake-the-Box. *Experiments in Fluids*, *64*(5), 93.

Piirto, M., Saarenrinne, P., Eloranta, H., & Karvinen, R. (2003). Measuring turbulence energy with PIV in a backward-facing step flow. *Experiments in Fluids*, *35*, 219–236.

Poelma, C. (2020). Measurement in opaque flows: A review of measurement techniques for dispersed multiphase flows. *Acta Mechanica*, *231*(6), 2089–2111.

Polsky, S. (2002). A computational study of unsteady ship airwake. *40th AIAA Aerospace Sciences Meeting & Exhibit*, 1022.

Qureshi, M., & Tien, W. (2022). Novel streak-resolving algorithm for particle streak velocimetry. *Flow Measurement and Instrumentation*, *87*, 102208.

Raffel, M., Bauknecht, A., Ramasamy, M., Yamauchi, G. K., Heineck, J. T., & Jenkins, L. N. (2017). Contributions of particle image velocimetry to helicopter aerodynamics. *AIAA Journal*, *55*(9), 2859–2874.

Raffel, M., Richard, H., Ehrenfried, K., Van der Wall, B., Burley, C., Beaumier, P., McAlister, K., & Pengel, K. (2004). Recording and evaluation methods of PIV investigations on a helicopter rotor model. *Experiments in Fluids*, *36*, 146–156.

Raffel, M., Willert, C. E., & Kompenhans, J. (1998). *Particle image velocimetry: A practical guide*. Springer.

Raffel, M., Willert, C. E., Scarano, F., Kähler, C. J., Wereley, S. T., & Kompenhans, J. (2018). *Particle image velocimetry: A practical guide*. springer.

Rosenfeld, N., Kimmel, K., & Sydney, A. J. (2015). Investigation of ship topside modeling practices for wind tunnel experiments. *53rd AIAA Aerospace Sciences Meeting*, 0245.

Samimy, M., & Lele, S. (1991). Motion of particles with inertia in a compressible free shear layer. *Physics of Fluids A: Fluid Dynamics*, *3*(8), 1915–1923.

Saredi, E. (2023). *Advancements in large-scale volumetric PIV and PTV* [Doctoral dissertation, Aerospace Engineering, Delft University of Technology].

Saredi, E., Sciacchitano, A., & Scarano, F. (2020). Multi-Δt 3D-PTV based on Reynolds decomposition. *Measurement Science and Technology*, *31*(8), 084005.

Sarpkaya, T., & Hiriart, G. (1975). Analysis of curved target-type thrust reversers. *AIAA Journal*, *13*(2), 185–192.

Scarano, F. (2001). Iterative image deformation methods in PIV. *Measurement science and technology*, *13*(1), R1.

Scarano, F. (2012). Tomographic PIV: Principles and practice. *Measurement Science and Technology*, *24*(1), 012001.

Scarano, F., Benocci, C., & Riethmuller, M. (1999). Pattern recognition analysis of the turbulent flow past a backward facing step. *Physics of Fluids*, *11*(12), 3808–3818.

Scarano, F., Ghaemi, S., Caridi, G. C. A., Bosbach, J., Dierksheide, U., & Sciacchitano, A. (2015). On the use of helium-filled soap bubbles for large-scale tomographic PIV in wind tunnel experiments. *Experiments in Fluids*, *56*, 1–12.

Scarano, F., & Poelma, C. (2009). Three-dimensional vorticity patterns of cylinder wakes. *Experiments in Fluids*, *47*, 69–83.

Scarano, F., Hysa, I., Grille Guerra, A., Tuinstra, M., & Sciacchitano, A. (2025). Asymmetric time sequence for multiple-exposure 3D PTV. *Experiments in Fluids*, *66*(4), 74.

Schanz, D., Gesemann, S., & Schröder, A. (2016). Shake-the-box: Lagrangian particle tracking at high particle image densities. *Experiments in Fluids*, *57*, 1–27.

Schanz, D., Gesemann, S., Schröder, A., Wieneke, B., & Novara, M. (2012). Non-uniform optical transfer functions in particle imaging: Calibration and application to tomographic reconstruction. *Measurement Science and Technology*, *24*(2), 024009.

Schanz, D., Schröder, A., Novara, M., Geisler, R., Agocs, J., Eich, F., Bross, M., & Kähler, C. J. (2019). Large-scale volumetric characterization of a turbulent boundary layer flow. *Proceedings of the 13th international symposium on particle image velocimetry*, (182), 251–265.

Schneiders, J. F. G., Scarano, F., Jux, C., & Sciacchitano, A. (2018). Coaxial volumetric velocimetry. *Measurement Science and Technology*, *29*(6), 065201.

Schneiders, J. F., Scarano, F., & Elsinga, G. E. (2017). Resolving vorticity and dissipation in a turbulent boundary layer by tomographic PTV and VIC+. *Experiments in Fluids*, *58*, 1–14.

Schnurr, N., Williamson, J., & Tatom, J. (1972). An analytical investigation of the impingement of jets on curved deflectors. *AIAA Journal*, *10*(11), 1430–1435.

Schröder, A., Geisler, R., Staack, K., Elsinga, G., Scarano, F., Wieneke, B., Henning, A., Poelma, C., & Westerweel, J. (2011). Eulerian and lagrangian views of a turbulent boundary layer flow using time-resolved tomographic PIV. *Experiments in Fluids*, *50*, 1071–1091.

Schröder, A., & Schanz, D. (2023). 3d lagrangian particle tracking in fluid mechanics. *Annual Review of Fluid Mechanics*, *55*(1), 511–540.

Schröder, A., Schanz, D., Bosbach, J., Novara, M., Geisler, R., Agocs, J., & Kohl, A. (2022). Large-scale volumetric flow studies on transport of aerosol particles using a breathing human model with and without face protections. *Physics of Fluids*, *34*(3).

Schröder, A., Schanz, D., Geisler, R., Jahn, T., Willert, C. E., Leclaire, B., & Gallas, Q. (2019). A characterization of the flow around a surface mounted cube by TR-PIV and 3D Shake-The-Box. *13th International Symposium on Particle Image Velocimetry*, (209), 285–300.

Schröder, A., & Willert, C. E. (2008). *Particle image velocimetry: New developments and recent applications*. Springer.

Sciacchitano, A., Giaquinta, D., Schneiders, J. F. G., Scarano, F., van Rooijen, B. D., & Funes, D. E. (2018). Quantitative flow visualization of a turboprop aircraft by robotic volumetric velocimetry. *Proceedings 18th international symposium on flow visualization*.

Sciacchitano, A., & Wieneke, B. (2016). PIV uncertainty propagation. *Measurement Science and Technology*, *27*(8), 084006.

Sciacchitano, A., Scarano, F., & Wieneke, B. (2012). Multi-frame pyramid correlation for time-resolved PIV. *Experiments in Fluids*, *53*, 1087–1105.

Seth, D., Leishman, J. G., Gnanamanickam, E., & Zhang, Z. (2021). Time-resolved ship airwake measurements in a simulated atmospheric boundary layer. *Journal of Aircraft*, *58*(3), 624–649.

Shukla, S., Sinha, S., & Singh, S. (2019). Ship-helo coupled airwake aerodynamics: A comprehensive review. *Progress in Aerospace Sciences*, *106*, 71–107.

Sirovich, L. (1987). Turbulence and the dynamics of coherent structures. ii. symmetries and transformations. *Quarterly of Applied mathematics*, *45*(3), 573–582.

Soloff, S. M., Adrian, R. J., & Liu, Z. C. (1997). Distortion compensation for generalized stereoscopic particle image velocimetry. *Measurement science and technology*, *8*(12), 1441.

Sousa, J. (2002). Turbulent flow around a surface-mounted obstacle using 2D-3C DPIV. *Experiments in Fluids*, *33*(6), 854–862.

Spazzini, P., Iuso, G., Onorato, M., Zurlo, N., & Di Cicca, G. (2001). Unsteady behavior of back-facing step flow. *Experiments in Fluids*, *30*(5), 551–561.

Spoelstra, A. (2022). *Ring of fire as a novel approach to study cycling aerodynamics* [Doctoral dissertation, Aerospace Engineering, Delft University of Technology].

Spoelstra, A., de Martino Norante, L., Terra, W., Sciacchitano, A., & Scarano, F. (2019). On-site cycling drag analysis with the ring of fire. *Experiments in Fluids*, *60*, 1–16.

Stone, S. W., Meinhart, C. D., & Wereley, S. T. (2002). A microfluidic-based nanoscope. *Experiments in Fluids*, *33*(5), 613–619.

Strash, D. J., Summa, J. M., Frank, J. H., & Standish, R. (2000). Aerodynamic analysis of an installed thrust reverser. *Journal of Propulsion and Power*, *16*(1), 10–15.

Tai, T. C. (1999). Simulation and analysis of lud ship airwake by navier-stokes method. *Fluid Dynamics Problems of Vehicles Operating Near or in the Air-Sea Interface*, *4*, 1.

Taira, K., Brunton, S. L., Dawson, S. T., Rowley, C. W., Colonius, T., McKeon, B. J., Schmidt, O. T., Gordeyev, S., Theofilis, V., & Ukeiley, L. S. (2017). Modal analysis of fluid flows: An overview. *AIAA Journal*, *55*(12), 4013–4041.

Tinney, C. E., Shipman, J., & Panickar, P. (2020). Proper-orthogonal-decomposition-based reduced-order models for characterizing ship airwake interactions. *AIAA Journal*, *58*(2), 633–646.

Tinney, C., & Ukeiley, L. (2009). A study of a 3D double backward-facing step. *Experiments in Fluids*, *47*, 427–438.

Tsai, R. (1987). A versatile camera calibration technique for high-accuracy 3D machine vision metrology using off-the-shelf tv cameras and lenses. *IEEE Journal on Robotics and Automation*, *3*(4), 323–344.

Utami, T., & Ueno, T. (1984). Visualization and picture processing of turbulent flow. *Experiments in Fluids*, *2*(1), 25–32.

Uzol, O., Chow, Y.-C., Katz, J., & Meneveau, C. (2002). Unobstructed particle image velocimetry measurements within an axial turbo-pump using liquid and blades with matched refractive indices. *Experiments in Fluids*, *33*(6), 909–919.

Van Dyke, M. (1982). *An album of fluid motion* (Vol. 176). Parabolic Press Stanford.

Van Hengst, J. (1992). Aerodynamic investigation of thrust-reversers on the Fokker 100. *AGARD 498, Vol. 10*.

Van Muijden, J., Boelens, O., van der Vorst, J., & Gooden, J. (2013). Computational ship airwake determination to support helicopter-ship dynamic interface assessment. *21st AIAA Computational Fluid Dynamics Conference*, 3078.

Vandervoort, B., Naughton, J. W., & Nikoueeyan, P. (2023). The development of pressure gloves for unsteady pressure measurements on varying airfoil geometry. *AIAA AVIATION 2023 Forum*, 3678.

Vidales, A. (2016). *Air-wake flow dynamics on a simplified frigate shape: An experimental study by large-scale tomographic PTV* [Master's thesis, Aerospace Engineering, TU Delft].

Wadcock, A. J., Yamauchi, G. K., & Schairer, E. T. (2013). Wind tunnel measurements of the wake of a full-scale uh-60a rotor in forward flight. *69th American Helicopter Society Annual Forum*, (ARC-E-DAA-TN6205).

Wall, A., Thornhill, E., Barber, H., McTavish, S., & Lee, R. (2022). Experimental investigations into the effect of at-sea conditions on ship airwake characteristics. *Journal of Wind Engineering and Industrial Aerodynamics*, *223*, 104933.

Wang, C. P. (1988). Laser doppler velocimetry. *Journal of Quantitative Spectroscopy and Radiative Transfer*, *40*(3), 309–319.

Wereley, S., & Meinhart, C. D. (2010). Recent advances in micro-particle image velocimetry. *Annual review of fluid mechanics*, *42*(1), 557–576.

Westerweel, J. (2000). Effect of sensor geometry on the performance of PIV interrogation. *Laser Techniques Applied to Fluid Mechanics: Selected Papers from the 9th International Symposium Lisbon, Portugal, July 13–16, 1998*, 37–55.

Westerweel, J., Elsinga, G. E., & Adrian, R. J. (2013). Particle image velocimetry for complex and turbulent flows. *Annual Review of Fluid Mechanics*, *45*(1), 409–436.

Wieneke, B. (2005). Stereo-PIV using self-calibration on particle images. *Experiments in Fluids*, *39*, 267–280.

Wieneke, B. (2008). Volume self-calibration for 3D particle image velocimetry. *Experiments in Fluids*, *45*(4), 549–556.

Wieneke, B. (2012). Iterative reconstruction of volumetric particle distribution. *Measurement Science and Technology*, *24*(2), 024008.

Wieneke, B., & Rockstroh, T. (2024). Lagrangian particle tracking in the presence of obstructing objects. *Measurement Science and Technology*, *35*(5), 055303.

Willert, C., Stasicki, B., Klinner, J., & Moessner, S. (2010). Pulsed operation of high-power light emitting diodes for imaging flow velocimetry. *Measurement Science and Technology*, *21*(7), 075402.

Willert, C. E., & Gharib, M. (1991). Digital particle image velocimetry. *Experiments in Fluids*, *10*(4), 181–193.

Wolf, C. C., Schanz, D., Schwarz, C., Heintz, A., Bosbach, J., Strübing, T., & Schröder, A. (2024). Volumetric wake investigation of a free-flying quadcopter using shake-the-box lagrangian particle tracking. *Experiments in Fluids*, *65*(10), 152.

Zan, S. (2005). On aerodynamic modelling and simulation of the dynamic interface. *Proceedings of the Institution of Mechanical Engineers, Part G: Journal of Aerospace Engineering*, *219*(5), 393–410.

Zhu, N., Zhang, Z., Gnanamanickam, E. P., & Leishman, J. G. (2024). Estimation of 3D ship airwakes using dual-plane PIV. *Experiments in Fluids*, *65*(1), 11.

ACKNOWLEDGEMENTS

In the first instance I would like to thank my team of supervisors, who have made this PhD possible and from whom I've learned a lot. Thank you to Marthijn, my supervisor from NLR, Andrea and Fulvio, my promotors from TU Delft. It is encouraging how working with competent and skilled people, who are enthusiastic about their work, can lift you up to a higher professional level. I appreciate having had that chance, especially having started this PhD from a place of no previous experience in aerodynamics.

I would like to also thank the managers (over time) of the Aero-acoustics department at NLR, Joost, Barbara, and Marthijn, for their support during my work, and all the colleagues from the department, DNW and TU Delft with whom I've had good discussions: Hasse, Julian, David, Karel, Tim, Lars, Mark-Jan, Jaap, Evelien, Bart, Roy, Edo, Gabriel, Christoph, Kushal, Constantin, Luuk, Adrian, Kherlen.

I want to thank my therapist, Jan-Willem, even if he's now retired. It was his job to listen to my life story and generally depressing worldview, but he was good at it, and that has helped me a lot.

Thank you to Maud, Shucheta, Dominique and Alberto just in general for being such good friends, and thank you to Ivo for being more optimistic about my work than I am.

Thank you to Egon, for reading my introduction and giving me his thoughts on it, and also for joining the billiard competition at NLR so that I don't have to be last again. The only thing I love more than being alone, is being with him.

I have to thank my sister, Enxhi, for more than I can possibly express here or anywhere. She's the best thing my parents have done for me. And also my brother, Arbis, for providing continuous examples of monumental laziness, and such simplicity of thinking, that make me feel better about myself whenever I question if I'm lazy or stupid.

CURRICULUM VITÆ

Ilda HYSA

EDUCATION

2013–2017	Bachelor of Science, Aerospace Engineering Middle East Technical University
2017–2019	Master of Science, Computational Mechanics of Materials and Structures University of Stuttgart
2020–2025	PhD Aerospace Engineering, Aerodynamics Delft University of Technology

PROFESSIONAL EXPERIENCE

2019–2020	Researcher in computational modelling of Carbon Matrix Composites German Aerospace Center
2024–Present	Experimental Aerodynamicist Royal Dutch Aerospace Center

LIST OF PUBLICATIONS

JOURNAL PUBLICATIONS

1. **Hysa, I.**, Tuinstra, M., Sciacchitano, A., Scarano, F., Schwartz, N., Harrison, C., and Gebbink, R. (2023). Three-dimensional quantitative flow visualization around a thrust reverser. *AIAA*, 61(12), 5404–5414.

2. **Hysa, I.**, Tuinstra, M., Sciacchitano, A., Scarano, F., v.d. Meulen, M. J., Rockstroh, T., and Roosenboom, E. W. (2024). A multi-directional redundant 3D-LPT system for ship–flight–deck wind interactions.*Experiments in Fluids*,65(8), 126

3. Scarano, F., **Hysa, I.**, Grille Guerra, A., Tuinstra, M., and Sciacchitano, A. (2025). Asymmetric time sequence for multiple-exposure 3D PTV. *Experiments in Fluids*, 66(4), 74.

CONFERENCE PUBLICATIONS

1. **Hysa, I.**, Tuinstra, M., Scarano, F., Sciacchitano, A., Lammers, K., Gebbink, R., and Harrison, C. (2022). Isolated Thrust-Reverser Investigation by Large-Scale 3D PIV. *AIAA SCITECH 2022 Forum*, Online.

2. **Hysa, I.**, Scarano, F., Sciacchitano, A., and Tuinstra, M. (2022). Incommensurable time intervals for multi-exposure PTV. *20th International Symposium on Application of Laser and Imaging Techniques to Fluid Mechanics*. Lisbon, Portugal.

3. **Hysa, I.**, Tuinstra, M., Sciacchitano, A., and Scarano, F. (2023). A multi-directional redundant 3D-PIV system for ship deck wind interactions. *15th International Symposium on Particle Image Velocimetry–ISPIV*, San Diego, USA.

4. **Hysa, I.**, Tuinstra, M., v.d. Meulen M.J. , Sciacchitano, A., Scarano, F. and Roosenboom E. M. (2025). 3D quantitative flow visualization around a ship at varying wind directions, *21st International Symposium on Flow Visualization*, Tokyo, Japan.

5. de Santana, L., Mertens, C., **Hysa, I.**, v.d. Meulen, M.J., Knepper, K., Tuinstra, M. (2025). Combined flow field and structural deformations measurements via integrated camera arrays, *AIAA SciTech*, Orlando, USA.